Department of Precision and Microsystems Engineering

A Fabrication Route for Integrating a Crystalline Barium Titanate Film onto Compliant PDMS Membranes

Nelson Pittroff

Report no : 2026.106
Coach : Semih Sevim, Mathieu Mirjolet
Professor : Murali Ghatkesar
Specialisation : Micro and Nano Engineering (MNE)
Type of report : Master Thesis
Date : 22 October 2026

TU Delft Delft University of Technology

Challenge the future

I dedicate this thesis to my family.
To my brothers, who shaped the man I am, to my parents, who encouraged me to follow my passion and saw what I could do before I did, and to my grandmother, who helped me relax and take my mind off the work.
Especially to my grandfather. He is my example, and he is the reason I began mechanical engineering. He showed me that challenging times are periods of growth, and that failure is a chance to reflect. He taught me to be persistent, and to measure myself by my own standards.

Declaration on the Use of Generative AI

Generative artificial-intelligence tools, including ChatGPT and Cursor, were used during the preparation of this thesis to support language editing, structuring, and the development and review of analysis code. All generated content was critically reviewed and revised by the author. The experimental work, selection of methods, data analysis, interpretation of results, and scientific conclusions remain the responsibility of the author. No experimental data were generated or altered using generative AI.

A Fabrication Route for Integrating a Crystalline Barium Titanate Film onto Compliant PDMS Membranes

Nelson Pittroff[a,b]

[a] Micro and Nano Engineering, Mechanical Engineering Faculty, Delft University of Technology, Mekelweg 2, Delft, 2628 CD, Zuid-Holland, The Netherlands
[b] Multi-Scale Robotics Lab, Institute of Robotics & Intelligent Systems, D-MAVT, ETH Zurich, Tannenstrasse 3, Zurich 8092, Switzerland

Supervisors: Murali Ghatkesar[a], Semih Sevim[b] and Mathieu Mirjolet[b]

ABSTRACT:
Neural implants are battery-powered electrical devices whose electrodes are placed on nerves in the brain and stimulate them via electrical signals. They are used to treat Parkinson's disease and drug-resistant epilepsy, and they remain in the body for years. The electrodes sit on the brain, while the battery is sealed in a rigid housing placed in a pocket in the chest. Body tissue is soft and moves, therefore the rigid housing and the leads connecting it to the electrodes create a mechanical mismatch and can inflame the tissue and damage nearby cells. Furthermore, the finite battery life requires additional replacement surgery increasing infection risks and health care costs. A soft carrier would allow a smaller, leadless implant, with the stimulus produced at the nerve directly. Piezoelectric ceramics are a suitable option to create these implants, as a deformation of the ceramic produces an electrical signal. Pressure changes in the body can supply that deformation, enabling the implant to stimulate the nerves without an external power source. However, growing crystalline oxides require a single crystal substrate and harsh growing conditions that flexible substrates cannot provide, making them difficult to integrate. Flexible electronics are already addressing parts of this integration challenge using sacrificial substrates to grow piezoelectric oxides on and move them onto a flexible substrate after. However, joining the oxide and integrating it with the electrical connections so the stack stays intact and bonded to the substrate remains difficult. This thesis establishes a fabrication route for that stack. A gold electrode is transferred onto a flexible polydimethylsiloxane membrane, and a barium titanate film, covered with gold, is released from its growth wafer and transferred onto that electrode. The fabrication route was established by optimizing the pulsed-laser deposition of the thin films, adding support during release and transfer, and developing a stable method to transfer gold to the soft polymer.

Keywords: Thin films, Pulsed-Laser Deposition, Flexible electronics, Piezoelectrics, Multilayer-stack

1. INTRODUCTION

Long-term electronic implantable systems are devices that remain in the body and electrically stimulate tissue or record its activity for months or years and are used to develop treatments and diagnostic methods [1, 2, 3]. Established clinical examples are cardiac pacemakers, cochlear implants, and deep-brain stimulators. The challenge of obtaining good readings or enabling sufficient stimulation is keeping contact between the device and the tissue. The surfaces they meet are soft and moving: the heart, the brain, the spinal cord, and peripheral nerves. Flexible electronics are pursued so that those readouts or stimulations can be conducted on that soft tissue without causing inflammation or loosing contact due to tissue deformation for as long as the implant remains [1, 3]. Typically, devices in clinical use separate the power unit from the sensing or stimulating part to overcome compatibility, space, and long-term integration issues. In neural stimulation devices, the electronics are typically housed in a rigid case away from the stimulation site, and insulated wires connect the functional part to the battery [4, 5]. This architecture introduces electrical losses, increases the risk of infection, and constrains system miniaturization [2, 6, 7]. Localized energy generation by converting mechanical energy in to electrical using piezoelectric materials could remove the need for spatial separation of the functional components and enable direct on-site stimulation or wireless sensing.

In order to provide a closer application-based approach, and due to the high potential for biological stimulation and sensing, the materials and device geometry take neural stimulation as their design guide. The pressure fluctuations of the cerebrospinal fluid (CSF) could bulge a soft membrane and introduce strain to it. The bulge test is the laboratory form of that loading. Barium titanate ($BaTiO_3$) is the piezoelectric material chosen here over commonly used lead zirconate titanate (PZT) and polyvinylidenefluoride (PVDF) because it has a higher biocompatibility than PZT [8, 9], while delivering a stronger piezoelectric response than PVDF [10, 11, 12]. Functionalized flexible electronics could enable smaller, distributed, or leadless implant architectures that avoid the previously mentioned issues. This can be achieved by integrating a piezoelectric layer on a soft carrier that converts bodily pressure fluctuations into mechanical deformation of the substrate to trigger electrical signal generation at the tissue and power stimulation [7, 5, 13, 14]. This architectural potential remains

largely unexplored in the implantable domain. Neural stimulation is only one application of flexible electronics, as they enable the placement of gold electrode arrays and soft probes to record electrical signals or stimulate nerves [3].

However, the fabrication and integration of a thin-film crystalline oxide on a soft substrate are challenging, as the growth conditions are not compatible with typically used carriers such as polydimethylsiloxane (PDMS). Direct growth needs a high temperature and a lattice-matched wafer, and PDMS provides neither [15]. By releasing the oxide from a sacrificial crystal layer and transferring it, the growth temperature and the lattice mismatch are avoided [16, 17]. Adding to the complexity is the integration of electrical contacts to the thin film and substrate, to distribute or read the electrical signal. While these methods have been developed, damage-free exfoliation and transfer are still challenging, especially with multiple layers [18]. The main challenge is no longer the single-layer transfer of conductors or oxides, but rather the assembly and transfer of multiple intact layers that do not delaminate over time or under strain [19].

This work developed a route for building this stack of thin films on a PDMS membrane. The gold electrodes enable the electrical characterization of these films in the future. The functional oxide in that stack is interchangeable. Fabrication is demonstrated with $BaTiO_3$, and it can be applied to other crystalline oxides that tolerate the same release and transfer. The results demonstrate that the oxide keeps its preferred crystal orientation through the release and transfer. This opens the way for electrical stimulation driven by a pressure change, and for continuous long-term pressure readings from the same stack. Cell stimulation was not carried out, and no usable piezoelectric output was measured. The thesis focuses on the fabrication.

2. METHODS

As briefly described in the introduction the device is designed to transfer mechanical pressure deformation into an electrical signal. The fabrication route is developed to build a device composed of a molded PDMS chip that consists of a circular cavity with a membrane spanning over it, that allows later deformation. The membrane is made from PDMS and clamped over the cavity. From the bottom (PDMS-membrane) to the top, the layers are; a bottom gold electrode, $BaTiO_3$, a small titanium adhesive layer, a top gold electrode, and a supporting polymethylmethacrylate (PMMA) layer. The piezoelectric film is attached to the soft membrane, and it is loaded through the pressure-induced deflection of this thin PDMS membrane. The strain is transferred only as long as the oxide stay attached. Delamination at the gold/oxide interface or cracking releases the strain and therefore reduces the stress in the film, causing the piezoelectric effect to diminish, highlighting the importance of a continuous, crack-free piezoelectric layer with strong adhesion between the thin films.

Figure 1 and Figure 2 show the systematic fabrication route of the previously described stack. The integrated electrode on the PDMS-platform and the oxide layer are fabricated separately and joined at the end. Route A shows the process that builds the base (Fig. 1**g**) and consists of: a molded PDMS chip with a cavity that has a 5 mm diameter (Fig. 1**b**) and a spin-coated PDMS membrane that carries the transferred gold electrode (Fig. 1**e**). Route B (Fig. 2) builds the oxide layer (functional layer), grown on strontium titanate ($SrTiO_3$) with a water-soluble strontium aluminate ($Sr_3Al_2O_6$) layer under the $BaTiO_3$ (Fig. 2**a**). On top of the $BaTiO_3$, an adhesive layer of titanium attaches the top gold electrode to the stack (Fig. 2**b**). PMMA and temperature-release tape (TRT) support that stack during the water release and transfer (Fig. 2**c**, **d**). The alignment of the bottom electrode and the functional stack is done in the last assembly step and results in the final device shown in Figure 1**h**.

2.1 ELECTRODE PLATFORM

The chip mold is made from Kapton-tape that is applied on a silicon wafer. The mold consists of a 5 mm circle and a 1 mm thick 15×15 mm spacer around that circle, creating the chip edges. This is done to easily cut the finished chips to the correct size. The wafer with the mold is exposed to chlorotrimethylsilane vapor (Sigma-Aldrich 92360) (1 mL, desiccator, 10^{-2} bar, 5 min). The vapor leaves a thin hydrophobic layer on the silicon, so the cured PDMS releases easily [20, 21]. This causes the cured chips to peel off easily without residual PDMS on the wafer. Sylgard 184 is mixed at a 10:1 base-to-curing-agent weight ratio, degassed for 30 min, and then poured onto the functionalized wafer. The wafer and polymer are cured at 60 °C for 45 min, peeled, and given a final cure at 100 °C for 12 h. After the final cure, a 1.5 mm hole is punched through the chip into that cavity for the pressure inlet (Fig. 1**b**). Mold fabrication and cleaning are explained in detail in the Appendix I.1.

The membrane is fabricated by mixing Sylgard 184 at a 20:1 ratio by weight, then spin-coating that mixture using a Polos SPIN 150i spin coater. The program is 100 rpm for 10 s, then 1000 rpm for 55 s. The coating is cured at 80 °C for 30 min and left at room temperature for 12 h. Thickness is measured with a Zygo NewView 5000 scanning white-light interferometer microscope at four points along the peeled boundary. On the device membrane, the four readings were 78.38, 80.16, 81.77, and 84.03 μm, a mean of 81.09 ± 2.40 μm, where the uncertainty is the standard deviation of those four points. At 2000 rpm, the thickness was 42.60 ± 0.57 μm. Later deformation tests described in Section 3.4 and Appendix II use bare membranes that measured 83.19 ± 0.81 μm. The second speed was initially tested to understand the behavior of the bulge with different PDMS thicknesses, and the results are reported in the Appendix II.

The bottom gold electrode is evaporated in a VTD Vera 450H. A 50 nm gold film is directly evaporated onto the silicon wafer, without chromium or titanium in between, to avoid strong adhesion of the gold to the wafer. The base pressure is 6×10^{-5} mbar, and the rate is 2 Å s^{-1}. A Kapton shadow mask defines the geometry with contact pads outside the cavity (the designs are seen in Figure 8). 3-Mercaptopropyltrimethoxysilane (MPTMS) is the molecular adhesive used to carry the thin gold film from silicon onto PDMS [22]. The gold is immersed in a 0.1 mM solution of MPTMS in absolute ethanol for 30 min, rinsed

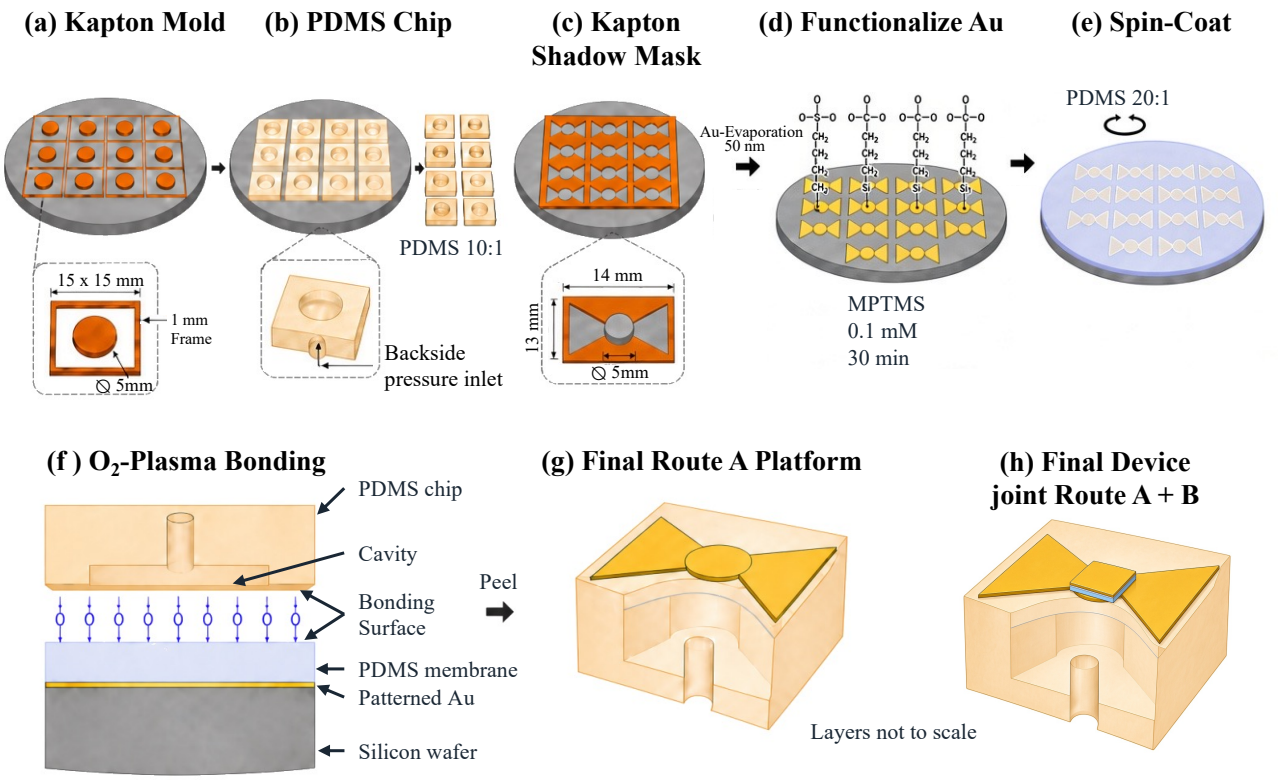


Figure 1: Fabrication of the Route A PDMS platform. **(a)** Laser-cut Kapton mold used to cast the chip array (15 × 15 mm chips, 1 mm frame, ⌀5 mm cavity). **(b)** Molded PDMS chips were peeled, cut and a pressure inlet is punched. **(c)** Kapton shadow mask for the bow-tie Au electrode and evaporation of gold. **(d)** Patterned Au was treated with 0.1 mM MPTMS for 30 min. **e** 20:1 PDMS membrane was spin-coated onto the donor. **(f)** O_2-plasma bonding of the PDMS chip to the membrane, followed by peeling from the silicon wafer. **(g)** Completed Route A platform. **(h)** Final device combination of both routes after functionalizing (g) with MPTMS for 30 minutes and then activating both final fabrication routes in plasma, temperature tape removed

with ethanol, and dried with nitrogen (Fig. 1**d**). The 20:1 PDMS mixture is spun over that gold and cured as described above (Fig. 1**e**). Both the membrane face and the chip face are treated in a Diener oxygen-plasma Asher, evacuated to 0.2 mbar, brought to 1 mbar in oxygen, and run at 100% of the instrument setting for 25 s (Fig. 1**f**). The surfaces are contacted within 1 min after the plasma treatment, held at 70 °C for 30 min for the bonds to close, subsequently rested to reach room temperature, and peeled from the silicon wafer so the gold leaves with the membrane (Fig. 1**g**). A transfer is accepted when the middle electrode lies on the cavity, the central area is complete, there are no large holes, and no cracks are visible that would break electrical continuity. This is tested by measuring the resistance with a multimeter from one end to the other. The transfer was experimentally improved by testing different post-deposition treatments, concentration, and exposure time. The transfer was judged from a visual screen on glass, one specimen per condition. That screen was a practical choice. The screen is in the Appendix III.

2.2 FABRICATION OF THE OXIDE STACK

The piezoelectric oxide is grown on $SrTiO_3$ because the polymer cannot provide the lattice or the growth temperature, as set out in Section 1. The cubic cell of $Sr_3Al_2O_6$ is about four perovskite units across, so one quarter of that cell is the spacing presented to the film [16, 23]. That spacing lies between $SrTiO_3$ and $BaTiO_3$. The barium titanate therefore grows on a closer template than the bare substrate would give, and less elastic strain is stored in the film while the wafer still clamps it. A high-quality $Sr_3Al_2O_6$ film not only delivers a template for the next layer but also favors an even and nearly crack-free release from the substrate. Poorly deposited $Sr_3Al_2O_6$ may contain insoluble compounds that act as stress concentration points during release and could introduce cracks.

The $SrTiO_3$ is heated to 840 °C at 10 °C min^{-1} under 200 mTorr of oxygen and annealed for 15 min. Oxygen is then stopped, and SAO is deposited at the chamber base pressure of approximately 3×10^{-6} torr with a fluence of 1.8 J cm^{-2}, a pulse energy of about 180 mJ, a repetition rate of 4 Hz, and about 1900 pulses (Fig. 2**a**). That pulse count was set from an X-ray reflectivity curve on a calibration film and corresponds to a nominal SAO thickness of about 40 nm. The reflectivity curve is in the Appendix IV.2.

The substrate is cooled to 750 °C at 10 °C min^{-1} without added oxygen, and $BaTiO_3$ is deposited in two stages without breaking vacuum. An oxygen-free capping layer is grown at 750 °C and base pressure, 1.5 J cm^{-2}, 4 Hz, and 850 pulses, nominally about 6 nm. The main layer is grown at 750 °C in 200 mTorr of oxygen, about 150 mJ per pulse, 1.5 J cm^{-2}, 4 Hz, and 14400 pulses, a nominal thickness of 100 nm. The stack is cooled at 20 °C min^{-1} in 200 mTorr of oxygen (Fig. 2**a**). Reflectivity fringes could not be fitted on the released stack, so the $BaTiO_3$ thickness is nominal, based on fringes from a joint $BaTiO_3$ and $Sr_3Al_2O_6$ depositions. Deposition runs that departed from this recipe, in-

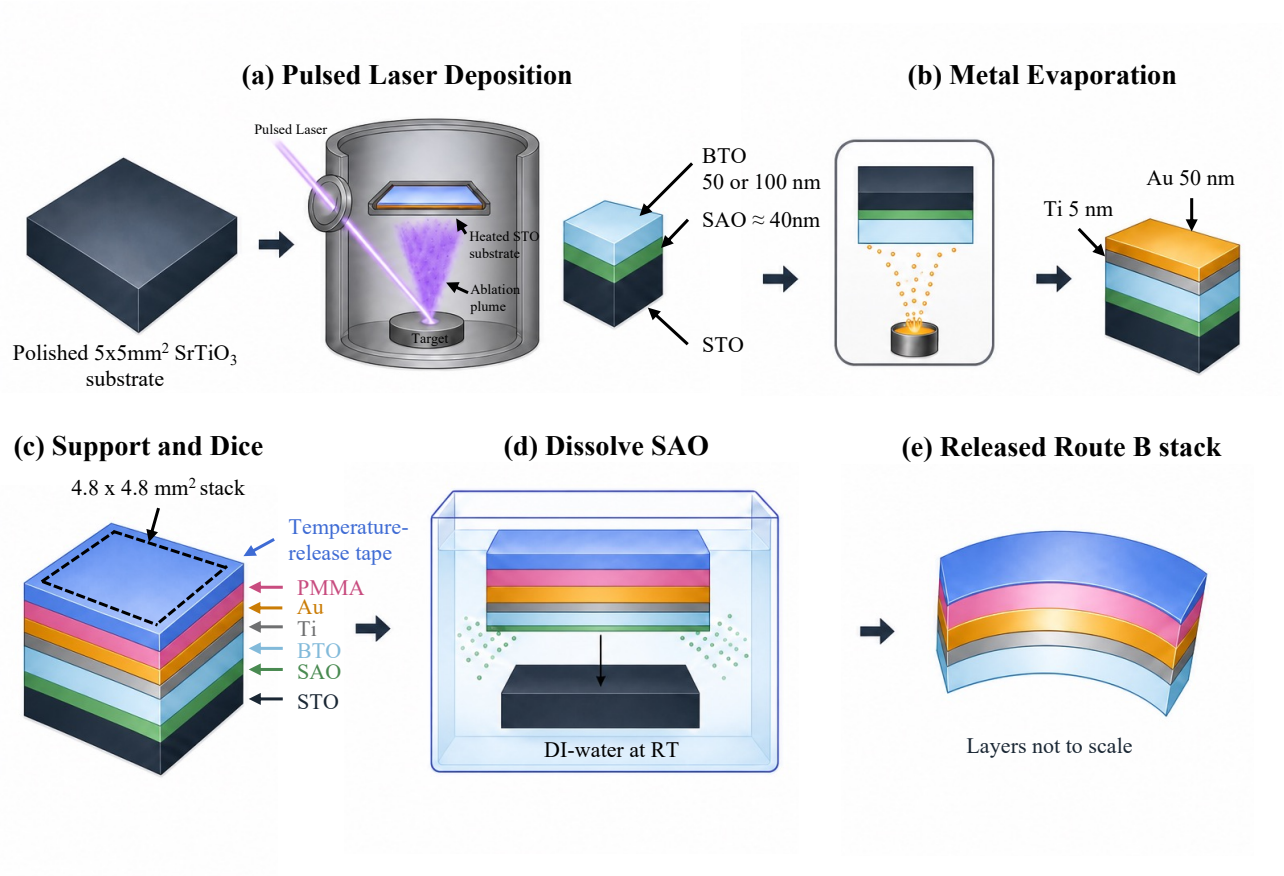


Figure 2: Fabrication and release of the Route B functional stack. **(a)** Pulsed laser deposition of sacrificial $Sr_3Al_2O_6$ (SAO, 40 nm) and $BaTiO_3$ (BTO, 100 nm) on a polished 5×5 mm^2 $SrTiO_3$ (STO) substrate. **(b)** Evaporation of the Ti/Au top electrode (5 nm Ti, 50 nm Au). **(c)** The stack was supported with PMMA, then diced to 4.8×4.8 mm^2, and temperature-release tape was applied. **(d)** Release of the stack was done by dissolving the SAO layer in deionized water at room temperature. **(e)** The released stack dried and attached to the TRT.

cluding runs with no or only a weak $BaTiO_3$ peak, are listed in the Appendix IV.

Titanium and gold are evaporated while the film is still supported on the wafer, so the top electrode is in place before $Sr_3Al_2O_6$ dissolution (Fig. 2**b**, **c**). Titanium is 5 nm at 1 nm s^{-1}, then gold is 50 nm at 2 Å s^{-1}, at a chamber pressure below 1×10^{-6} mbar. This deposition uses an Evatec BAK 501LL, a different evaporator from the VTD Vera 450H used for the bottom gold.

2.3 RELEASE AND ASSEMBLY

After the deposition, the $BaTiO_3$ is still located on the growth substrate. In order to create the desired device, a freestanding thin film is required. To achieve this, an 8% solution of PMMA (950k in anisole, AR-P 672.08) is spin-coated onto the top gold at 6000 rpm and baked at 180 °C for 5 min, creating a 700-nm protective film. The coated film is wet-diced into a 4.8×4.8 mm square so that the SAO edge is exposed to water during the release process (Fig. 2**c**). Temperature-release tape is applied to the PMMA. Dissolving the sacrificial layer to free the oxide is the release introduced in Section 1 [16, 17]. The PMMA film and the tape are the support used here (Fig. 2**c**). The chip is immersed in about 40 mL of room-temperature deionized water, without stirring or water changes, for 24 h (Fig. 2**d**). Once the release is done, the substrate is removed using tweezers. The stack of thin films on the TRT is then dried under a stream of nitrogen (Fig. 2**e**). The release was optimized over time. Earlier releases onto PDMS, or onto tape with no additional PMMA support, are in the Appendix V. Several growth and support variables changed together in those trials and are discussed further in the Appendix V.

Once the films are released, the bottom electrode needs to be functionalized in the same way as the silicon wafer with the gold electrodes, as described in Section 2.1. The entire PDMS platform, including the bottom electrode, is treated again with 0.1 mM MPTMS for 30 min, rinsed with ethanol, and dried with nitrogen. The released functional sheet is aligned by eye to the bottom electrode. The PDMS platform and the exposed $BaTiO_3$ then receive the same oxygen-plasma treatment used to bond the chip to the membrane. The sheet is pressed onto the electrode by hand. Air is pushed through the inlet with a syringe to establish full contact between the membrane and the oxide layer. The final device is held at 70 °C for 30 min for the bonds to establish. To remove the TRT, a clean silicon wafer is heated to 115 °C. When the temperature is reached, the fabricated device is placed tape-side down on the wafer for about 30 s, until the TRT turns from transparent to opaque. Once this change is visible, the TRT is peeled off using tweezers. This step concludes the fabrication process and delivers the desired stack as discussed in Section 1. Later electrical tests required the removal of PMMA. This is done by exposing only the coated face to acetone for about 30 s, then

to ethanol, then to deionized water, and repeating that sequence three times. Assembly is inspected on a Keyence microscope. During release optimization, PMMA was removed before attaching the stack to the TRT, to see the effect of pure gold supported release.

2.4 CHARACTERIZATION METHODS

The sections above describe the fabrication methods and recipes. The following section describes the methods used to characterize the device at different fabrication stages. Furthermore, it explains how process parameters were evaluated during optimization.

X-ray Diffraction

An X-ray diffraction (XRD) scan of the stack, before and after release, is done to determine two changes. First, it validates that the substrate was detached successfully and that the sacrificial layer has dissolved, which is shown by the absence of the material peaks in the scan of the released film. Secondly, the $BaTiO_3$ (00ℓ) reflection remains at a similar angle, meaning the out-of-plane order survives the release process. Additional X-ray diffraction measurements were carried out to improve pulsed-laser deposition parameters.

The X-ray diffraction is measured on functional stacks that belong to the same deposition run. Later depositions were carried out on a 10×10 mm substrate, producing 4 smaller chips with equal layer composition. These chips are then measured before release and again after release and transfer to PDMS. Three pieces from one growth are measured and are called P1, P2, and P3 below, "P" indicating the piezoelectric layer is present. P1 is measured on the $SrTiO_3$ substrate. P2 is measured after release onto PDMS with PMMA still on the top gold. P3 is measured after release and transfer with PMMA removed before the release. In the appendix these pieces are `P260908_2_3`, `P260908_2_4`, and `P260908_2_1`. The scan is a symmetric θ–2θ scan through the $BaTiO_3$ (002) reflection, with a rocking curve of that reflection. The results are discussed in Section 3.2.

Electrical Characterization

In order to evaluate whether there is a piezoelectric response to the pressure change, two gold electrodes are integrated. The in-plane stretch changes the polarization of the $BaTiO_3$ film. This polarization causes charges to build up at the interface of the electrodes which could be measured as an open-circuit voltage. The two gold electrodes are integrated for future characterization of the film. However, this change in voltage could not be seen in the measurements. Due to the absence of an appropriate model of the strain through the layers, no voltage is calculated.

To determine the continuity of the electrical path of the electrode during pressure loading, the resistance is measured in a four-terminal arrangement between the gold pads outside the cavity. This minimizes the resistance reading on the wires and delivers a clear resistance reading of the gold over the cavity. Placing the wires next to the cavity allows the cavity to deform realistically under the given pressure and minimizes the delamination of the copper tape and silver paste used to attach the wires. The results are discussed in Section 3.5.

Bulge Test

In order to replicate the bulge due to pressures in the body, the molded chip is attached to a pressure source, creating a pressure difference across the membrane. While the deflection is small compared with the thickness, the membrane bends. Once the deflection is large compared to the thickness, the center of the film is stretched in its plane. At 40 mbar, the center rise is multiple times larger than the membrane thickness, so the measurements are in that stretching regime. Intracranial pressure can reach up to 3300 Pa in patients with hydrocephalus [24]. This sets the order of magnitude for the experimental chosen pressure values. The series from 0 to 40 mbar is the laboratory protocol set from that pressure.

The bulge is recorded from a side view of the membrane and measured to determine the behavior of the membrane under pressure. Pressure is controlled with a Fluigent Flow EZ Push-Pull controller and the OxyGEN software, from 0 to 40 mbar in steps of 2 mbar and pushes desisted water into the cavity. Each step is held for 60 s. In this way, the membrane has enough time to reach a state of equilibrium, and the image is taken at the end of the hold. After 40 mbar, the pressure returns to 0. This loading cycle is repeated three times, with a zero-pressure image before the first cycle and after each return, to determine repeatability and reproducibility. The results are discussed in Section 3.4. The chip lies on its side, and the inlet tubing (1 mm inner diameter) is pressed into the 1.5 mm hole. Images are taken on an Olympus SZX10 with a Basler camera, illuminated from the objective and captured using Pylon Viewer. The scale is read from the manufacturer's calibration slide in ImageJ, averaged over ten increments. Two points on the image set the baseline of the profile. Edge-finding details and the retest after additional resting days, and the bare-membrane fit are in the Appendix II.5.

3. RESULTS

The previous section explained the fabrication process developed, with the supporting material elaborating the improvement of that process. In the same order as before, this section reports the results that those recipes produced. The result of each step determines whether the next step counts as part of one stack.

3.1 TRANSFER OF GOLD ELECTRODE TO MEMBRANE

After improving the transfer protocol, as described in the Appendix III, the transfer of the gold layer was complete and consistent over multiple trials compared to earlier transfers (Fig. 3). Optically, flakes and incomplete transfers were no longer identifiable, and no PDMS residue was spotted on the donor. The film reached the membrane closer to a continuous sheet with less prominent cracks. The results were analyzed together with the electrode area, the donor

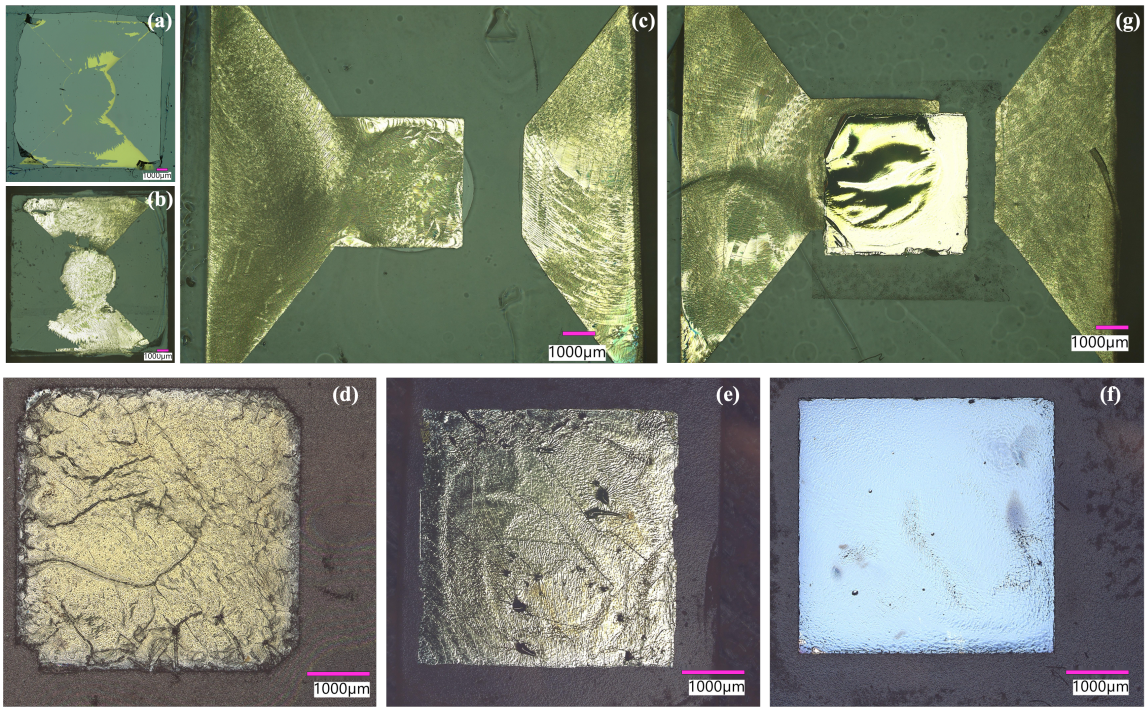


Figure 3: Gold transfer onto the membrane. **(a)** Donor after an early peel, with gold still on the silicon. **(b)** The membrane from that peel, carrying the film in flakes and leaving the corners behind. **(c)** A later transfer, in which the gold on the membrane is closer to a continuous film and the cracks are less prominent. Release of the $BaTiO_3$ sheet. Stack description from bottom to top. **(d)** TRT/PMMA/$BaTiO_3$, no gold. The released film is crossed by a network of wrinkles and a few cracks. **(e)** TRT/Gold/Titanium/$BaTiO_3$, no PMMA. The sheet has fewer wrinkles but more cracks, and a few bubbles are visible. **(f)** TRT/PMMA/Gold/Titanium/$BaTiO_3$ with gold and PMMA. The sheet is continuous, and a few bubbles remain. **(g)** Final assembly with the following structure from bottom to top: PDMS/Gold/$BaTiO_3$/Titanium/Gold/PMMA. Scale bars: 1000 μm

image, and the membrane. The transferred area increased from 56-87% to above 99% see Appendix III.

However, even with a full transfer, the peeling process introduced strain in the film, causing it to crack. To support the claim of a complete transfer and evaluate whether cracks had already permanently damaged the conductance of the film, the resistance across the electrodes was measured. Typically, values reached between 8 and 30 Ω. A lower resistance could hint at a more continuous film, or at cracks in a less critical direction, as cracks along the electrical path are less obstructive than cracks across that path. Later transfers stayed in that form. The electrode outline was changed afterward so the stack would be easier to integrate while maintaining the deposition parameters. The oxide in the next section was grown to be placed on these fabricated bottom gold electrodes.

3.2 $BATIO_3$ RELEASE

To ensure a high-quality $BaTiO_3$ film that releases nearly crack-free, the parameters for $BaTiO_3$ and $Sr_3Al_2O_6$ deposition need to be optimized. The deposition of thin films via pulsed-laser deposition is a widely studied field. When the growth parameters are taken from the literature, one quickly discovers that these parameters are sensitive to the deposition system and chamber. Even though the same KrF laser at 248 nm was used, the oxygen pressures, substrate temperature, and fluence differ between publications [17, 25]. Therefore, the deposition had to be adjusted for the chamber used in order to produce a good-quality sacrificial layer. The evolution of these parameters can be seen in the Appendix IV, together with the diffraction results (Appendix IV.1). Once the process was stable and produced similar films, the parameters were frozen. The nominal layer thickness was fixed to the previously mentioned 100 nm, grown in a two-stage deposition, with sequential titanium and gold evaporation before release. During the optimization process, the samples were used to understand and improve the release step. Films were released directly onto PDMS, then onto Kapton, and later supported with PMMA and temperature-release tape. These trials and results can be found in the Appendix V.

Fabricating the functional layer as described achieves high-quality films that are released and transferred as largely continuous sheets with few cracks. While adding a supportive layer of PMMA as described in Section 2.3 produces visually higher-quality films (Fig. 3**f**) than releases of $BaTiO_3$ deposited under identical conditions with gold alone, as seen in Figure 3**e**, this supportive layer hinders electrical connection to the top electrode, as it acts as an insulator. Furthermore, it adds to the overall stiffness of the device, reducing the deformation of the membrane under the same pressure loading by 0.3 mm (see Appendix II.4). Removing it after transfer often delaminated the $BaTiO_3$. The procedure and results are shown in Appendix V. PMMA left a crack-free continuous sheet, although a few bubbles remained. Solutions to address that compromise are taken up in the discussion.

Figure 4 shows the diffraction of three functional pieces from the same growth (grown on a 10 × 10 mm substrate, then diced). On the substrate, the $SrTiO_3$ reflection is at 46.48°, and a $Sr_3Al_2O_6$ reflection sits near 45.98°. Both released pieces sit at the background at those two angles,

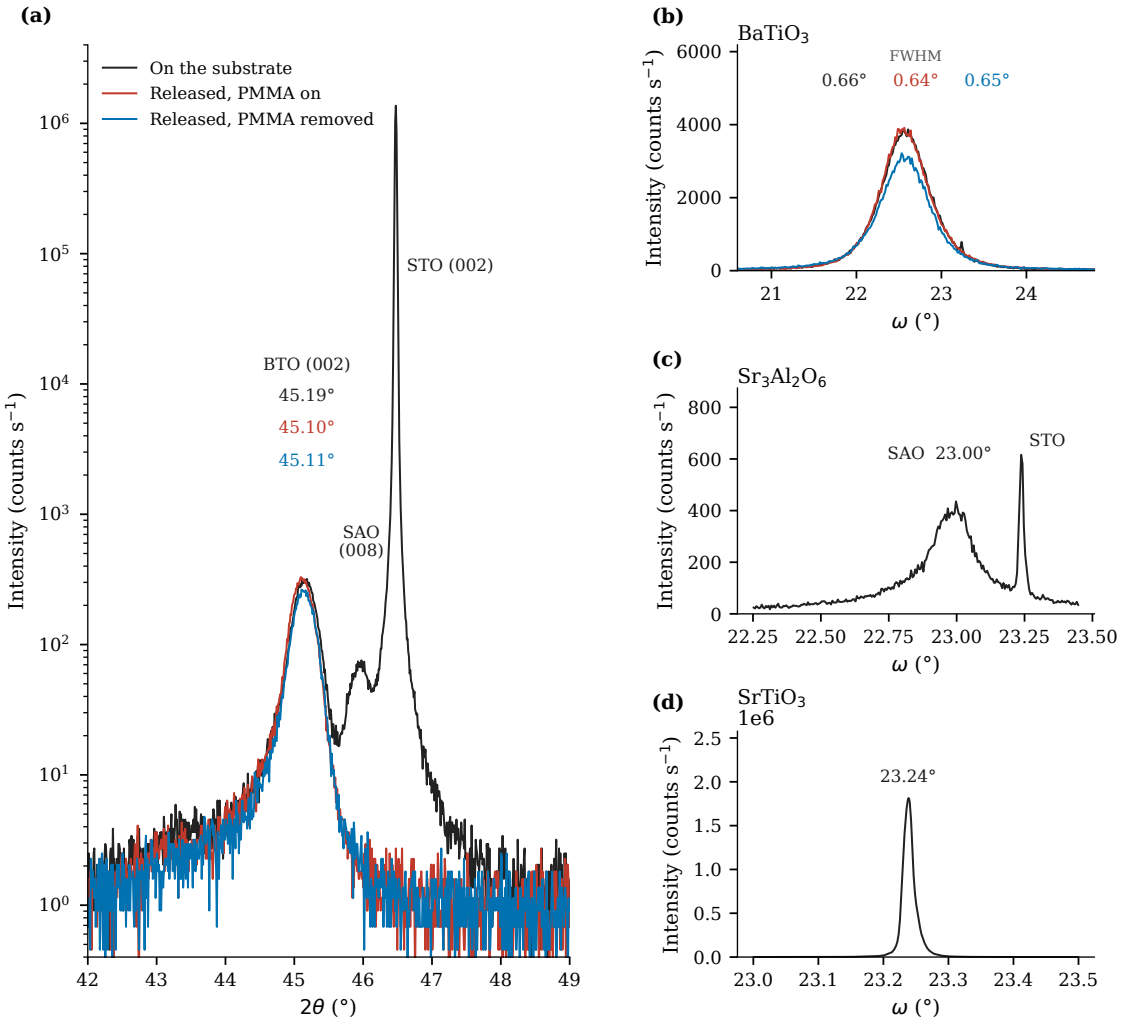


Figure 4: Symmetric scans and rocking curves of three pieces from one growth. **(a)** θ–2θ scans. The $SrTiO_3$ reflection at 46.48° and a small $Sr_3Al_2O_6$ reflection near 45.98° are present on the substrate (P1) and absent after release (P2, P3). The $BaTiO_3$ reflection remains. **(b)** $BaTiO_3$ rocking curves. The widths are 0.66°, 0.64°, and 0.65°. **(c)** $Sr_3Al_2O_6$ rocking scan of P1. The narrow spike is at the same ω as the $SrTiO_3$ rocking peak. **(d)** $SrTiO_3$ rocking curve of P1, 0.018° wide. Black is still on the substrate, blue is released with PMMA, and red is released after the PMMA was removed. Coupled scans are the mean of ten runs and the $BaTiO_3$ rocking curves are the mean of two.

meaning the film has left the substrate and the sacrificial layer is no longer present. The film reflection is at 45.19° on the substrate and at 45.10° and 45.11° after release. The $BaTiO_3$ rocking curves at that reflection are 0.66°, 0.64°, and 0.65° wide. The substrate piece also has a $SrTiO_3$ rocking curve 0.018° wide, and a $Sr_3Al_2O_6$ rocking scan with a broad maximum near 23.0° and a narrow spike at the same ω as the $SrTiO_3$ rocking peak. Due to the absence of the peaks of the substrate and the sacrificial layer, those two scans were not repeated after release (see Fig. 4**a**). A broadening in the rocking curve could be caused by wrinkles in the film or a spread in the tilt of the (00ℓ) planes. The scan does not show that a single crystal was grown, but rather a film with crystals oriented in a preferred direction.

3.3 ASSEMBLY OF THE RELEASED SHEET

After the oxide was released on the TRT, the films were inspected under the Keyence microscope and imaged (Appendix V). The TRT-supported stack was carefully aligned with the bottom electrode to maximize the overlapping electrode areas, which increases the theoretical capacitance of the stack. Fourteen stacks were graded from the Keyence image after transfer based on their continuity. The grade is good, acceptable for testing, or bad (Figure 5). Four were good, eight were acceptable for testing, and two were bad (Table 1). Of the six transferred with PMMA still on the top gold, four were good and two were acceptable for testing. Of the eight transferred after the PMMA had been removed, six were acceptable for testing and two were bad. The eight stacks graded acceptable for testing were used to develop the characterization. A capacitance of the stack was attempted and was not obtained. Where the leads were attached, the bottom electrode was often no longer continuous, and silver paste shorted films that had survived the transfer. The remaining frames and the grading rule are in Appendix V.

3.4 BULGE TESTS

In order to understand the behavior of the PDMS membrane under pressure, membranes were first spanned over a cavity

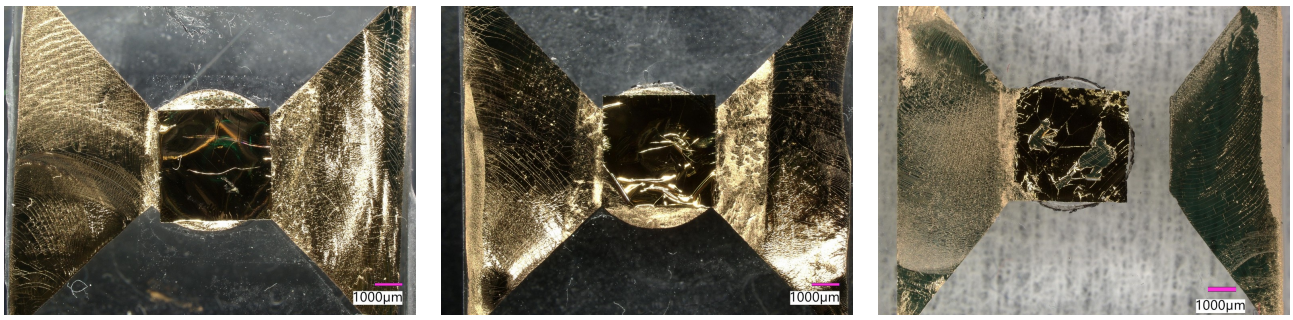


Figure 5: One example of each transfer grade. **(a)** PG2, good. The sheet is continuous across the cavity and PMMA is still on the top gold. **(b)** PG6, acceptable for testing. **(c)** PG13, bad. A large hole occupies the cavity. The grades of all fourteen stacks are in Table 1. Scale bars: 1000 μm.

Table 1: Transfer grade of the fourteen assembled stacks. The grade is the grade after transfer. PMMA means the support was still on the top gold. Acceptable means acceptable for testing. Laboratory identifiers are the names used in the appendix.

Stack	Laboratory ID	PMMA	Grade
PG1	P260708	yes	good
PG2	P260717_1	yes	good
PG3	P260720_1	yes	good
PG4	P260908_1_4	yes	good
PG5	P260716_1	yes	acceptable
PG6	P260722	yes	acceptable
PG7	P260902_1	no	acceptable
PG8	P260908_2_2	no	acceptable
PG9	P260909_1_1	no	acceptable
PG10	P260909_1_2	no	acceptable
PG11	P260909_2_1	no	acceptable
PG12	P260909_2_2	no	acceptable
PG13	P260908_1_2	no	bad
PG14	P260721	no	bad

of ∅ 5 mm without any gold or oxide. The membranes tested had a thickness of 42.60 μm $\pm$ 0.57 μm. At 40 mbar, the mean center deflection is 2.16 mm, on a traced chord of 5.40 mm (Fig. 6, black curve). Above 10 mbar, the within-chip coefficient of variation stays between 1.1 % and 4.6 %, and the between-chip coefficient stays between 6.6 % and 11.5 % (10.4 % at 40 mbar). That rise is the deflection a gold film and an oxide sheet would have to follow, so a thicker coating was spun on the same mold.

These membranes had a thickness of 83.19 μm $\pm$ 0.81 μm and followed the recipe described in Section 2. At 40 mbar, the center deflection is 1.26 mm (Fig. 6, blue curve), on a traced chord of 5.29 mm. From 10 mbar to 40 mbar, the within-chip coefficient of variation falls from 7.7 % to 2.4 %, and the between-chip coefficient stays between 1.2 % and 7.1 % (1.6 % at 40 mbar). These membranes were used to determine the reproducibility and repeatability of this fabrication step. The complete analysis is in Appendix II.3. Membranes mixed at the same ratio and spun at the same speed behave similarly.

Even though the cavity was designed to be ∅ 5 mm, the traced diameter was not the same on every chip. A wider opening reaches a higher center at equal pressure and equal thickness, so the center peak is divided by the traced half-chord. At 40 mbar, that ratio is 0.80 for the 42.60 μm membranes and 0.48 for the 83.19 μm membranes. Added thickness still lowers the bulge after the opening is scaled. The relation between added thickness and reduced deformation is elaborated in Appendix II.5. These bare membranes qualify the measurement bench. They are not the reference for the gold chips.

To determine the impact of the gold electrodes on the deformation behavior, the same measurements were repeated for the result of fabrication route A. G1, G2, and G3 carry only the transferred gold (`GC260923_1`, `GC260923_2`, and `GC260923_3` in the appendix), on the 90.53 μm $\pm$ 0.63 μm

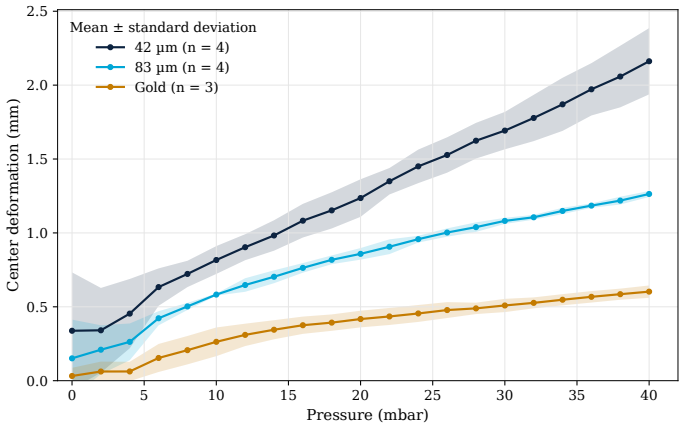


Figure 6: Center deformation against pressure. Each line is the mean of the chip means from the first measurement. The band is the standard deviation of those means. The 42.60 μm group is four chips, and at 40 mbar the mean is 2.16 mm. The 83.19 μm group is four chips, and at 40 mbar the mean is 1.26 mm. The gold group is G1, G2, and G3 on the 90.53 μm coating, and at 40 mbar the mean is 0.60 mm.

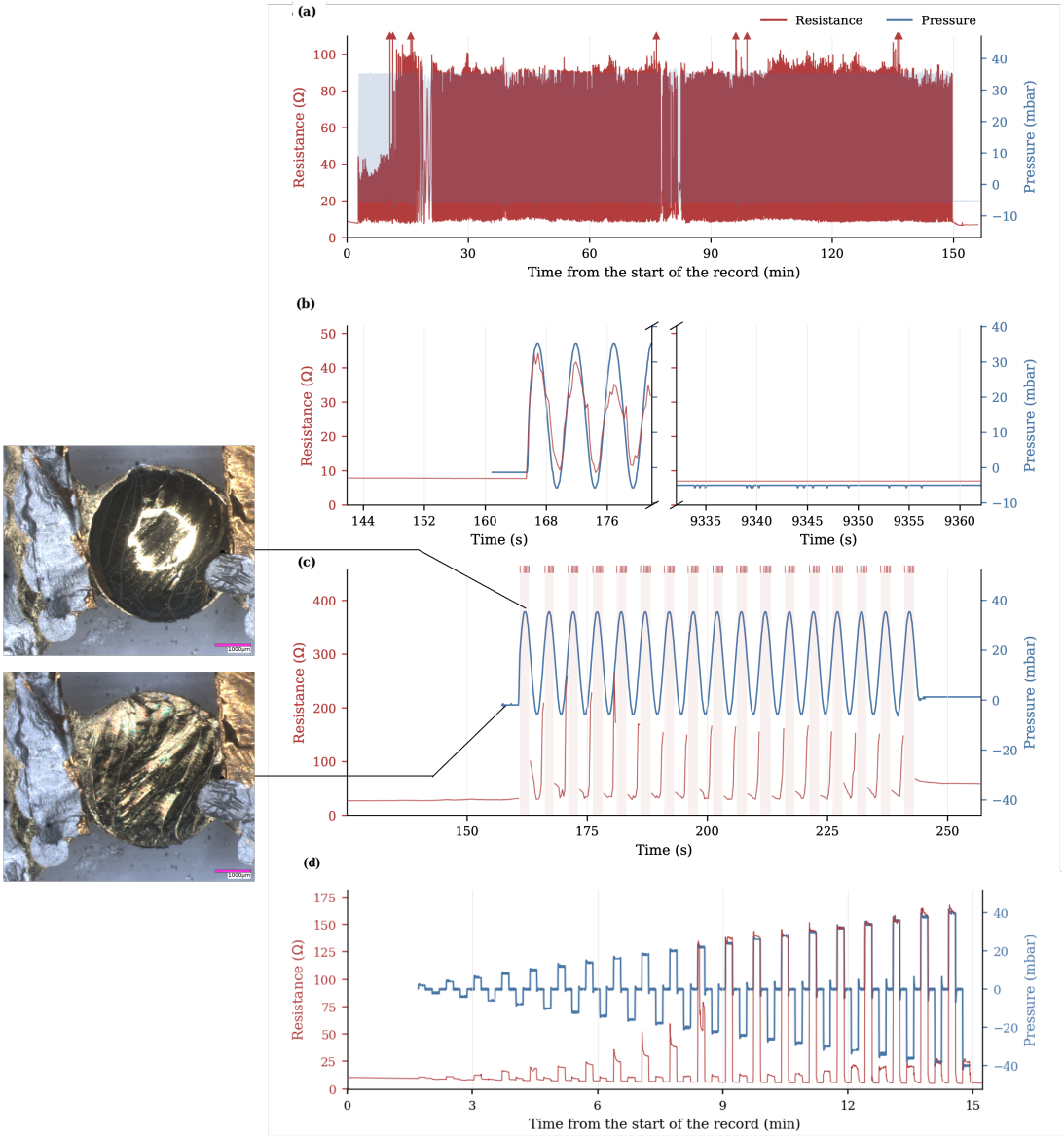


Figure 7: Four-wire resistance during pressure cycling. **(a)** Four-wire resistance of G1. The record, 156 min at 0.2 Hz (ca. 1900 cycles). Resistance and pressure are on one time axis. The pressure is the pale trace. It cycles between about −6 and 37 mbar. Triangles mark resistance readings above 110 Ω. The highest is 511 Ω. The meter does not overload. **(b)** The start and the end, with the middle cut out of the time axis. On the left, the resistance is still near 9 Ω before the pressure cycle begins. **(c)** G2, the opening, in seconds. The meter overloads on the pressure peaks. The first overload is at about 20 mbar. The resting resistance is about 29 Ω. **(d)** G4. The resistance rises with the outward pressure steps, reaches 168 Ω, stays finite, and ends near 5 Ω. The pressure runs between about −40 and 40 mbar.

coating. The electrode spans the cavity, so the gold is present over the whole region over which the membrane stretches. At 40 mbar, the mean center deflections are 0.63, 0.63, and 0.55 mm (Fig. 6, orange curve). The coefficients of variation across the three cycles are 0.5 %, 2.8 %, and 1.9 %, and the between-chip coefficient is 7.0 %. Divided by the traced half-chord, the same peaks are 0.26, 0.27, and 0.26. The mean of the three chips is 0.26, against 0.40 for the bare membrane. Referred to a 5 mm opening, the gold arches are 0.65, 0.67, and 0.68 mm, and the bare chip is 1.01 mm. The gold lowers the arch.

3.5 RESISTANCE OVER CYCLING

To determine whether the transferred gold stays continuous while the membrane is pressurized, the four-wire resistance between the pads outside the cavity was measured on the gold electrodes during cycling. The long record in Figure 7**a** is G1, which carries only the gold from the electrode platform. On that record, the pressure was varied at 0.2 Hz, between about −6 and 37 mbar. The resistance mainly stays inside a band from about 10 Ω to about 100 Ω, with some peaks reaching a resistance as high as 511 Ω. After 156 min, it returns to 9.2 Ω, from a start of 9.0 Ω. The triangles indicate a resistance over 110 Ω, not an overload of the multimeter. The conducting path between the pads therefore survived the ca. 1900 cycles. The same measurement was repeated with other gold electrodes from the same batch and different batches (G4, `GC260911_9 in appendix`), showing no signs of delamination or permanent electrical path opening after 8000 cycles (see Appendix VI.1). When the pressure is cycled sinusoidally, the resistance follows the peaks and valleys with a small lag (Fig. 7**b**, **c**, Fig. 42**c**and Fig. 43**b**). The pressure in the cavity was incrementally

stepped in the positive and negative directions, causing the membrane to deform outward and inward, respectively. It can be seen that the outward bulge increases the resistance more than the inward deformation (Fig. 7**d**).

Since the deformation of the gold chip overstepped the boundary of elastic deformation for gold, breaking of the gold layer is anticipated. However, if the gold layer breaks, the multimeter should output an overload as the resistance is too high to measure. The only gold electrode that showed this was G2, while the other chips did not reflect such an output. Therefore, a control strip was measured in the same setup. In that way, a single conducting path over the cavity can be compared with the electrode design. At small pressures, the resistance increases with increasing pressure proportionally (Fig. 43**b, c**). However, once the pressure is higher than 10 mbar, the electrical path starts to open and the resistance increases drastically after 14 mbar the multimeter displays an overload. The overload appears on the strip, and not on the long gold record, because the strip is a single path. Once that path opens, the meter has no remaining connection to measure. The electrode is a film across the cavity, so the resistance can increase while a path between the pads remains. On G3, it stays between about 4 and 21 Ω. A path along the rim can still keep that reading finite if the gold nearer the center has opened. Compared with G2, where the rim path is exactly on the boundary to the deforming membrane (Fig. 7, photo of electrode), the resistance reaches an overload every time the pressure reaches roughly 20 mbar (Fig. 7**c**). Therefore, an optically continuous film does not by itself guarantee a closed path on every chip. Nevertheless, all chips return to the resting resistance once the pressure is 0 mbar.

A transferred electrode is counted as continuous here when a path between the pads survives pressure cycling and the resistance returns to the baseline at zero pressure. Open-circuit voltage was logged on three fully assembled chips while the membrane was pressurized. The reading stayed within a few millivolts, and no piezoelectric response was logged at a changed pressure. The same floor appears on the noise record, so this is not a piezoelectric output (Appendix VI.2).

4. DISCUSSION AND OUTLOOK

Despite the limitations discussed above, the fabrication process leaves a $BaTiO_3$ layer with a gold contact on each side, integrated on a flexible PDMS membrane. The loss of the $SrTiO_3$ reflection, while the $BaTiO_3$ (002) reflection remains, shows that the out-of-plane order survives the sacrificial release [16]. The sheets of highest quality are those that still carry the PMMA. A polymer support allows a brittle oxide membrane to leave the substrate in one piece [17]. Removing that support is a known way to introduce cracks into the film [18], as the releases in Appendix V show, the $BaTiO_3$ cracks and wrinkles. The pattern depends on the thickness, the support, and the surface onto which the film is transferred [26]. Barium titanate is the oxide released here. Another crystalline oxide can follow only when it tolerates the same sacrificial release and the lattice parameters match. Alternatively sacrificial substrates like Mica can be chosen to improve transfer [27].

Molding, both evaporations, the pulsed-laser growth, and the transfer of the bottom gold were optimized and repeated. The same steps can be adjusted further: the electrode outline can be changed, the $BaTiO_3$ thickness can be set, and the cavity size and the membrane deflection can be chosen. A complete gold transfer from the donor to the membrane, independent of the electrode shape, shows that the transfer itself can be varied. Increasing the number of deposition pulses made the $BaTiO_3$ thicker, and a thicker PDMS membrane or a smaller cavity reduced the deflection. To have an exact thickness of the deposited $BaTiO_3$ and $Sr_3Al_2O_6$ instead of nominal thickness AFM or cross section SEM can be carried out. The cracks left by the peel are the defects that remain in the gold transfer step. A continuous gold film fractures near 1% tension [28, 29], and the membrane reaches that limit twice. During the peel, the elastomer stretches as it leaves the donor and carries the gold with it, so the film cracks where the tension passes that strain. Those are the cracks the peel leaves behind. The same limit appears again when the membrane is pressurized. The rim stays fixed, so the line of material that lay across the chord is drawn out into the arc of the dome. At 40 mbar that arc is 4.2%, 4.6%, and 3.9% longer than the chord on G1, G2, and G3. On all three chips the elongation already exceeds 1% by 16 mbar. A continuous film cannot follow an extension of that size, so the path across the cavity opens and the resistance rises with pressure. Crack-free, continuous gold requires a peel that keeps the tensile strain below the fracture strain of the film. This can be achieved by an additional sacrificial layer below the gold similar to what was done with $Sr_3Al_2O_6$. This could reduce the strain during the transfer. Alternatively a mechanical or fluid-aided peel could set the speed and deformation to limit the stretch of the PDMS, which the present manual peel does not [30, 31, 32]. Furthermore, a rigid plane close to the chip surface could limit the bending during the peel. With regards to the deformation under pressure, a thicker membrane, or a lower mixing ratio of the polymer, reduces that strain at the same pressure and cavity size. The pressure at which the film tears is then higher, which protects the layers from breaking.

The critical step is the bond between the released functional sheet and the bottom electrode. That bond decides whether the two films become one device. During transfer, the receiving surface forms the permanent interface, and the interface forms only when the two surfaces meet [18]. Route A supplies that surface: gold adhered to the PDMS, the oxide stack is placed by hand, full contact is not guaranteed. Pressure applied through the inlet increases the contact area, but it can also introduce wrinkles or cracks. The sheet may already be attached around the circumference while the center is still free. Inflating the membrane then presses the PDMS against the center before the surrounding area has attached. The functional stack limits how far the membrane can move, so the membrane can wrinkle as it attaches to the oxide. When the pressure is released, the membrane relaxes, the wrinkles straighten, and the attached oxide tears. Cracks that appear while the PMMA is removed can come from uneven dissolution and from polymer left behind. Like $Sr_3Al_2O_6$, that residue can concentrate stress and crack the film [15], further more released

parts will relax while unreleased parts can't, this causes the film to curl. The oxide therefore has to be supported while the PMMA is removed, which requires strong adhesion between the oxide and the bottom electrode. No protocol for that adhesion was developed, and the plasma step on the functionalized gold was not followed by a surface analysis. Making the bond and the PMMA removal controllable means measuring that adhesion and analyzing the gold surface after the plasma.

The deflection under pressure is recorded from a side view of the stack. The traced opening, the tilt of the chip, and the shape of the membrane before pressure is applied all change the center height read from the silhouette. Omitting the initial bulge height from a stiffness analysis is a known source of error [33]. In the early measurements that height was present because no vacuum pump was attached, and the membrane was what forced the liquid back. Once the pump was attached, the initial-height offset was no longer observed. At low pressure, air trapped in the cavity can still shift the apparent arch by as much as the deflection itself, and that shift appears in the repeatability and reproducibility of the chips. The membrane is compliant, and the trapped air acts as a damper, so each pressure step takes longer to settle. PDMS is permeable to air, so letting the chip rest at a given pressure gives that air time to leave the cavity before the test. A useful comparison is possible only at higher pressure, where the arch is large enough that chips imaged in the same way agree.

The deflection decreases as the membrane is made thicker, and stacks that still carry PMMA sit much lower at 40 mbar. Stacks from which the PMMA has been removed do not follow that trend, which suggests that those films are damaged. Some electrode designs also leave parts of the cavity uncovered, so the strain is not uniform. The bare PDMS at the sides takes more of the strain, and the stack then deflects more like a bare membrane than like a gold-covered one. The outline can be drawn so the gold spans the whole cavity, which would load the stack more uniformly. None of these measurements gives the strain in the $BaTiO_3$. A uniaxial strain tests of the membranes and the chips would measure together with the bulge test would allow for a better determination of the material properties. Furthermore, a piezoelectric force microscopy measurement would give the piezoelectric coefficients. With these material properties a model of the device can be created and a piezoelectric response calculated. On the finished stack, the corresponding readings are the capacitance, the resistance, the inductance, and the piezoelectric response to a change in pressure. Those readings are also what would allow the chip to be sized to a use [7].

The limits of the resistance measurement became clear when the control strip was measured. Where the gold electrodes cross the whole cavity, the parts bonded to the rigid chip barely deform. Current can still pass along those parts, so the resistance stays finite even at high pressure. The long-term record nevertheless returns to the baseline, and the gold shows no delamination under visual inspection. The rise in resistance still means that the conducting path through the gold over the cavity has been reduced. A deeper cavity would let the membrane deflect inward as far as outward. Both directions stretch the sheet, however, the bending part of the strain changes sign. The resistance already shows that difference: outward pressure raises it more than inward pressure (Appendix VI.1). The small lag between pressure and resistance, and the correlation between them, can be analyzed further in order to build a model that relates the two. Once the bond, the peel, and those readings of the stack are in hand, the same device could be used as a pressure sensor. In the spinal subarachnoid space that reading would bear on cerebrospinal-fluid pressure, which is still obtained by lumbar puncture, and would allow a longer observation without that procedure [34]. Telemetric pressure in the lumbar theca has so far been recorded only through a shunt [35]. A magnetostrictive $CoFe_2O_4$ layer, strain-coupled to the $BaTiO_3$, would make the stack magnetoelectric [36, 37]. Pressure would change the strain in the barium titanate and, through that coupling, the magnetic state of the cobalt ferrite, so an external magnetic field could read the pressure without a wired contact [38]. This development would allow long term wireless measurements of otherwise inaccessible locations. Furthermore, the same deformation of the membrane could stimulate cells mechanically, and the barium titanate electrically increasing the likelihood of STEM-cells differentiating [37, 39].

5. CONCLUSION

The aim was to develop a fabrication route, not a finished sensor or stimulator. The route now places a lead-free oxide, with one gold electrode on each side of the $BaTiO_3$, supported by PMMA, on a soft membrane that can be loaded by a pressure difference. $BaTiO_3$ is the oxide with which this was shown. The pressure-based deformation was characterized, the electrical continuity of the electrodes under pressure cycling was analyzed and the preferred crystal orientation of the $BaTiO_3$ was maintained over the entire fabrication process. The project stops at that stack.

The membrane was shaped with physiological pressure changes as its design condition. The bulge was the laboratory form of that load. A rigid harvester has already been considered for the same fluid pressure [5]. The compliant stack is the soft form of that idea, and it remains a fabrication result.

6. ACKNOWLEDGMENT

Funding: This work was supported by the Justus & Louise van Effen Research Grant. The funders had no involvement in the study design, the analysis and interpretation of results, the writing of this thesis, or the decision to submit it for publication.

The author thanks Dr. Murali Ghatkesar, Dr. Semih Sevim, Dr. Mathieu Mirjolet, who supervised this work, for their advice and guidance throughout the study. The author also thanks the Multi-Scale Robotics Lab at ETH Zürich and Prof. Dr. Bradley Nelson and Prof. Dr. Salvador Pané Vidal for hosting this research and for the feedback and discussion it provided throughout.

Additionally, the author thanks the Binnig and Rohrer Nanotechnology Center (BRNC) and the FIRST CLA for allowing and supporting the work in their clean rooms.

REFERENCES

[1] J.-H. Kim et al. Conformable Piezoelectric Devices and Systems for Advanced Wearable and Implantable Biomedical Applications. In: Annual Review of Biomedical Engineering 2025, 27, pp. 255–282. DOI: 10.1146/annurev-bioeng-020524-121438.

[2] K. Scholten; E. Meng. Materials for Microfabricated Implantable Devices: A Review. In: Lab on a Chip 2015, 15. DOI: 10.1039/C5LC00809C.

[3] E. Song et al. Materials for flexible bioelectronic systems as chronic neural interfaces. In: Nature Materials 2020, 19, pp. 590–603. DOI: 10.1038/s41563-020-0679-7.

[4] E. Elsanadidy et al. Self-sustainable intermittent deep brain stimulator. In: Cell Reports Physical Science 2022, 3. DOI: 10.1016/j.xcrp.2022.101099.

[5] L. Beker et al. Energy harvesting from cerebrospinal fluid pressure fluctuations for self-powered neural implants. In: Biomed Microdevices 2017, 19. DOI: 10.1007/s10544-017-0176-1.

[6] N. Zalewska et al. Flexible Gold Electrodes with Enhanced Adhesion and Electrochemical Performance via Silane-Modified PDMS for Bioelectronics. In: Advanced Electronic Materials 2025, 11, e00444. DOI: 10.1002/aelm.202500444.

[7] N. Almarri et al. Piezoelectric Energy Harvesting and Ultra-Low-Power Management Circuits for Medical Devices. In: Nano Energy 2024, 131. DOI: 10.1016/j.nanoen.2024.110196.

[8] C. Covaci; A. Gontean. Piezoelectric Energy Harvesting Solutions: A Review. In: Sensors 2020, 20. DOI: 10.3390/s20123512.

[9] F.-C. Kao et al. Self-assisted wound healing using piezoelectric and triboelectric nanogenerators. In: Science and Technology of Advanced Materials 2022, 23, pp. 1–16. DOI: 10.1080/14686996.2021.2015249.

[10] M. Smith; S. Kar-Narayan. Piezoelectric polymers: theory, challenges and opportunities. In: International Materials Reviews 2022, 67. DOI: 10.1080/09506608.2021.1915935.

[11] Q. Chen et al. Hybrid Piezoelectric/Triboelectric Wearable Nanogenerator Based on Stretchable PVDF-PDMS Composite Films. In: Applied Materials & Interfaces 2024, 16. DOI: 10.1021/acsami.3c15760.

[12] Y. Yu et al. Biocompatibility and in vivo operation of implantable mesoporous PVDF-based nanogenerators. In: Nano Energy 2016, 27. ISSN: 2211-2855. DOI: 10.1016/j.nanoen.2016.07.015.

[13] M. G. Abdelmageed; A. M. R. Fath El-Bab; A. A. Abouelsoud. Design and simulation of pulsatile blood flow energy harvester for powering medical devices. In: Microelectronics Journal 2019, 86. DOI: 10.1016/j.mejo.2019.02.021.

[14] D. Jiang et al. Emerging Implantable Energy Harvesters and Self-Powered Implantable Medical Electronics. In: ACS Nano 2020, 14. DOI: 10.1021/acsnano.9b08268.

[15] J. Huang; W. Chen. Flexible Strategy of Epitaxial Oxide Thin Films. In: iScience 2022, 25, p. 105041. DOI: 10.1016/j.isci.2022.105041.

[16] D. Lu et al. Synthesis of Freestanding Single-Crystal Perovskite Films and Heterostructures by Etching of Sacrificial Water-Soluble Layers. In: Nature Materials 2016, 15, pp. 1255–1260. DOI: 10.1038/nmat4749.

[17] G. Dong et al. Super-Elastic Ferroelectric Single-Crystal Membrane with Continuous Electric Dipole Rotation. In: Science 2019, 366, pp. 475–479. DOI: 10.1126/science.aay7221.

[18] S. Choo et al. From Oxide Epitaxy to Freestanding Membranes: Opportunities and Challenges. In: Science Advances 2024, 10, eadq8561. DOI: 10.1126/sciadv.adq8561.

[19] M. S. Lim; E. G. Jeong. Developments and Future Directions in Stretchable Display Technology: Materials, Architectures, and Applications. In: Micromachines 2025, 16, p. 772. DOI: 10.3390/mi16070772.

[20] D. Qin; Y. Xia; G. M. Whitesides. Soft lithography for micro- and nanoscale patterning. In: Nature Protocols 2010, 5, pp. 491–502. DOI: 10.1038/nprot.2009.234.

[21] E. H. Tümer; H. Y. Erbil; N. Akdoğan. Wetting of Superhydrophobic Polylactic Acid Micropillared Patterns. In: Langmuir 2022, 38, pp. 10052–10064. DOI: 10.1021/acs.langmuir.2c01708.

[22] I. Byun; A. W. Coleman; B. Kim. Transfer of Thin Au Films to Polydimethylsiloxane (PDMS) with Reliable Bonding Using (3-Mercaptopropyl)trimethoxysilane (MPTMS) as a Molecular Adhesive. In: Journal of Micromechanics and Microengineering 2013, 23, p. 085016. DOI: 10.1088/0960-1317/23/8/085016.

[23] R. Qiu et al. Epitaxial Growth of Pure $Sr_3Al_2O_6$ Sacrificial Layer for High Quality Freestanding Single-Crystalline Oxide Membranes. In: Thin Solid Films 2023, 773, p. 139820. DOI: 10.1016/j.tsf.2023.139820.

[24] A. Di Ieva; E. M. Schmitz; M. D. Cusimano. Analysis of Intracranial Pressure: Past, Present, and Future. In: The Neuroscientist 2013, 19, pp. 592–603. DOI: 10.1177/1073858412474845.

[25] R. Wang et al. Polarization Evolution in Morphology-Engineered Freestanding Single-Crystalline $BaTiO_3$ Membranes. In: Advanced Functional Materials 2022, 32, p. 2112276. DOI: 10.1021/acs.jpcc.2c04404.

[26] R. Mandal; A. Kumar; N. Pryds. Thickness-dependent crack suppression and wrinkle formation in freestanding $BaTiO_3$ membranes. In: Journal of Materials Research 2026. DOI: 10.1557/s43578-026-01965-9.

[27] D. Y. Hyeon; K.-I. Park. Piezoelectric Flexible Energy Harvester Based on $BaTiO_3$ Thin Film Enabled by Exfoliating the Mica Substrate. In: Energy Technology 2019, 7, p. 1900638. DOI: 10.1002/ente.201900638.

[28] S. P. Lacour et al. Stretchable Gold Conductors on Elastomeric Substrates. In: Applied Physics Letters 2003, 82, pp. 2404–2406. DOI: 10.1063/1.1565683.

[29] J. A. Rogers; T. Someya; Y. Huang. Materials and Mechanics for Stretchable Electronics. In: Science 2010, 327, pp. 1603–1607. DOI: 10.1126/science.1182383.

[30] S. Liu et al. Green Fabrication of Freestanding Piezoceramic Films for Energy Harvesting and Virus Detection. In: Nano-Micro Letters 2023, 15, p. 131. DOI: 10.1007/s40820-023-01105-6.

[31] J. Ma et al. Role of Thin Film Adhesion on Capillary Peeling. In: Nano Letters 2021, 21, pp. 9983–9989. DOI: 10.1021/acs.nanolett.1c03494.

[32] P. Li; X. Huang; Y.-P. Zhao. Electro-Capillary Peeling of Thin Films. In: Nature Communications 2023, 14, p. 6150. DOI: 10.1038/s41467-023-41922-2.

[33] M. K. Small; W. D. Nix. Analysis of the accuracy of the bulge test in determining the mechanical properties of thin films. In: Journal of Materials Research 1992, 7, pp. 1553–1563. DOI: 10.1557/JMR.1992.1553.

[34] B. L. C. Wright; J. T. F. Lai; A. J. Sinclair. Cerebrospinal Fluid and Lumbar Puncture: A Practical Review. In: Journal of Neurology 2012, 259, pp. 1530–1545. DOI: 10.1007/s00415-012-6413-x.

[35] S. Khawari et al. Novel Telemetric Pressure Monitoring in Lumbar Theca. In: Brain and Spine 2022, 2, p. 100886. DOI: 10.1016/j.bas.2022.100886.

[36] H. Zheng et al. Multiferroic $BaTiO_3$–$CoFe_2O_4$ Nanostructures. In: Science 2004, 303, pp. 661–663. DOI: 10.1126/science.1094207.

[37] M. Mirjolet et al. Magnetoelectric $BaTiO_3/CoFe_2O_4$ Thin-Film Meshes for Neuronal Differentiation. In: Advanced Science 2026, e77180. DOI: 10.1002/advs.77180.

[38] K. L. Kozielski et al. Nonresonant Powering of Injectable Nanoelectrodes Enables Wireless Deep Brain Stimulation in Freely Moving Mice. In: Science Advances 2021, 7, eabc4189. DOI: 10.1126/sciadv.abc4189.

[39] A. Marino et al. Piezoelectric Nanoparticle-Assisted Wireless Neuronal Stimulation. In: ACS Nano 2015, 9, pp. 7678–7689. DOI: 10.1021/acsnano.5b03162.

[40] H. Hencky. On the Stress State in Circular Plates With Vanishing Bending Stiffness. In: Zeitschrift für Mathematik und Physik 1915, 63, pp. 311–317.

[41] W. B. Fichter. Some Solutions for the Large Deflections of Uniformly Loaded Circular Membranes. In: NASA Langley Research Center, NASA TP-3658 1997.

[42] M. Kim et al. Regulation of corneal stromal cell behavior by modulating curvature using a hydraulically-controlled organ chip array. In: Nature Communications 2025, 16, p. 9944. DOI: 10.1038/s41467-025-64889-8.

[43] T. Ishida et al. Surface-Conditioning Effect of Gold Substrates on Octadecanethiol Self-Assembled Monolayer Growth. In: Langmuir 1997, 13, pp. 4638–4643. DOI: 10.1021/la970241t.

[44] M. A. Moram; M. E. Vickers. X-ray diffraction of III-nitrides. In: Reports on Progress in Physics 2009, 72, p. 036502. DOI: 10.1088/0034-4885/72/3/036502.

[45] H. M. Christen; G. Eres. Recent advances in pulsed-laser deposition of complex oxides. In: Journal of Physics: Condensed Matter 2008, 20, p. 264005. DOI: 10.1088/0953-8984/20/26/264005.

[46] J. Zhang et al. Effect of oxygen pressure on the orientation, lattice parameters, and surface morphology of laser ablated $BaTiO_3$ thin films. In: Thin Solid Films 1996, 287, pp. 101–103. DOI: 10.1016/S0040-6090(96)08736-6.

[47] M. Tyunina; D. Chvostova; A. Dejneka. Optical revelation of defects in epitaxial barium titanate films. In: Physical Chemistry Chemical Physics 2019, 21, pp. 7874–7878. DOI: 10.1039/C9CP00923J.

[48] A. Aidoud et al. Tuning the growth and strain relaxation of ferroelectric $BaTiO_3$ thin films on $SrRuO_3$ electrode: influence on electrical properties. In: The European Physical Journal Applied Physics 2017, 80, p. 30303. DOI: 10.1051/epjap/2017170314.

[49] S. Kondo et al. Significant suppression of island growth in epitaxial (Pb,La)(Zr,Ti)O_3 thin films by two-step growth technique. In: Journal of the Ceramic Society of Japan 2016, 124, pp. 1127–1131.

Supporting Results and Process-Development Evidence

This appendix follows the order in which the route was built. Each section keeps the samples in date order. A cell that was empty in the deposition log is written as not measured. It is not treated as a failed film, and it is not given an empty diffraction panel. One specimen was prepared for most conditions, so a row is a process record, not a replicate.

I. MASK HANDLING AND ELECTRODE DESIGN

I.1 KAPTON MASK FABRICATION

The cavity mold and the electrode masks were cut from the same double-sided Kapton tape on a Speedy 300 laser cutter (Trotec). The laser was run at 100% power and 3% speed. After cutting, the tape was sonicated for 5 min in acetone, rinsed with isopropanol, sonicated for 5 min in isopropanol, rinsed with deionized water, and dried with a nitrogen gun. The tape was supplied at a nominal thickness of 0.13 mm, including one protective liner. Three layers were stacked on top of the laser cutter holder. The layer in contact with the wooden holder was removed after cutting because the surface was too contaminated. The mold that was cast and the shadow mask that was used are two layers thick, a nominal height of 0.26 mm. The cavity depth of the chip was not measured again on the cured chip.

I.2 ELECTRODE DESIGN CHOICES

The electrode is not part of the mold for the chip. It is, however, a Kapton shadow mask, cut with the same laser settings and the same solvent clean, and stuck to the silicon donor before the 50 nm gold evaporation. The electrode design changed over the course of the research, as seen in Figure 8. The gold thickness, the absence of a chromium or titanium adhesion layer, the evaporation rate, and the selected MPTMS immersion were kept when the outline changed.

The blue area in the design seen in Figure 8 is the part that will be removed after cutting. The initial electrode (Fig. 8 **(a)**) was designed to have four contact pads, increasing the chances of an intact electrical path. However, the small distance between the pads made handling of the Kapton masks difficult, with those “arms” ripping off during peeling of the holder. The inner circle is meant to sit over the cavity while the electrode pads are on a non-deforming part of the chip.

To make handling easier, the outline was changed to a bow-tie shape (8**b**). Again the circle was positioned to span over the entire cavity and the pads were placed on a non-deforming part of the chip. This design was used during the deformation measurement of the gold chips GC260923_1, GC260923_2, and GC260923_3. However, both earlier designs had a flaw that did not allow for realistic electrical characterization, because the design required the top electrode to be connected on top of the moving membrane. The connection is done via silver paste, which would have changed the stiffness of the entire stack. To minimize this impact, the electrode pads were split up. This way, a small connection between the oxide stack and the electrode can be applied by silver paste without changing the entire dynamics of the device.

The first trial can be seen in Figure 8**c**. The released stack of BTO, titanium, and gold can be placed on the square bottom electrode. However, since the middle gold electrode square was almost the same size as the diced oxide stack, when silver paste was applied, the cracks in the BTO layer created a short circuit. This is why the final design has a slightly smaller bottom electrode (see Fig. 8**d**) than the diced stack (4.8×4.8 mm), which creates an area underneath the BTO and top electrode where there is no bottom electrode, reducing the risk of electrically shorting the device. The pads remain off the membrane, which is the same reason the bow-tie pads were outside the cavity. The change is there so the stack can be aligned and contacted. It is not a new gold recipe, and it does not change the 5 mm opening that sets the bulge.

II. MEMBRANE DEFORMATION

II.1 SPIN SPEEDS AND THICKNESS

Bare membranes and the membranes that received gold were Sylgard 184 at 20:1, spun on a Polos SPIN 150i. The program was 100 rpm for 10 s, with an acceleration of 1000 rpm s^{-1}, then 55 s at either 1000 or 2000 rpm, with an acceleration of 200 rpm s^{-1}. Nitrogen was supplied during spinning to reduce dust entering the spin coater. The coating was cured at 80 °C for 30 min and left at room temperature for 12 h. For bare membranes, the wafers were functionalized with chlorotrimethylsilane like the PDMS-chips as described in Section 2.1.

Thickness was the mean of four Zygo readings at the peeled boundary. The standard deviation in Table 2 is the scatter of those four points on one coating. Two coatings were spun at each speed. The device membranes in the methods are a

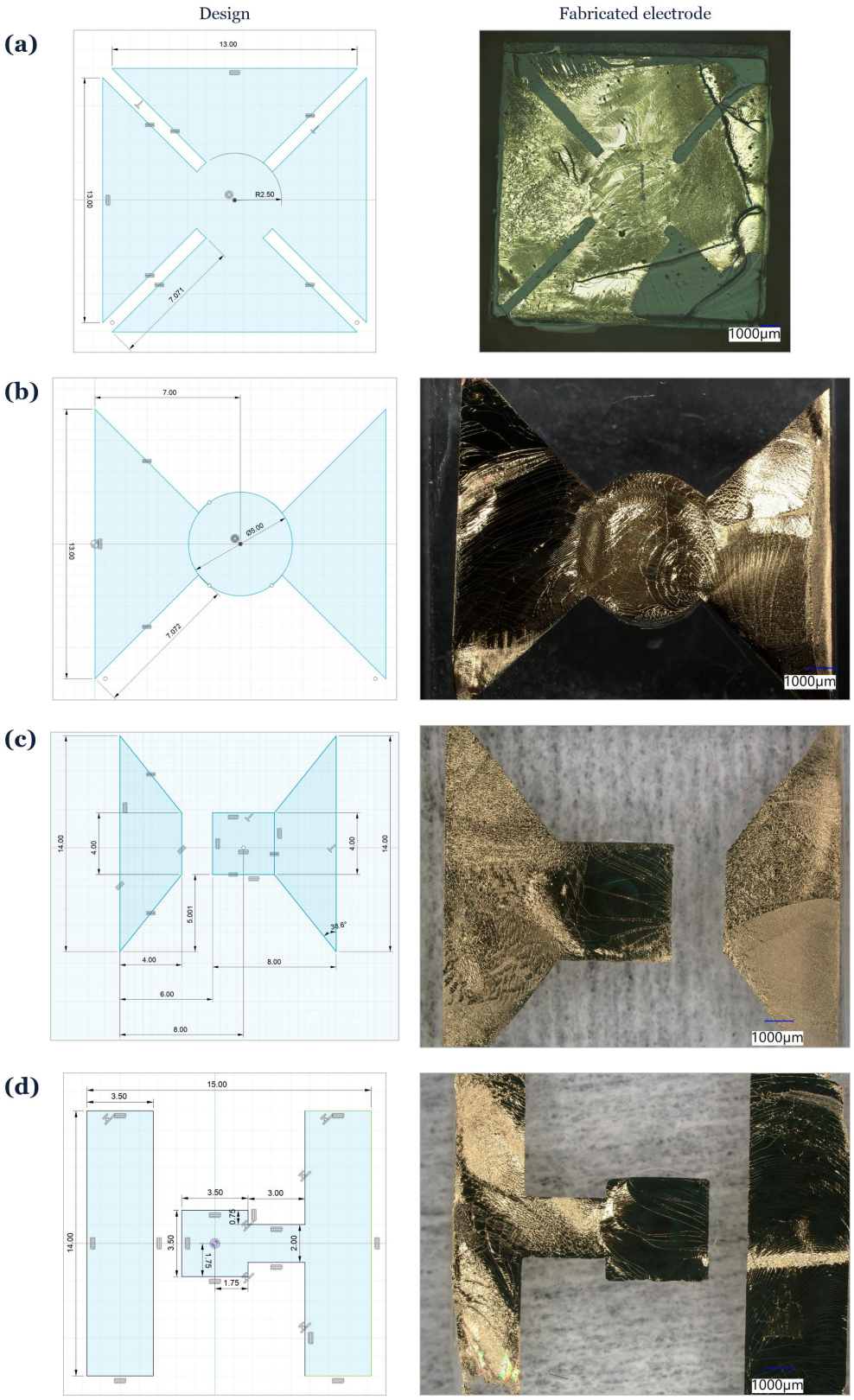


Figure 8: Bottom-electrode designs in the order they were drawn (left, dimensions in millimetres) and an optical micrograph of an electrode made with each design (right, scale bars 1000 µm). (a) First design: a 13×13 mm square cut by four diagonal slits that stop at a 5 mm circle in the centre; chip GC5. (b) Bow-tie: two triangles, 13 mm tall, joined by a 5 mm disc at the centre; chip GC260824_1. (c) Two trapezoidal pads, 14 mm tall and narrowing to 4 mm, with a 4×4 mm square joined to one pad; chip GC260911_3. (d) Final design: a 3.5×3.5 mm square connected to one 3.5×14 mm pad by a 3 mm long, 2 mm wide lead; chip GC260924_2. In (c) and (d) the micrograph is the mirror image of the drawing, because the electrode is seen from the other side after the transfer.

later 1000 rpm coating and are reported there (81.09 ± 2.40 μm). They are not listed in this table. The coating under the gold chips is a later sheet as well. Its four readings are given with the bare chip of that coating, CC261007_2.

Table 2: Spin-coated membranes. The uncertainty is the standard deviation of four boundary readings on that coating.

Spin speed	Coating	Thickness (μm)
2000 rpm	1	42.60 ± 0.57
2000 rpm	2	39.68 ± 2.15
1000 rpm	1	83.19 ± 0.81
1000 rpm	2	81.50 ± 2.27

II.2 HOW THE CENTER RISE IS READ

The membrane is photographed from the side on the bench in Figure 9. Pressure steps and timing are the protocol in the methods. The same bench is used for the bare coatings, the gold chips, and the stacks. Guided traces add clicks along the membrane, and the profile follows those points. A PyTorch model trained on the guided clicks fills in the edge between the same two endpoints. When the edge is found automatically, the two endpoints are still set by hand. The code straightens the band between them so the baseline lies flat, and the model returns the membrane height along that band. Those heights are drawn back onto the frame. Those automatic traces are the learned traces used below wherever a run has them.

A form correction is then applied to that curve. The predicted edge is compared with a smooth arch pinned at the two endpoints, the shape a pressurized membrane takes. A local jump that leaves that arch, such as a speck or a reflection on the membrane, is pulled back onto it. The correction stabilizes the curve and removes those artifacts.

The two endpoints also set the chord, the distance between them. Half of that distance is the half-chord. The cavity is molded at 5 mm, but the traced chord is not 5 mm on every chip, because the marked edge is not always the rim. At 40 mbar the center rise is large compared with the thickness. Where the pressure is carried by stretching, that rise grows with the half-chord to the power $4/3$ [40, 41], so a wider opening of the same thickness rises farther.

Scaling each rise to a 5 mm opening takes that difference in cavity size out, and a thicker coating can then be compared with a thinner one on the same opening.

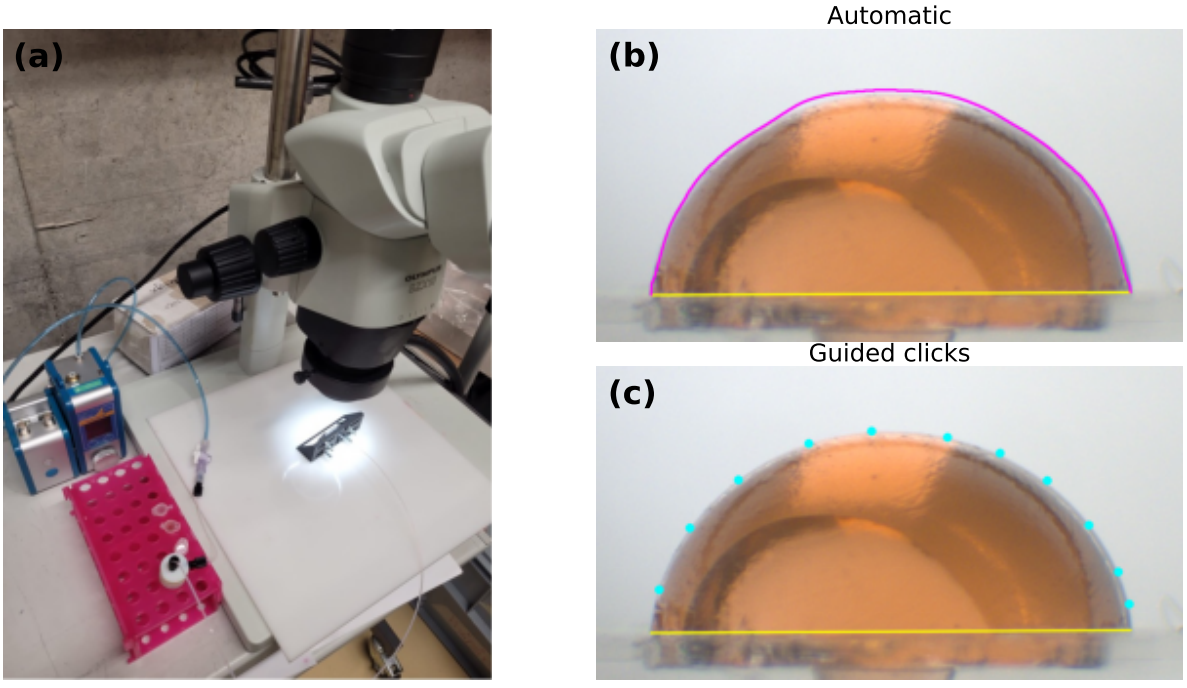


Figure 9: Side-view bulge measurement. **(a)** The bench. The chip lies on its side under the stereo microscope. **(b)** Edge filled in by the trained model on one 40 mbar frame. The yellow line is the baseline. **(c)** Guided clicks on the same frame.

II.3 BARE PDMS DEFORMATION

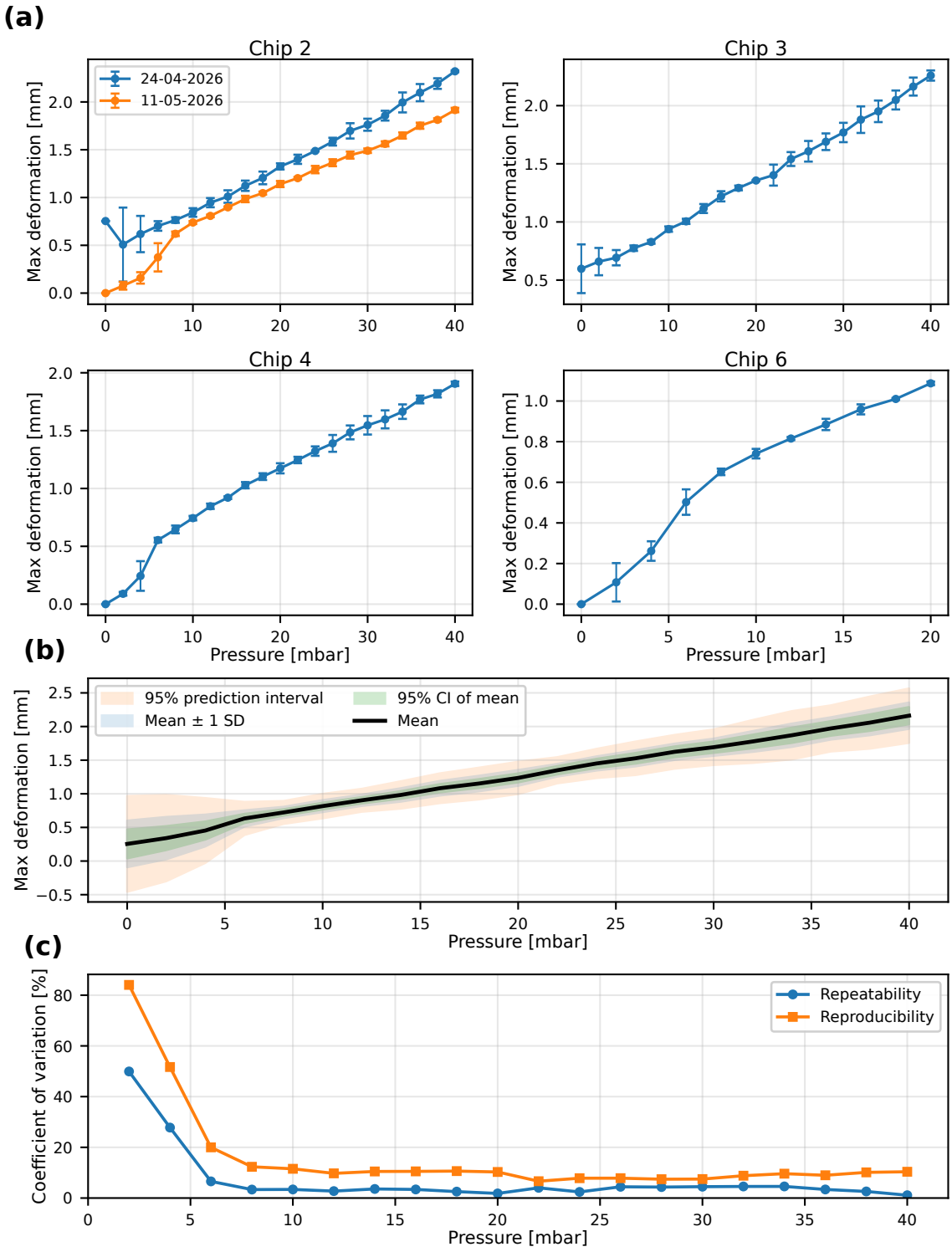


Figure 10: Center rise of the 42.60 μm membranes. **(a)** Session mean of each chip, with the same arrangement as the separate chip panels. The bar is the standard deviation of the cycles at that pressure. Chip 2 has a second curve from the session 17 days later. Chip 6 ends at 20 mbar. Chip 2 on 24 April and Chip 3 still sit above zero at the first pressure step; that offset was kept. **(b)** Mean of the first session. The bands are the 95% prediction interval, the mean ± 1 standard deviation, and the 95% confidence interval of the mean. Above 20 mbar the mean is Chips 2, 3, and 4. **(c)** Repeatability is the mean within-chip coefficient of variation, and reproducibility is the coefficient of variation of the chip means. Both are large below about 5 mbar, where the rise is still small. From 10 mbar to 40 mbar the within-chip coefficient stays between 1.1% and 4.6%. The between-chip coefficient stays between 6.6% and 11.5%, and it is 10.4% at 40 mbar.

The thinner coating was measured first (Fig. 10). At 40 mbar its mean center rise was 2.16 mm, on a traced chord of 5.40 mm. In panel (c) both coefficients fall once the center rise is established. Above 10 mbar the cycles on one chip stay close, and the spread between chips stays wider than that cycle-to-cycle scatter. Chip 2 was measured again after 17 days. At 40 mbar its center rise fell from 2.32 mm to 1.92 mm, and the later curve lies below the first. One explanation is that cross-linking continued and the membrane stiffened.

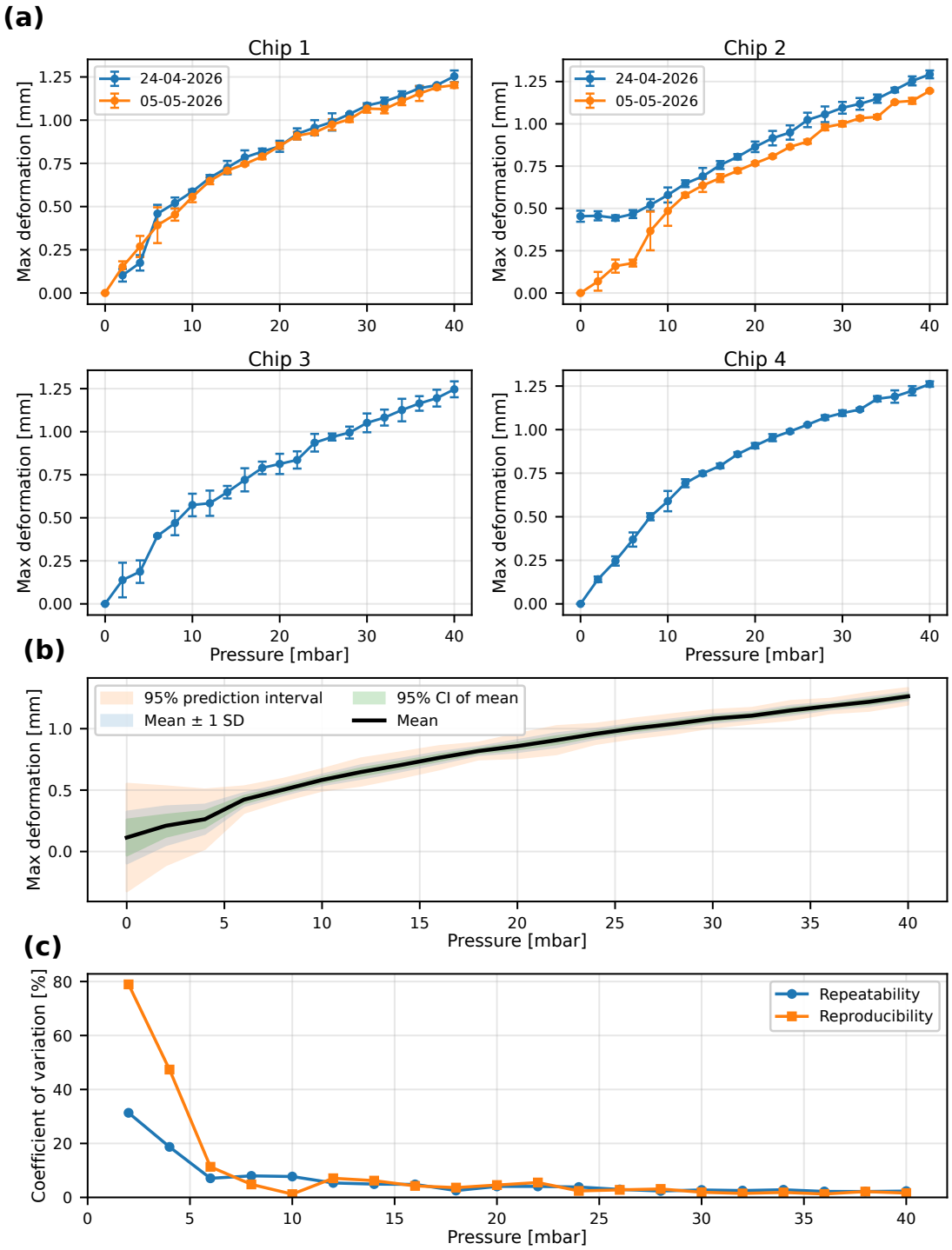


Figure 11: Center rise of the 83.19 μm membranes. **(a)** Session mean of each chip. The bar is the standard deviation of the cycles at that pressure. Chips 1 and 2 have a second curve from the session 11 days later. Chip 2 on 24 April still sits above zero at the first pressure step; that offset was kept. **(b)** Mean of the first session. The bands are the 95% prediction interval, the mean ± 1 standard deviation, and the 95% confidence interval of the mean. **(c)** Repeatability is the mean within-chip coefficient of variation, and reproducibility is the coefficient of variation of the chip means. Both are large below about 5 mbar, where the rise is still small. From 10 mbar to 40 mbar the within-chip coefficient falls from 7.7% to 2.4%. The between-chip coefficient stays between 1.2% and 7.1%, and it is 1.6% at 40 mbar.

A thicker coating was spun on the same mold to bring the rise down (Fig. 11). At 40 mbar its mean center rise was 1.26 mm, on a traced chord of 5.29 mm. In panel (c) both coefficients fall as the center rise grows. Repeatability keeps easing toward 40 mbar, and the spread between chips stays small over the upper half of the range. Chips 1 and 2 were measured again after 11 days. At 40 mbar Chip 1 went from 1.25 mm to 1.20 mm, and Chip 2 from 1.29 mm to 1.20 mm. Both later curves still follow the first session. Dividing the center rise by the traced half-chord gives 0.80 and 0.48 for the two thicknesses at 40 mbar.

The three later sessions sit below the first. Continued cross-linking after the cure would stiffen the sheet and lower the rise, which is the change on all three chips. The curves used in the thickness comparison and in the stress reduction are the first sessions.

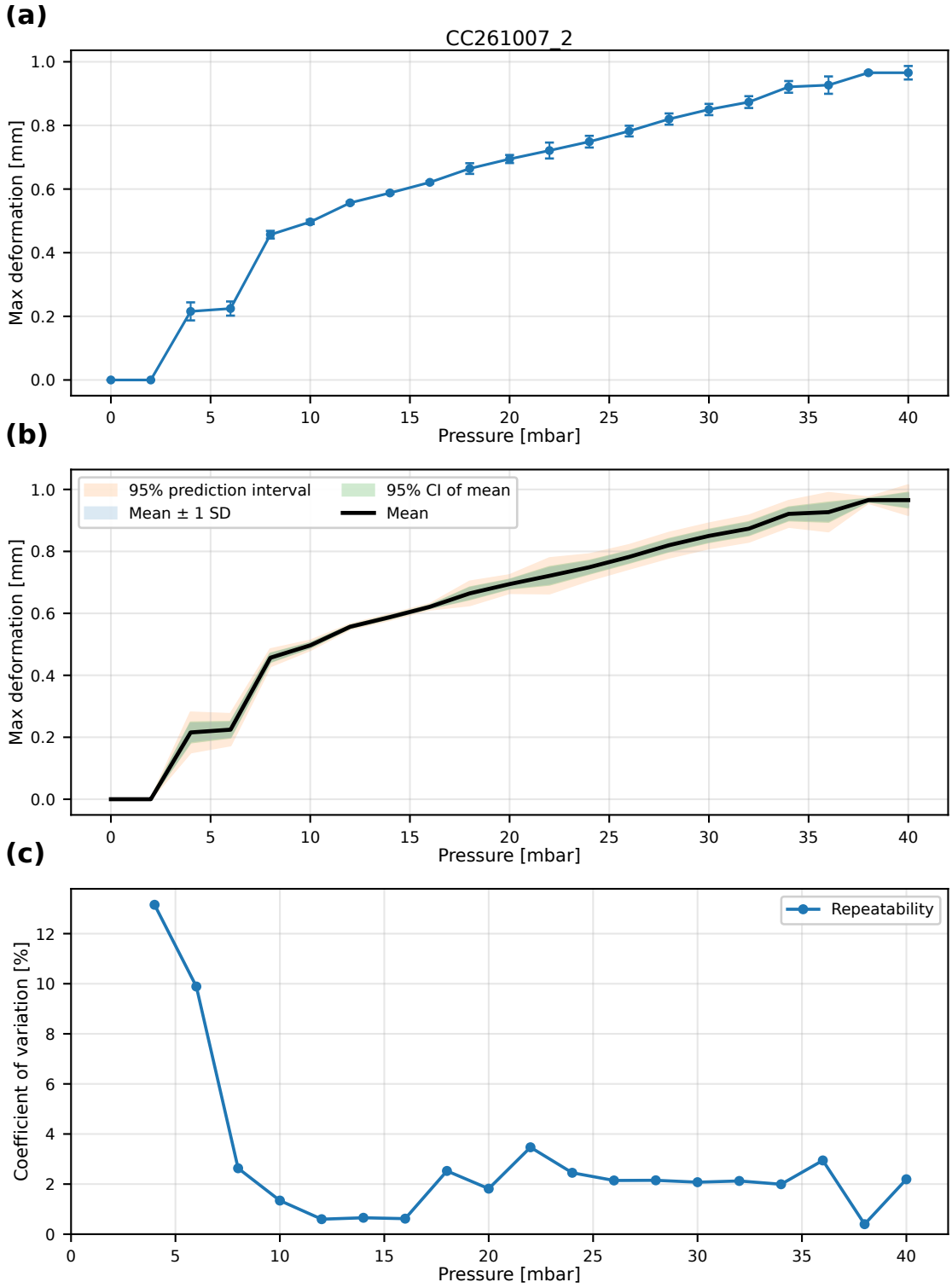


Figure 12: Center rise of CC261007_2, the 90.53 μm coating. **(a)** Mean of the three cycles. The bar is their standard deviation at that pressure. **(b)** Mean of the three cycles. The bands are the 95% prediction interval, the mean ± 1 standard deviation, and the 95% confidence interval of the mean. **(c)** Within-chip coefficient of variation. One chip does not give a between-chip value. At 40 mbar the coefficient is 2.2%.

CC261007_2 is the bare chip of the coating that later received the gold. The four Zygo readings on that coating were 91.21, 90.88, 90.17, and 89.85 μm, a mean of 90.53 ± 0.63 μm. At 40 mbar the three cycles return 0.95, 0.95, and 0.99 mm, a mean of 0.97 mm of center peak deformation, with a coefficient of variation of 2.2%. The three chords at that pressure are 4.81, 4.86, and 4.81 mm. Figure 12 shows the three cycles. The chip panel is their mean, and the bar is the standard deviation of the three cycles. The coefficient plot is the within-chip coefficient. One chip does not give a between-chip value. This chip is the empty sheet for the gold comparison.

II.4 GOLD CHIPS AND RELEASED STACKS

These chips were measured on the same bench using the same pressure protocol and detection scripts. The traced chord varies from chip to chip. Two readings take that opening out. One is the center rise divided by the traced half-chord. The other refers the same rise to a 5 mm opening with the $4/3$ scaling already used for the bare coatings.

GC260923_1, GC260923_2, and GC260923_3 carry only the transferred gold on a 90.53 ± 0.63 μm PDMS membrane. The gold covers the entire cavity, leaving no bare PDMS. GC260923_1 and GC260923_3 use the automatic membrane detection script. GC260923_2 has no learned traces, so the guided traces are used. At 40 mbar the mean center rises are 0.63, 0.63, and 0.55 mm. The within-chip coefficients of variation are 0.5%, 2.8%, and 1.9%. The traced chords are about 4.86, 4.75, and 4.31 mm. Divided by the half-chord, the rises are 0.26, 0.27, and 0.26, and the mean of those three ratios is 0.262. Referred to a 5 mm opening, the same three rises are 0.65, 0.67, and 0.68 mm. The bare chip of this coating is 0.40 of its half-chord and 1.01 mm on that same opening, so the gold film lowers the referred arch from 1.01 mm to 0.65–0.68 mm. In panel (e) of Figure 13 both coefficients fall as the pressure rises, as they do on the bare coatings. The tension that belongs to this flatter arch is calculated in Section II.7.

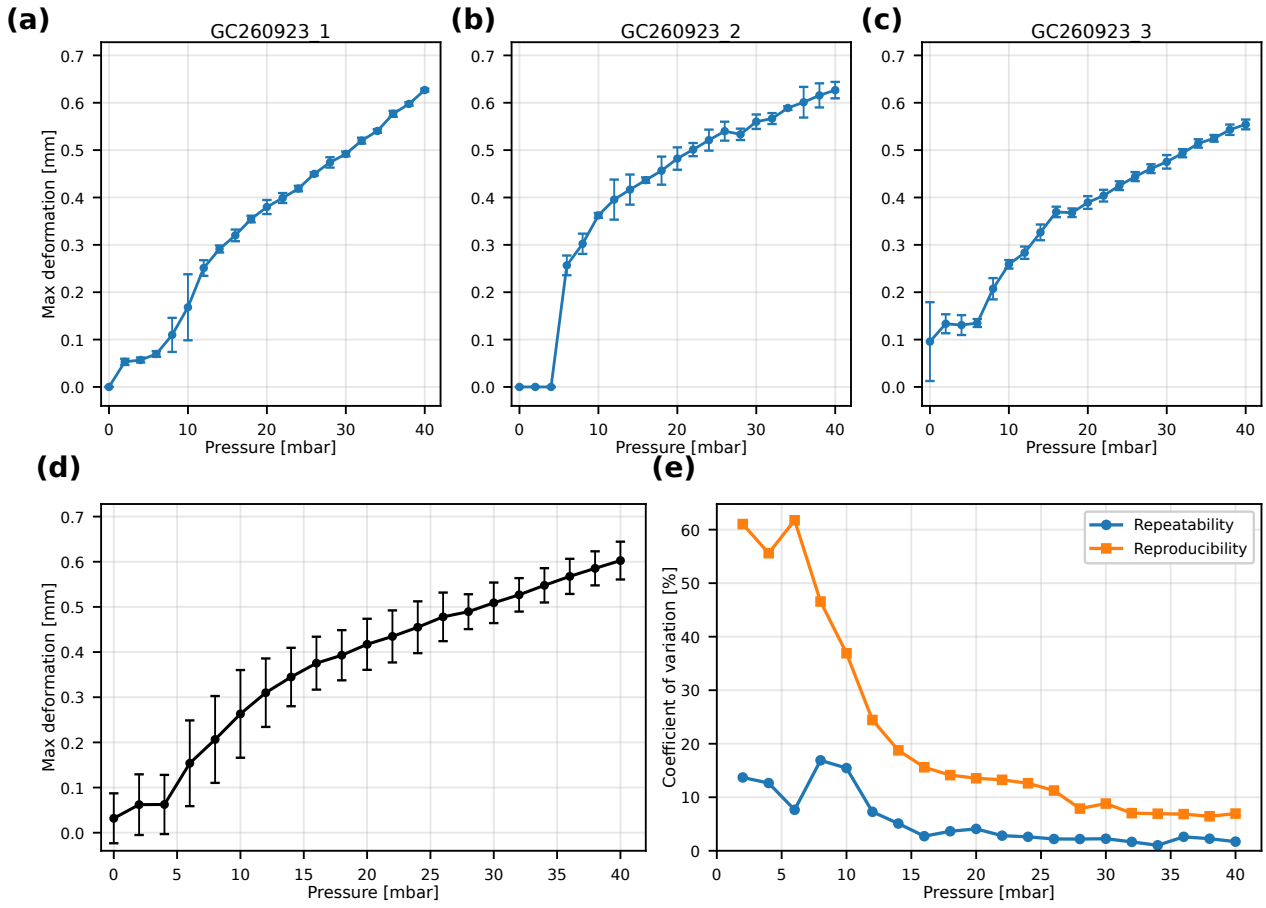


Figure 13: Center rise of the gold-covered membranes. **(a)**–**(c)** GC260923_1, GC260923_2, and GC260923_3. The point is the mean of the three cycles and the bar is their standard deviation. GC260923_2 stays near zero through the first pressure steps. **(d)** Mean of the three chips. The bar is the standard deviation of the three chip means. **(e)** Repeatability is the mean within-chip coefficient of variation, and reproducibility is the coefficient of variation of the chip means. Both are large at the first pressure steps, where the rise is still small. From 10 mbar to 40 mbar the within-chip coefficient falls from 15% to 1.7%. The between-chip coefficient falls from 37% to 7.0%.

The stack chips measured after PMMA removal are P260908_2_2, P260909_1_1, P260909_2_1, and P260909_2_2 (Fig. 14). One Zygo reading on each of these membranes gave 78.02, 78.39, 80.16, and 81.73 μm, a mean of 79.58 ± 1.71 μm. That membrane is thinner than the 90.53 μm coating under the gold. The released stack covers only part of the opening, while the gold covers all of it. Where a learned trace exists, it is the curve that is drawn. At 40 mbar the chip means, in the order named above, are 0.597, 0.704, 0.651, and 0.739 mm, on traced chords of 4.12, 4.34, 4.34, and 4.28 mm. Divided by the half-chord, the rises are 0.29, 0.32, 0.30, and 0.35. Referred to a 5 mm opening, they are 0.77, 0.85, 0.78, and 0.90 mm. On that opening the empty 83.19 μm membranes reach 1.17 mm, and the gold chips stay at 0.65 to 0.68 mm. The released stacks sit between those two.

A continuous oxide on the gold would be expected to lower the rise from the gold chips. These four chips rise above them. The stack membrane is thinner than the gold coating, and the film covers only part of the opening, so bare PDMS remains in the loaded span. P260909_2_1 and P260909_2_2 were scored acceptable for testing, with flakes and an

incomplete sheet. Those rises, and the rises of the other two released chips, are not the stiffness of a continuous $BaTiO_3$ film. No strain in the oxide is taken from them.

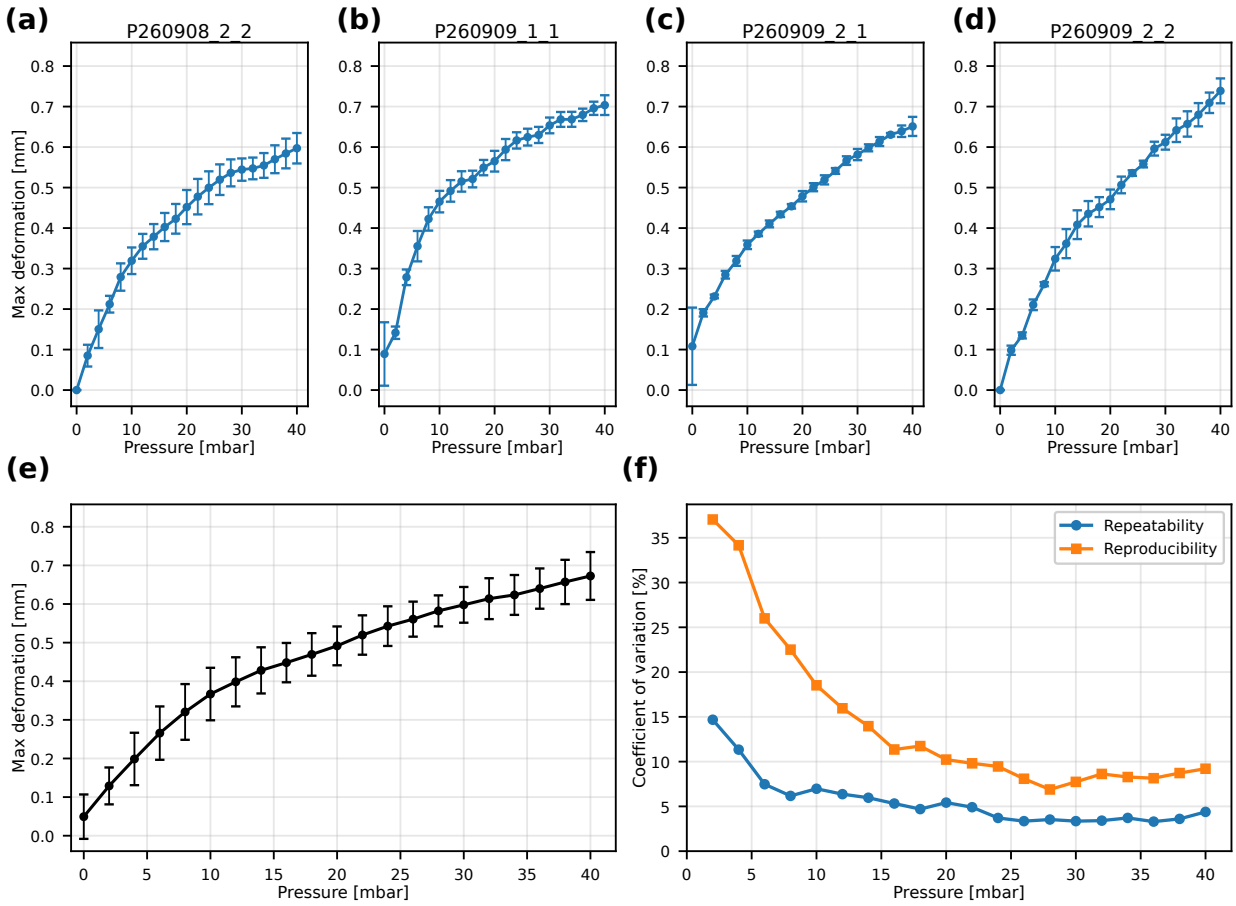


Figure 14: Center rise of the stacks without PMMA. **(a)–(d)** P260908_2_2, P260909_1_1, P260909_2_1, and P260909_2_2. The point is the mean of the three cycles and the bar is their standard deviation. **(e)** Mean of the four chips. The bar is the standard deviation of the four chip means. **(f)** Repeatability is the mean within-chip coefficient of variation, and reproducibility is the coefficient of variation of the chip means.

P260908_1_4 was measured with the PMMA still on the stack and was scored good. At 40 mbar the mean center rise is 0.30 mm and the within-chip coefficient of variation is 17%. The support layer is still in place, so this rise is kept separate from the released stacks.

II.5 CENTER RISE AGAINST THICKNESS

Two coatings are enough to try a relation between thickness and center rise at one pressure. CC261007_2, the 90.53 μm chip above, is the third thickness. At 40 mbar the first-session center rises are 2.16 mm at 42.60 μm, 1.26 mm at 83.19 μm, and 0.97 mm on the 90.53 μm chip. The traced openings are not the same, so the comparison uses the peak referred to a common half-chord, as set out above. Each chip is scaled to a 5 mm opening, and the chips of one thickness are then averaged. For the 90.53 μm chip the mean of the three 40 mbar chords is 4.83 mm, and that step lifts 0.966 mm to 1.01 mm. The scaled means are 1.95, 1.17, and 1.01 mm.

For a clamped circular membrane the bending stiffness is left out, and the pressure is carried by in-plane stretch. This approximation can be chosen as the rise is 11 to 51 times the thickness of the membrane at 40 mbar. Hencky's solution, in the form given by Fichter, then makes the center rise at fixed pressure and fixed opening proportional to the thickness to the power $-1/3$ [40, 41]. Only the scale of that curve was fitted to the three means. It does not follow them. The 42.60 μm coating stands 0.31 mm above the curve, and the 90.53 μm coating stands 0.26 mm below it.

The power $-1/3$ holds when the coatings share one modulus. At fixed pressure and fixed opening the center rise depends on the product of modulus and thickness,

$$w = C(\nu)\left(\frac{p}{Et}\right)^{1/3} a^{4/3},$$

so a change in E moves the rise by the same power as a change in t [40, 41]. One modulus was fitted to each chip on its own, to the mean of its three runs, at pressures above 14 mbar, with Poisson's ratio fixed at 0.49. Chips 2, 3, and 4 of the 42.60 μm coating, on openings of 5.30–5.45 mm, give 0.15, 0.14, and 0.21 MPa. Chips 2, 3, and 4 of the 83.19 μm

coating, on openings of 5.29–5.40 mm, give 0.31, 0.37, and 0.29 MPa. A factor of two in modulus changes the rise by $2^{1/3} = 1.26$, which equals $(83.19/42.60)^{1/3} = 1.25$. The thinner coating is also the softer one, so a curve that varies only the thickness sits below it, and the thicker coatings sit below that curve in turn. On one chip the same solution, fitted from 16 to 40 mbar, lies above the three-run mean at 16 mbar and below it at 40 mbar. Those residuals are several times the standard deviation of the three runs.

II.6 SIDE-VIEW RADIUS AND MEMBRANE STRESS

The center rise used above is one height taken from the side-view trace. The same trace fixes the shape of the dome, and the pressure in the file name fixes the load. The pressure and the radius together fix the tension in the sheet. Kim and co-workers measure a pressurized membrane from the side in the same way. They mark the apex and the two points where the dome meets the baseline, and they compute the angle of that dome from the circular-segment formulas [42]. The chord c is the distance between those two ends. The height h is the apex above the ends. The circle that passes through the three points has radius

$$R = \frac{h}{2} + \frac{c^2}{8h},$$

and the angle at the center of that circle is

$$\alpha = 2\arcsin\left(\frac{c}{2R}\right).$$

The center of the circle sits below the opening, so R is longer than $c/2$.

Figure 15 is that reduction for the 83.19 μm Chip 1 at 40 mbar, first session. The guided trace is folded about its midpoint, and no outer-edge mean is removed. The chord is 5.23 mm and the height is 1.25 mm, so

$$R = \frac{1.247}{2} + \frac{5.232^2}{8 \times 1.247} = 3.368 \text{ mm}.$$

The segment angle is 102°. Half the chord on this frame is 2.616 mm.

On that circle the pressure and the radius set the tension, the force per unit length of a cut through the sheet,

$$N = \frac{pR}{2}.$$

Forty millibar is 4000 Pa, so

$$N = \frac{4000 \times 0.003368}{2} = 6.74 \text{ N m}^{-1}.$$

The membrane stress divides this tension by the Zygo thickness of the coating,

$$\sigma = \frac{N}{t} = \frac{6.74}{83.19 \times 10^{-6}} = 81.0 \text{ kPa}.$$

On the circle the hoop stress and the meridional stress are this same value. Kim and co-workers show the two stresses separating near the clamp, and that separation comes from a finite-element model of the curved sheet [42]. The clamp layer is not reconstructed here. The stress reported below is the membrane stress of the measured circle.

The same four quantities, chord, height, radius, and stress, were read on every first-session trace above 10 mbar. Below 10 mbar the height is still a small fraction of the chord. A small change in h then moves $c^2/(8h)$ by a large amount, and the radius stops being a stable reading. That is the same range in which the coefficients of variation in Section II.3 settle.

At 40 mbar Chips 1 to 4 of the 83.19 μm coating give tensions of 6.74, 6.86, 7.05, and 6.88 N m^{-1}, and stresses of 81, 82, 85, and 83 kPa. Chips 2, 3, and 4 of the 42.60 μm coating give tensions of 5.50, 5.46, and 5.78 N m^{-1}, and stresses of 129, 128, and 136 kPa. The thinner sheet rises higher, so its circle is tighter and its tension is lower. Its stress is higher because that tension is carried by about half the thickness. The same order, lower tension and higher stress on the thinner coating, holds from 12 to 40 mbar.

This balance assigns the whole pressure to tension in the sheet. Hencky's solution, in the form given by Fichter, makes the same assignment and then predicts the center rise from one modulus [40, 41]. Bending is left out. The edge is immovable, the load is taken as vertical, and the sheet is taken as flat before the pressure is applied. Poisson's ratio was fixed at 0.49. A free ratio sat on the bound in the profile fits, so the fixed value is not a measured Poisson's ratio. One modulus was then fitted to the mean center rise of each coating above 10 mbar, on the median traced chord.

The fitted values are 0.19 MPa for the 42.60 μm coating and 0.35 MPa for the 83.19 μm coating. They are the effective moduli of that stretching solution. The two coatings do not return one value, so the pair is not a Young's modulus of the silicone [33]. The side-view stress is the reading kept. It uses the measured circle at each pressure. The stretching solution is the check that one modulus does not describe both thicknesses. The same reduction, applied to the bare 90.53 μm chip and to the gold chips on that coating, is the comparison in Section II.7.

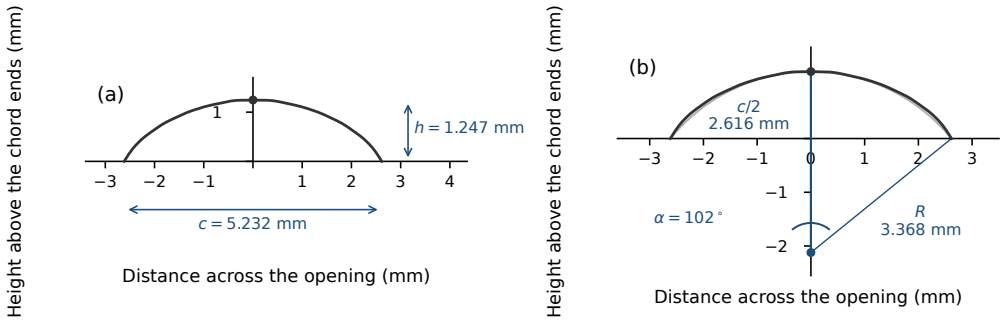


Figure 15: Side-view reduction of the 83.19 μm Chip 1 at 40 mbar, first session. **(a)** The guided trace, folded about the midpoint. The chord c is the opening and h is the apex above the ends. **(b)** The circle through those two ends and the apex. The center lies below the opening, so the radius R is longer than half the chord. The black curve is the measured trace.

II.7 EXTRA TENSION OF THE GOLD FILM

The bare tension is the reference load of an empty sheet. On the 90.53 μm coating gold is added to build GC260923_1, GC260923_2, and GC260923_3. All use the circular-segment reduction of Section II.6, at pressures from 12 to 40 mbar. Each value is the mean of the three cycles. The height is the apex of the folded trace above the chord ends.

A flatter dome has a larger radius, so the same pressure requires a larger tension. At 40 mbar the bare chip has $c = 4.83$ mm, $h = 0.960$ mm, and $R = 3.515$ mm, which gives

$$N = \frac{4000 \times 0.003515}{2} = 7.03 \ \mathrm{N\,m^{-1}}.$$

The three gold chips give 10.21, 9.62, and 9.37 N m^{-1} (Table 3). The extra tensions, gold minus bare at the same pressure, are 3.18, 2.59, and 2.34 N m^{-1}. GC260923_1 and GC260923_2 have chords of 4.86 and 4.75 mm, against 4.83 mm for the bare chip, so that extra is the film. GC260923_3 is the short chord, 4.31 mm, and its tension is still above the bare chip.

Table 3: Side-view reduction at 40 mbar on the 90.53 μm coating. The height is the apex of the folded trace. The extra tension is the gold-chip tension minus the bare-chip tension at the same pressure.

Chip	Chord (mm)	Height (mm)	R (mm)	N (N m^{-1})	Extra (N m^{-1})
GC260923_1	4.86	0.616	5.10	10.21	3.18
GC260923_2	4.75	0.627	4.81	9.62	2.59
GC260923_3	4.31	0.527	4.68	9.37	2.34

Placing the extra tension entirely in the 50 nm gold would give 64, 52, and 47 MPa, and that split holds only when the polymer under the gold still carries the bare tension of 7.03 N m^{-1}. The gold dome is the flatter one, so the polymer is less stretched and its share of the tension is smaller. The gold then carries more of the 9–10 N m^{-1} than the 2.3–3.2 N m^{-1} difference. The circle fixes only the total. If the polymer carried none of it, the same total in 50 nm of gold would be 204, 192, and 187 MPa. That is the ceiling.

The bare chip and the gold chips are reduced in the same way, so the difference is the change in the measured circle after the gold is added. From 12 to 40 mbar the gold tension stays above the bare tension, and the arch stays well below it. The size of that change is the result for the film. The referred center rise falls from 1.01 mm to 0.65–0.68 mm, and the extra tension at 40 mbar is a few N m^{-1} on a sheet that already carries 7.03 N m^{-1}. A continuous 50 nm gold film would take the tension, and the arch would fall much further than that. The transferred film stiffens the sheet and does so as a partial layer. The resistance measurement agrees with that reading on one chip: GC260923_2 opens the meter on the pressure peaks, the first time near 20 mbar (Section VI.1), while its side-view tension stays above the bare curve. An intact stack on this opening, read with the same formulas above 10 mbar, is the measurement that would give the oxide its share of the extra tension. Until that chip is measured, the bare tension is the reference load of the empty sheet, and it is not a strain in $BaTiO_3$.

III. GOLD TRANSFER DEVELOPMENT

The transferred fraction is read from the electrode design and from the gold still on the donor (Figure 16). The design is the whole electrode. The gold that remains on the donor is the part that did not leave. The two together are the full area, so the transferred fraction is $100\% \cdot (1 - A_{\mathrm{donor}}/A_{\mathrm{design}})$. The area is the projected area in the photograph. Wrinkles make the membrane side a little larger than the flat film. Across these early peels the transferred fraction runs from 56% to 87%. The transfers above 99% are the ones made after the immersion selected below.

The bottom gold is 50 nm, evaporated on silicon with no metal adhesion layer, then immersed in a solution of MPTMS in absolute ethanol (described in Section 2.1). Initial transfers were done with older gold-covered wafers. These wafers did not produce any usable membrane. This can be explained by contamination on the gold surface, blocking adsorption sites for the molecule. Longer immersion times could mitigate this issue [43]. To reduce experiment time the gold for the screen was therefore evaporated immediately before the immersion. The screen was run on glass, one specimen per condition. It ranks the images qualitatively. It does not measure an adhesion energy.

The chloroform set was dipped five times, for 10 s each time, in chloroform, and dried under a stream of nitrogen. Directly after drying the slides were submerged in the solution to minimize the binding of ambient sulfur to the gold [43]. The annealed set was heated in nitrogen to 300 °C at 5 °C min^{-1}, held for 1.5 h, and cooled at the same rate. The furnace had been flushed with nitrogen for 5 h before the ramp. Each surface was then immersed at 0.1 mM or 5 mM, for 30 min or 60 min. A separate slide with no MPTMS transferred no visible gold.

After the immersion, the slides were rinsed with ethanol and dried with nitrogen. Sylgard 184 at 10:1 was poured to a slab about 5 mm thick, cured at 80 °C for 120 min, and left for 12 h at 100 °C. The slab was peeled by hand. A piece of Scotch tape was pressed on the transferred gold for one minute and subsequently peeled off. Each condition was imaged before the tape, after the tape, and on the tape.

Every MPTMS-treated slide transferred a gold film. The differences are continuity before the tape test and how much gold the tape removed (Fig. 17, 18, 19). Untreated gold at 0.1 mM for 30 min was continuous before the test, showed no clear loss after it, and left only sparse to no residue on the tape. That condition was selected. Other conditions looked similarly favorable, including untreated gold at 5 mM for 60 min. The choice is practical to reduce fabrication time and costs. It is not a uniquely demonstrated optimum.

The chloroform series does not rise or fall smoothly with concentration or time. Annealed gold at 0.1 mM was already discontinuous before the tape. Annealed gold at 5 mM kept larger continuous regions. Those differences are left as the images show them.

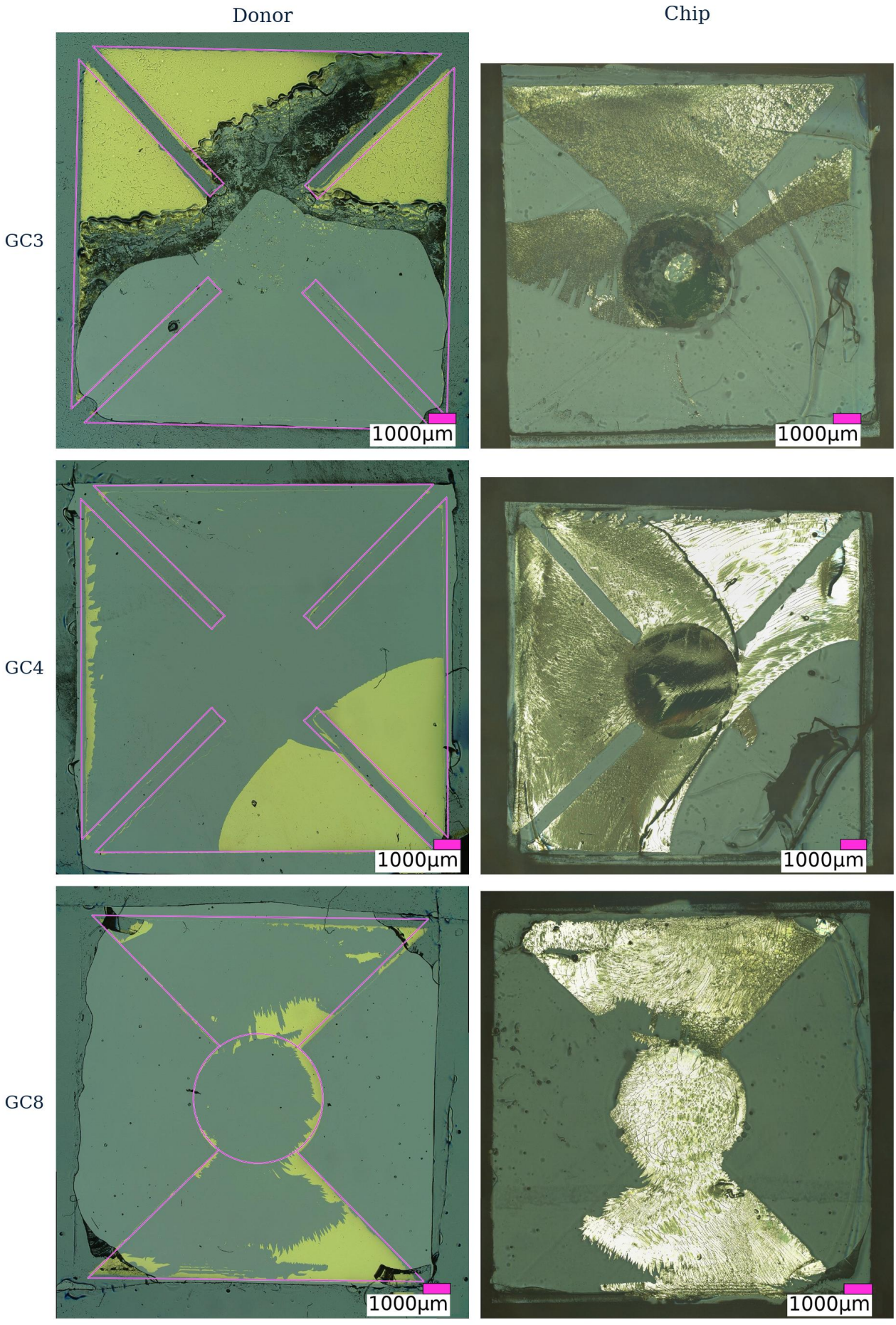


Figure 16: Electrode design on the donor, and the film that reached the chip. Rows are GC3, GC4, and GC8. The left column is the donor. The outline is the design area, and the gold inside it is the area that remained. The right column is the chip from the same peel. The scale bar is 1000 μm.

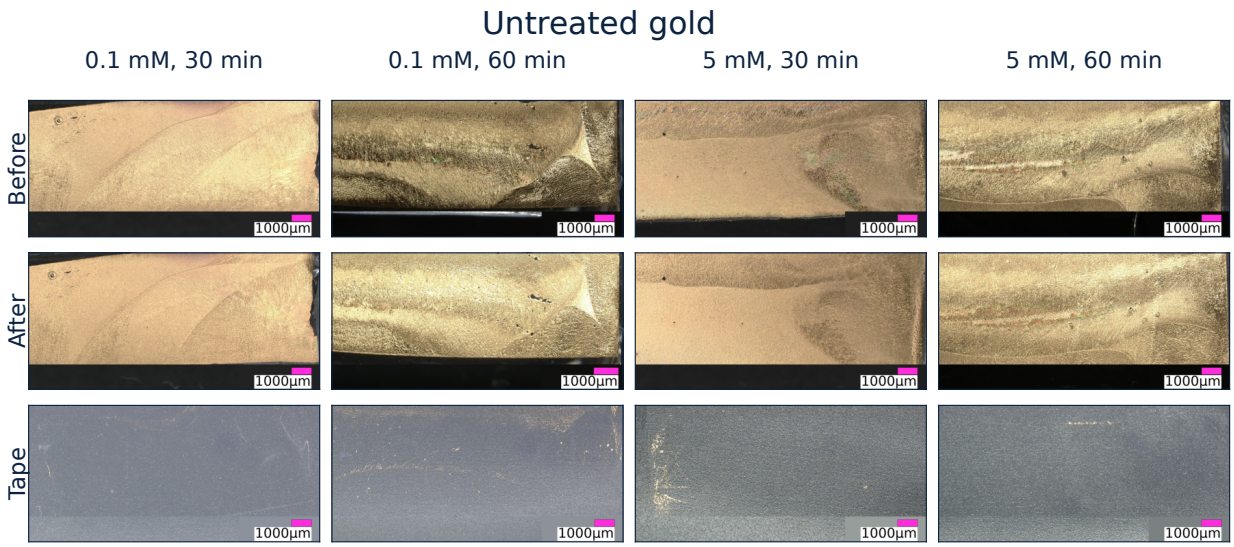


Figure 17: Untreated gold, immersed as evaporated. Columns are the four immersions. The upper row is the transferred film before tape test, the second row shows the same film after the tape test. The lower row is the tape. The mark is 1000 μm.

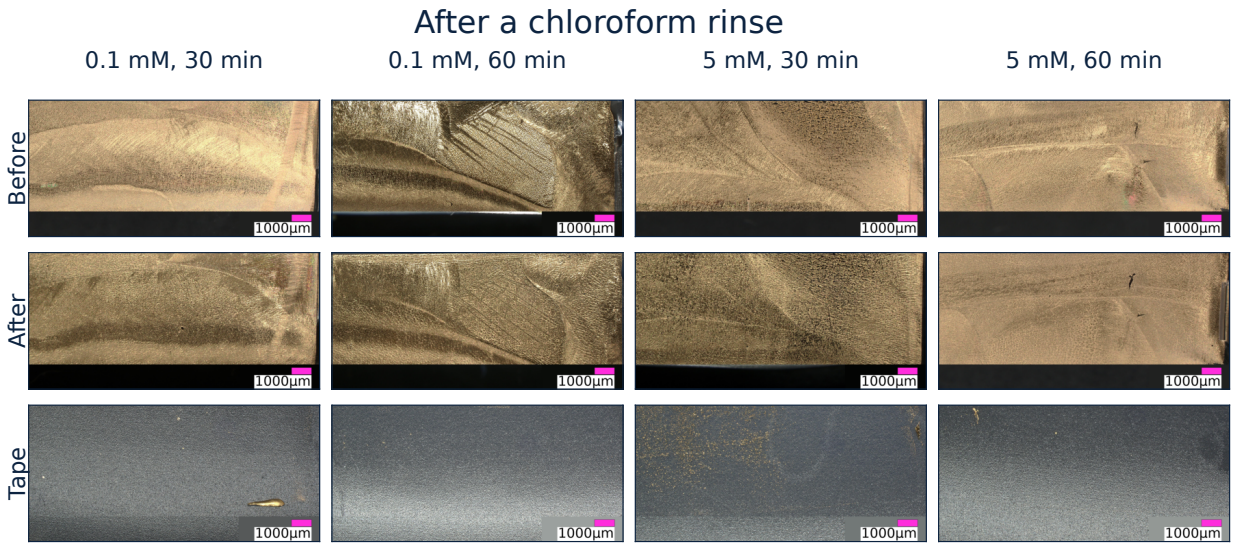


Figure 18: Gold rinsed in chloroform before the immersion. Columns and rows are as in Figure 17. The mark is 1000 μm.

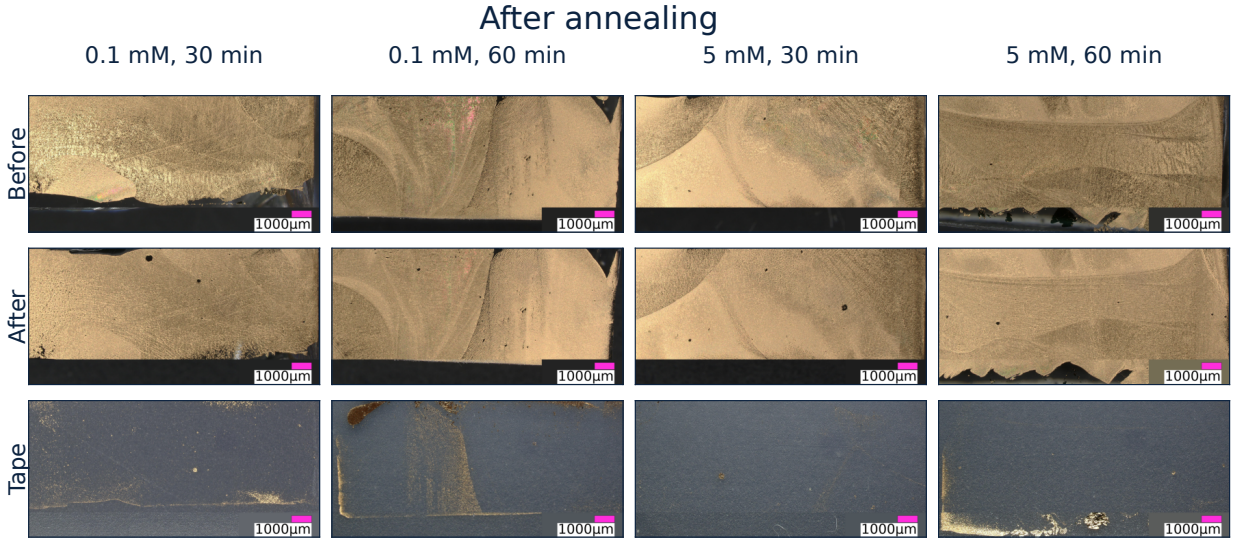


Figure 19: Gold annealed in nitrogen before the immersion. Columns and rows are as in Figure 17. The mark is 1000 μm.

IV. DEPOSITION RECORD

The growths were made one at a time when the substrate size was 5×5 mm. For bigger substrates, the substrate was diced into smaller pieces after deposition. This means that four samples can be deposited during one session. These samples will carry an additional index-number after the deposition name. A film was grown and inspected or tested, and the next setpoint was taken from that result. P260513 is the first film that was grown: $Sr_3Al_2O_6$ at 800 °C and $BaTiO_3$ at 750 °C, both at base pressure, 50000 and 4000 pulses. P260518 repeats those pulse counts with both layers at 840 °C. The rocking curve of $Sr_3Al_2O_6$ is narrower on P260518, 0.67° against about 0.16°, and 840 °C is the $Sr_3Al_2O_6$ temperature from then on. P260528 is the first thick $BaTiO_3$, 40000 pulses logged as 50 nm, grown at 840 °C in 200 mTorr. P260603_1 returns to the thin count, 4000 pulses, and grows both layers at 1 mTorr. The log records no $BaTiO_3$ peak on that row.

On 04.06.2026 the sacrificial entrance window was exchanged. The window sits in the laser beam path. Replacing it changes the energy that reaches the target, so one pulse no longer grows the thickness it grew on the coated window. Pulse counts from before that date are therefore not usable to determine the actual thickness of the deposition. P260609_2 is the calibration grown on the new window, 5000 pulses of $Sr_3Al_2O_6$ and a 700-pulse cap, and its reflectivity is the curve in Section IV.2. The rate read there is what sets the later $Sr_3Al_2O_6$ count: about 2000 pulses, where the earlier rows had used 50000 pulses for a logged thickness near 30 nm. On $BaTiO_3$ the same reset pairs about 7200 pulses with the logged 50 nm, and 14400 or 15000 pulses with about 100 nm. Before the exchange, 4000 pulses were the thin film, logged as about 5 nm on P260513 and P260518 and as "few" nanometers on P260603_1, and 40000 pulses were the 50 nm film. A 5 nm sheet and a 100 nm sheet are not the same mechanical object, so a crack network on an early release is not evidence about the support alone.

P260609_2 and P260610_1 both carry a note that the fluence should have been 2.1 J cm^{-2} instead of 2.4 J cm^{-2}. On P260610_1 the main layer was also stopped at 700 pulses, and the 50 nm cell is the thickness that was intended. Those two rows remain in the log and are left out of the recipe. P260610_1 is the first three-layer stack: $Sr_3Al_2O_6$, an oxygen-free cap, and a main layer at 750 °C in 200 mTorr. P260617_1 raises the main count to 15000 and was set out to analyze whether a thicker BTO layer reduces the number of cracks after release. P260622_1 brings the $Sr_3Al_2O_6$ count down to 1600 and tries the main layer at 100 mTorr. P260622_2 tries 1 mTorr again, and the log records no peak. P260624 returns the main layer to 200 mTorr and to 15000 pulses. P260701 is the first row with the cap at 850 pulses and the main layer at 7200, the 50 nm count used after that. From P260707 the usual coat is 5 nm of titanium, 50 nm of gold, and PMMA.

P260707 and P260708 leave the oxygen-free cap out. From P260716_1 the cap is back, and P260716_1 through P260720_1 repeat one growth: 2000 pulses of $Sr_3Al_2O_6$, 850 pulses of cap, and 7200 pulses of the main layer, at 840 °C then 750 °C, base pressure for the first two layers and 200 mTorr for the main layer. The fluence on those rows is 1.8 J cm^{-2} for $Sr_3Al_2O_6$ and 1.5 J cm^{-2} for $BaTiO_3$. From P260721 the main count is 14400. Temperature, oxygen, fluence, and the other two pulse counts stay the same through P260909_2. The September growths are written on 10×10 mm substrates. A second window exchange is written on 07.09.2026, after a compressed-air fault.

Deposition log

Op	Ref	Subs.	Size (mm)	Layers	Set temp. (°C)	Real temp.	Nominal PO2 (mTorr)	O2 MF (sccm)	Measured PO2 (mTorr)	Laser voltage (kV)	Laser power (mJ)	Fluence (J cm^{-2})	Pulses	Freq. (Hz)	FWHM (°)
MM	P260513	STO	5x5	1: SAO 2: BTO	1: 1,000 2: 938	1: 800 2: 750	1: BP 2: BP	x	x	1: 28.5 2: 21.5	1: 237 2: 154	1: 2.4 2: 1.5	1: 50,000 2: 4,000	1: 10 2: 4	1: 0.67 2: 0.97
NP	P260518	STO	5x5	1: SAO 2: BTO	1: 1,050 2: 1,050	1: 840 2: 840	1: BP 2: BP	x	x	1: 23.65 2: 19.56	1: 239 2: 149	1: 2.4 2: 1.5	1: 50,000 2: 4,000	1: 10 2: 4	1: 0.16 2: 0.59
NP	P260528	STO	5x5	1: SAO 2: BTO	1: 1,050 2: 1,050	1: 840 2: 840	1: BP 2: 200	1: x 2: 160	1: x. 2: 200	1: 25.5 2: 20.35	1: 240 2: 149.5	1: 2.4 2: 1.5	1: 35,000 2: 40,000	1: 10 2: 10	1: 0.29 2: 0.76
NP	P260603_1	STO	5x5	1: SAO 2: BTO	1: 1,050 2: 1,050	1: 840 2: 840	1: 1 2: 1	1: 6 2: 6	1.05	1: 22.9 2: 19.6	1: 239 2: 151	1: 2.4 2: 1.5	1: 50,000 2: 4,000	1: 10 2: 4	1: 0.12 2: none
4 June 2026 SACRIFICIAL WINDOW EXCHANGE															
NP	P260609_2	STO	5x5	1: SAO 2: BTO	1: 1,050 2: 1,050	1: 840 2: 840	1: BP 2: BP	1: x 2: x	1: x 2: x	1: 23.55 2: 19.8	1: 240 2: 150	1: 2.4 2: 1.5	1: 5,000 2: 700	1: 5 2: 4	
NP	P260610_1	STO	5x5	1: SAO 2: BTO 3: BTO	1: 1,050 2: 938 3: 938	1: 840 2: 750 3: 750	1: BP 2: BP 3: 200	1: x 2: x 3: 160	1: x 2: x 3: 194	1: 23.6 2: 19.85 3: 19.85	1: 241 2: 151 3: 151	1: 2.4 2: 1.5 3: 1.5	1: 5,000 2: 700 3: 700	1: 5 2: 4 3: 4	1: 0.34 2: none
NP	P260617_1	STO	5x5	1: SAO 2: BTO 3: BTO	1: 1,050 2: 938 3: 938	1: 840 2: 750 3: 750	1: BP 2: BP 3: 200	1: x 2: x 3: 160	1: x 2: x 3: 194	1: 23.6 2: 19.85 3: 19.85	1: 180 2: 151 3: 151	1: 1.8 2: 1.5 3: 1.5	1: 6,000 2: 1,500 3: 15,000	1: 5 2: 4 3: 4	
NP	P260622_1	STO	5x5	1: SAO 2: BTO 3: BTO	1: 1,050 2: 938 3: 938	1: 840 2: 750 3: 750	1: BP 2: BP 3: 100	1: x 2: x 3: 124	1: x 2: x 3: 101	19.80	150	1.5	1: 1,600 2: 1,400 3: 7,100	4	1: 1.10 2: none
NP	P260622_2	STO	5x5	1: SAO 2: BTO 3: BTO	1: 1,050 2: 938 3: 938	1: 840 2: 750 3: 750	1: 1 2: 1 3: 100	1: 6 2: 6 3: 124	1. 1.01 2: 1.01 3: 101	19.83	150	1.5	1: 2,250 2: 1,900 3: 7,100	4	1: none 2: none
NP	P260624	STO	5x5	1: SAO 2: BTO 3: BTO	1: 1,050 2: 938 3: 938	1: 840 2: 750 3: 750	1: BP 2: BP 3: 200	1: x 2: x 3: 160	1: x 2: x 3: 200	1: 20.95 2: 19.9 3: 19.9	1: 180 2: 150 3: 150	1: 1.8 2: 1.5 3: 1.5	1: 2,000 2: 1,400 3: 15,000	4	1: none 2: 1.06
NP	P260701	STO	5x5	1: SAO 2: BTO 3: BTO	1: 1,050 2: 938 3: 938	1: 840 2: 750 3: 750	1: BP 2: BP 3: 200	1: x 2: x 3: 160	1: x 2: x 3: 200	1: 21.4 2: 20.15 3: 20.15	1: 180 2: 150 3: 150	1: 1.8 2: 1.5 3: 1.5	1: 2,000 2: 850 3: 7,200	4	1: 0.25 2: 1.10
NP	P260707	STO	5x5	1: SAO 2: BTO	1: 1,050 2: 938	1: 840 2: 750	1: BP 2: 200	1: x 2: 160	1: x 2: 195	1: 21.75 2: 20.4	1: 180 2: 150	1: 1.8 2: 1.5	1: 2,000 2: 8,600	4	1: none 2: 1.00
NP	P260708	STO	5x5	1: SAO 2: BTO	1: 1,050 2: 938	1: 840 2: 750	1: 1 2: 200	1: 6 2: 160	1: 1 2: 200	1: 21.8 2: 20.45	1: 180 2: 150	1: 1.8 2: 1.5	1: 2,000 2: 8,600	4	1: none 2: none
NP	P260716_1	STO	5x5	1: SAO 2: BTO 3: BTO	1: 1,050 2: 938 3: 938	1: 840 2: 750 3: 750	1: BP 2: BP 3: 200	1: x 2: x 3: 160	1: x 2: x 3: 200	1: 22.5 2: 21 3: 21	1: 180 2: 151 3: 150	1: 1.8 2: 1.5 3: 1.5	1: 2,000 2: 850 3: 7,200	4	
NP	P260717_1	STO	5x5	1: SAO 2: BTO 3: BTO	1: 1,050 2: 938 3: 938	1: 840 2: 750 3: 750	1: BP 2: BP 3: 200	1: x 2: x 3: 160	1: x 2: x 3: 200	1: 22.65 2: 21.15 3: 21.1	1: 181 2: 151 3: 151	1: 1.8 2: 1.5 3: 1.5	1: 2,000 2: 850 3: 7,200	4	
NP	P260720_1	STO	5x5	1: SAO 2: BTO 3: BTO	1: 1,050 2: 938 3: 938	1: 840 2: 750 3: 750	1: BP 2: BP 3: 200	1: x 2: x 3: 160	1: x 2: x 3: 200	1: 23.1 2: 21.45 3: 21.4	1: 181 2: 152 3: 151	1: 1.8 2: 1.5 3: 1.5	1: 2,000 2: 850 3: 7,200	4	
NP	P260721	STO	5x5	1: SAO 2: BTO 3: BTO	1: 1,050 2: 938 3: 938	1: 840 2: 750 3: 750	1: BP 2: BP 3: 200	1: x 2: x 3: 160	1: x 2: x 3: 200	1: 23.12 2: 21.5 3: 21.48	1: 180 2: 152 3: 151	1: 1.8 2: 1.5 3: 1.5	1: 2,000 2: 850 3: 14,400	4	
NP	P260722	STO	5x5	1: SAO 2: BTO 3: BTO	1: 1,050 2: 938 3: 938	1: 840 2: 750 3: 750	1: BP 2: BP 3: 200	1: x 2: x 3: 160	1: x 2: x 3: 200	1: 23.25 2: 21.51 3: 21.51	1: 180 2: 150 3: 150	1: 1.8 2: 1.5 3: 1.5	1: 2,000 2: 850 3: 14,400	4	
NP	P260730	STO	5x5	1: SAO 2: BTO 3: BTO	1: 1,050 2: 938 3: 938	1: 840 2: 750 3: 750	1: BP 2: BP 3: 200	1: x 2: x 3: 160	1: x 2: x 3: 200	1: 24.74 2: 22.7 3: 22.55	1: 181 2: 152 3: 149	1: 1.8 2: 1.5 3: 1.5	1: 2,000 2: 850 3: 14,400	4	

One row per growth. Numbered lines are the layers, from the substrate upward. Shaded rows have a diffraction scan. FWHM is the rocking-curve width from that scan. Window-exchange rows are markers in the log, not growths.

Deposition log

Op	Ref	Subs.	Size (mm)	Layers	Set temp. (°C)	Real temp.	Nominal PO2 (mTorr)	O2 MF (sccm)	Measured PO2 (mTorr)	Laser voltage (kV)	Laser power (mJ)	Fluence (J cm^{-2})	Pulses	Freq. (Hz)	FWHM (°)
NP	P260827	STO	5x5	1: SAO 2: BTO 3: BTO	1: 1,050 2: 938 3: 938	1: 840 2: 750 3: 750	1: BP 2: BP 3: 200	1: x 2: x 3: 160	1: x 2: x 3: 200	1: 20.6 2: 21.92 3: 21.92	1: 182 2: 150 3: 150	1: 1.8 2: 1.5 3: 1.5	1: 2,000 2: 850 3: 14,400	4	
7 September 2026 SACRIFICIAL WINDOW EXCHANGE (because compressed air issue)															
NP	P260908_1	STO	10x10	1: SAO 2: BTO 3: BTO	1: 1,050 2: 938 3: 938	1: 840 2: 750 3: 750	1: BP 2: BP 3: 200	1: x 2: x 3: 160	1: x 2: x 3: 200	1: 23.1 2: 21.5 3: 21.45	1: 182 2: 152 3: 151	1: 1.8 2: 1.5 3: 1.5	1: 2,000 2: 850 3: 14,400	4	
NP	P260908_2	STO	10x10	1: SAO 2: BTO 3: BTO	1: 1,050 2: 938 3: 938	1: 840 2: 750 3: 750	1: BP 2: BP 3: 200	1: x 2: x 3: 160	1: x 2: x 3: 200	1: 23.1 2: 21.45 3: 21.4	1: 183 2: 152 3: 151	1: 1.8 2: 1.5 3: 1.5	1: 2,000 2: 850 3: 14,400	4	1: 0.17 2: 0.66
NP	P260909_1	STO	10x10	1: SAO 2: BTO 3: BTO	1: 1,050 2: 938 3: 938	1: 840 2: 750 3: 750	1: BP 2: BP 3: 200	1: x 2: x 3: 160	1: x 2: x 3: 200	1: 23 2: 21.36 3: 21.38	1: 183 2: 152 3: 151	1: 1.8 2: 1.5 3: 1.5	1: 2,000 2: 850 3: 14,400	4	
NP	P260909_2	STO	10x10	1: SAO 2: BTO 3: BTO	1: 1,050 2: 938 3: 938	1: 840 2: 750 3: 750	1: BP 2: BP 3: 200	1: x 2: x 3: 160	1: x 2: x 3: 200	1: 23.25 2: 21.51 3: 21.51	1: 180 2: 150 3: 150	1: 1.8 2: 1.5 3: 1.5	1: 2,000 2: 850 3: 14,400	4	

One row per growth. Numbered lines are the layers, from the substrate upward. Shaded rows have a diffraction scan. FWHM is the rocking-curve width from that scan. Window-exchange rows are markers in the log, not growths.

IV.1 DIFFRACTION SCANS

The scans use Cu Kα_1 radiation ($\lambda = 1.540598$ Å). On a symmetric coupled scan the scattering vector stays normal to the surface and its length changes, so the angle of a maximum is the spacing of the planes parallel to the surface [44]. The sharp maximum at 46.48° is the $SrTiO_3$ (002) reflection, 3.905 Å. A film maximum is read the same way, as an (002) spacing. An ω scan holds that spacing fixed and rotates the sample, so its width is the angular spread of the plane normals. Moram and Vickers list tilt and curvature as the contributions to that width. A short coherence length along the surface normal, as in a layer only a few nanometers thick, broadens the reflection on the coupled scan. The rocking width reported here is the full width at half the height above the intensity at the ends of the scan. The height of a maximum is not used as a measure of crystallinity.

In order to get clearer data, the scans are repeated multiple times. The coupled scans on the crystal are ten runs of 0.440 s at each point. P260624 has five complete runs at the same time per point. The $BaTiO_3$ rocking curves displayed in the appendix are five runs of 0.440 s, except P260624 and P260708, which have two. The $Sr_3Al_2O_6$ rocking curves are a single run. The time per point on that run is 0.660 s for P260513 and P260610_1, and 0.880 s for P260518, P260528, and P260603_1. P260622_1 uses 0.660 s and P260701 uses 0.880 s on the $Sr_3Al_2O_6$ run. P260701 has two complete $BaTiO_3$ runs; a third run in that file stops early and is left out. The plots are the mean of the complete runs, divided by the time per point. A file with more runs, or a longer dwell, is not drawn higher for that reason.

The intensity that remains is the sample. The $SrTiO_3$ (002) maximum is about 10^6 counts per second. The film maxima are tens to a few thousand counts per second. P260624 has no diffraction scan from before release. The only file is the one labeled PDMS. With the substrate gone, that curve sits at the film intensity, about 10^2 counts per second at its maximum, in the same range as the film maxima of the layers that are still on the crystal.

P260513 and P260518 are the temperature pair (Fig. 20). Both are from before the window exchange. Both layers are at the base pressure of the deposition chamber. The fluence is 2.4 for $Sr_3Al_2O_6$ then 1.5 J cm^{-2} for $BaTiO_3$, the pulse counts are 50000 then 4000, and the frequency is 10 then 4 Hz. The real temperature is 800 °C then 750 °C on P260513, and 840 °C for both layers on P260518. The $Sr_3Al_2O_6$ spacing stays at 3.968 Å and 3.962 Å. Its rocking curve narrows from 0.67° to 0.16°. The $BaTiO_3$ spacing moves from 4.082 Å to 4.067 Å, and its rocking curve from 0.97° to 0.59°. The $SrTiO_3$ rocking curves stay narrow on both chips, so the narrower film curves are the film. Substrate temperature is the setting that most often decides whether a pulsed-laser oxide orders as each pulse lands [45]. The rocking width is the spread of the plane normals, from tilt and from curvature [44]. Here the spacing barely moves and the widths drop, so the higher temperature narrowed that tilt distribution while the oxygen, which was base pressure on both chips, left the lattice expansion in place. Both $BaTiO_3$ layers are the thin film logged near 5 nm. On the coupled scan both remain a low, broad maximum, which is the broadening expected when the coherence length along the surface normal is only a few nanometers [44]. 840 °C is the $Sr_3Al_2O_6$ temperature kept after this pair. Epitaxial $Sr_3Al_2O_6$ for a freestanding membrane is grown near 10^{-6} Torr [16], the same pressure regime as the base pressure that keeps the $Sr_3Al_2O_6$ reflection in Figure 20.

Figure 21 is the oxygen series at 840 °C, still before the window exchange. P260518 and P260603_1 share the pulse counts, the fluence, and the frequency of the temperature pair. P260518 grows both layers at base pressure. P260603_1 grows both layers at 1 mTorr. On that pair the $BaTiO_3$ maximum present at base pressure is absent at 1 mTorr. The $Sr_3Al_2O_6$ maximum remains, moving from 3.962 Å and 0.16° to 3.978 Å and 0.12°. The 0.12° curve has a shoulder on the low-angle side, so that width is the narrow part of the curve. Laser-ablated $BaTiO_3$ on $SrTiO_3$ grows with a larger out-of-plane spacing when the oxygen pressure is lower [46]. The expansion is discussed as oxygen-vacancy defects [47] and, across 1–200 mTorr, as a change in the cation ratio as well [48]. The thin base-pressure films sit at 4.082 Å and 4.067 Å. A nominal 1 mTorr is neither the near-10^{-6} Torr growth used for epitaxial $Sr_3Al_2O_6$ [16] nor the higher oxygen pressure at which the $BaTiO_3$ reflection in Figure 21 becomes distinct. P260528 is on the same figure as the thick $BaTiO_3$ film: 40000 pulses, logged as 50 nm, in 200 mTorr, with the $Sr_3Al_2O_6$ count at 35000 and the $BaTiO_3$ frequency at 10 Hz. The oxygen and the thickness change together on that row. It is the first of the three with a distinct $BaTiO_3$ maximum, at 4.039 Å, and a rocking width of 0.76°. Its $Sr_3Al_2O_6$ rocking curve is 0.29° wide, at 3.979 Å. The smaller spacing follows the higher oxygen pressure [46]. The maximum is also easier to see because a 50 nm layer has a longer coherence length than the film logged near 5 nm [44].

The comparisons below are the growths from after the window exchange on 4 June 2026. A pulse count from before that date is a different thickness, as Section IV records.

P260610_1 is shown on its own (Fig. 22). It is the first three-layer stack, and the main layer was stopped at 700 pulses. The film maximum is $Sr_3Al_2O_6$, at 3.965 Å, with a rocking width of 0.34°. There is no $BaTiO_3$ maximum. That is the pattern of a $BaTiO_3$ layer that was not grown to the intended thickness, and of the underlying layer grown in the absence of oxygen. The substrate rocking curve is the narrow peak of the crystal.

P260622_1 and P260622_2 share the main $BaTiO_3$ layer: 7100 pulses at 100 mTorr and 750 °C, one fluence of 1.5 J cm^{-2} for the run, and 4 Hz (Fig. 23). $Sr_3Al_2O_6$ is at 840 °C. Both rows note a 30 min pre-anneal of the $SrTiO_3$ at the $Sr_3Al_2O_6$ temperature in 200 mTorr. On P260622_1 the first two layers are at base pressure, 1600 and 1400 pulses. On P260622_2 those layers are at 1 mTorr, 2250 and 1900 pulses. P260622_1 has one broad maximum. The rocking curve was taken at 45.36°, a spacing of 3.995 Å. The log entered 3.9977 Å and 1.1° and marked the reflection as uncertain between $Sr_3Al_2O_6$ and $BaTiO_3$. The rocking curve is about 1.1° wide. It is still above the background at the low-angle

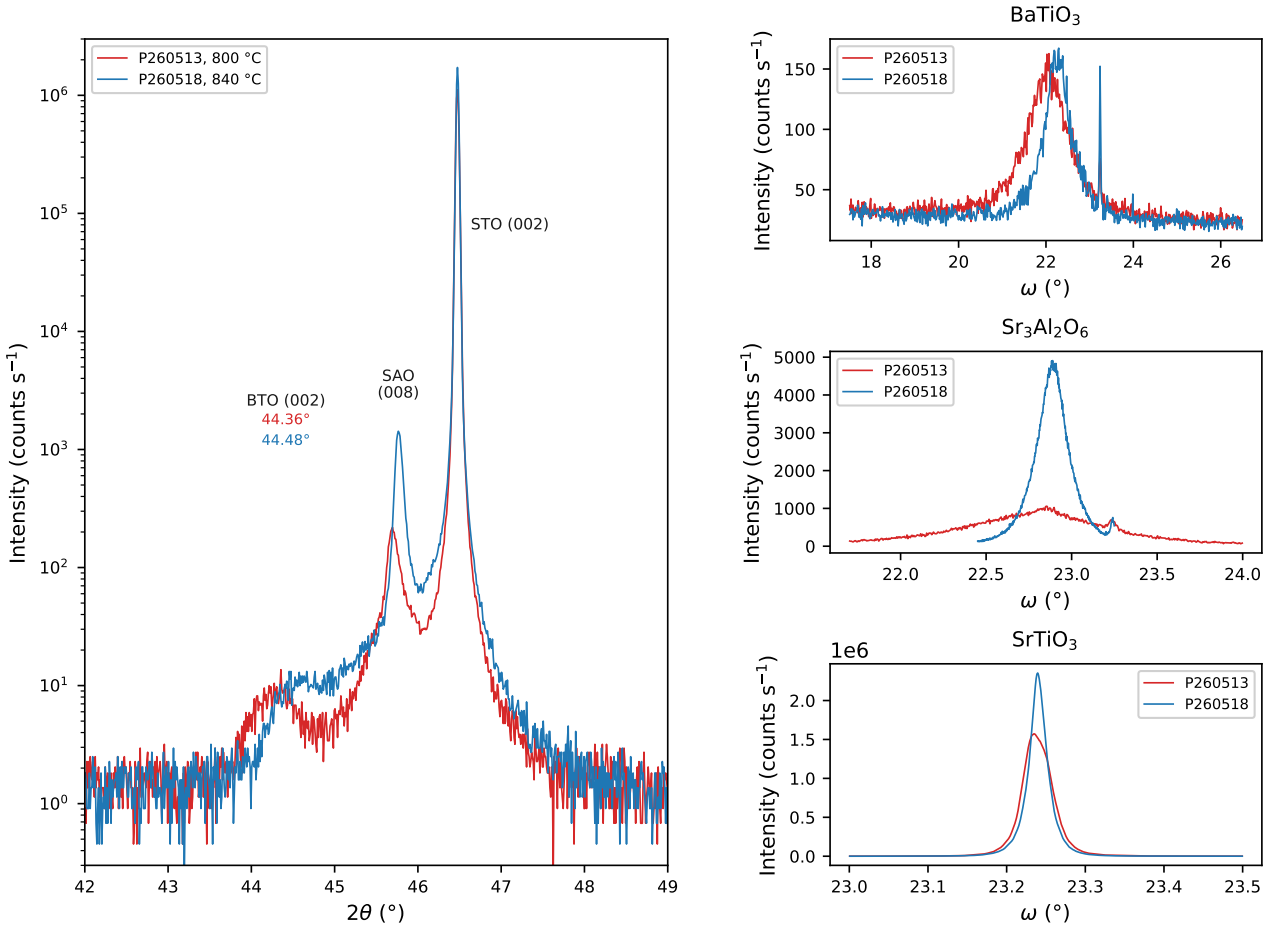


Figure 20: P260513 and P260518, the same pulse counts at two temperatures. Each curve is the mean of the runs named in the legend, in counts per second. Left: coupled scans. Right: rocking curves of $BaTiO_3$, $Sr_3Al_2O_6$, and the $SrTiO_3$ substrate.

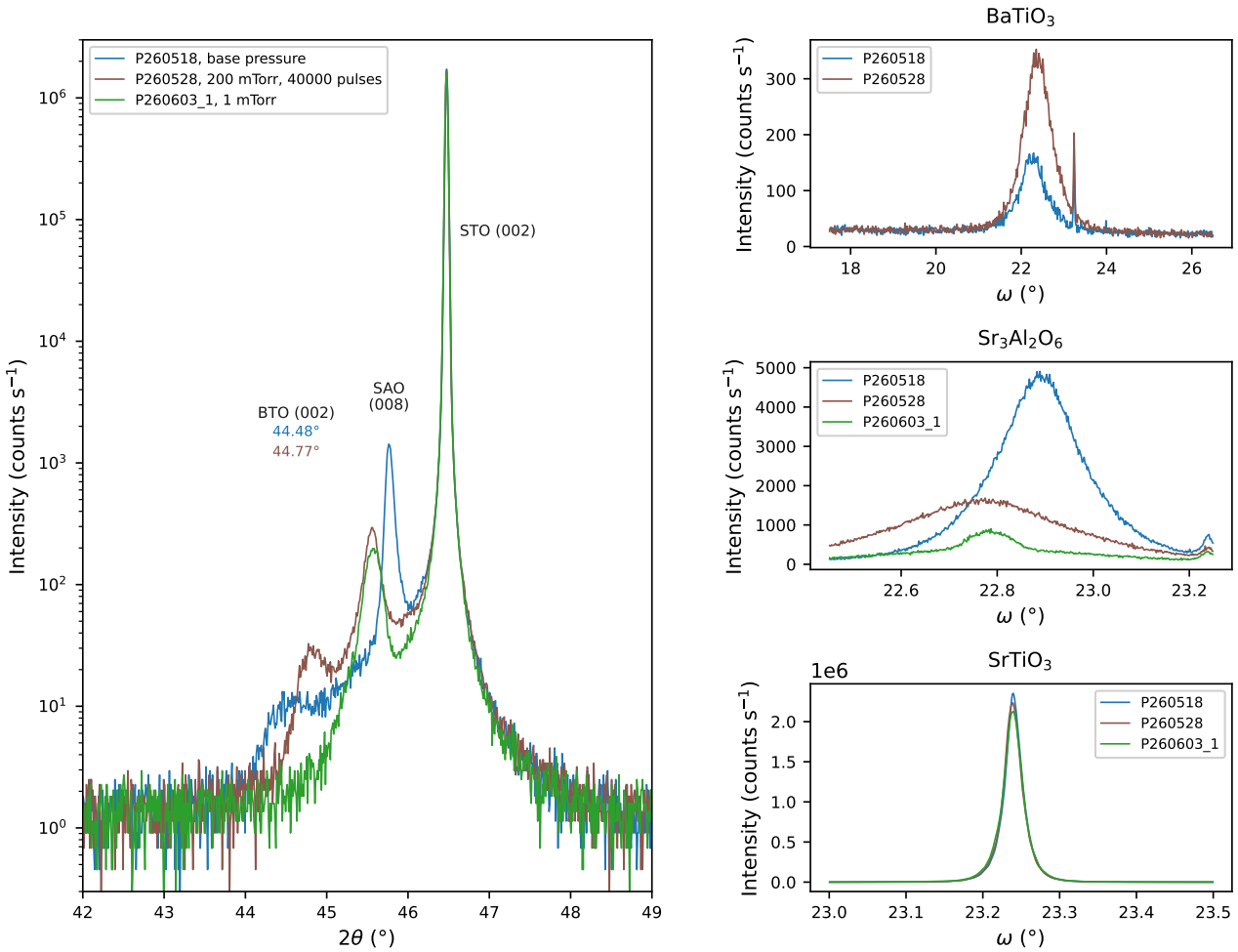


Figure 21: Coupled scans and rocking curves at 840 °C. P260603_1 has no $BaTiO_3$ rocking curve because that maximum is absent. The $Sr_3Al_2O_6$ rocking curves are the single run taken at 0.880 s per point. The substrate rocking curves are included for all three films.

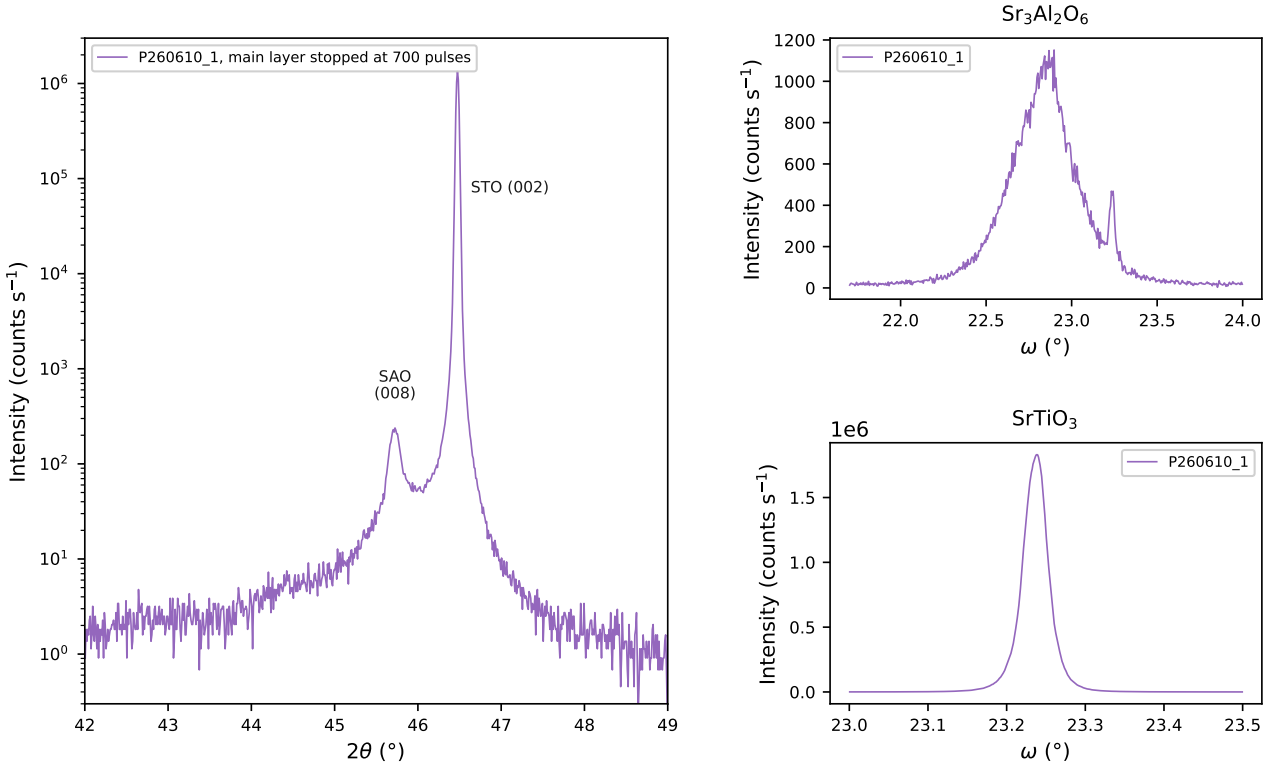


Figure 22: P260610_1. Left: the coupled scan. Right: the $Sr_3Al_2O_6$ rocking curve and the $SrTiO_3$ rocking curve.

end of the scan, and a narrow spike sits on the high-angle side. The width given here is the broad peak, not that spike. P260622_2 shows the substrate and no film maximum clear of its tail, and the folder has no film rocking curve. The substrate reflection is present on both chips. The same loss of the film maximum at 1 mTorr is the result on Fig. 21. The lower fluence of the laser at P260622_1 could explain the absence of a clear $Sr_3Al_2O_6$/$BaTiO_3$ peak. Growing the first layers at that pressure takes $Sr_3Al_2O_6$ out of the near-10^{-6} Torr condition in which the sacrificial layer is epitaxial [16], and the $BaTiO_3$ that follows has no (002) maximum to rock on.

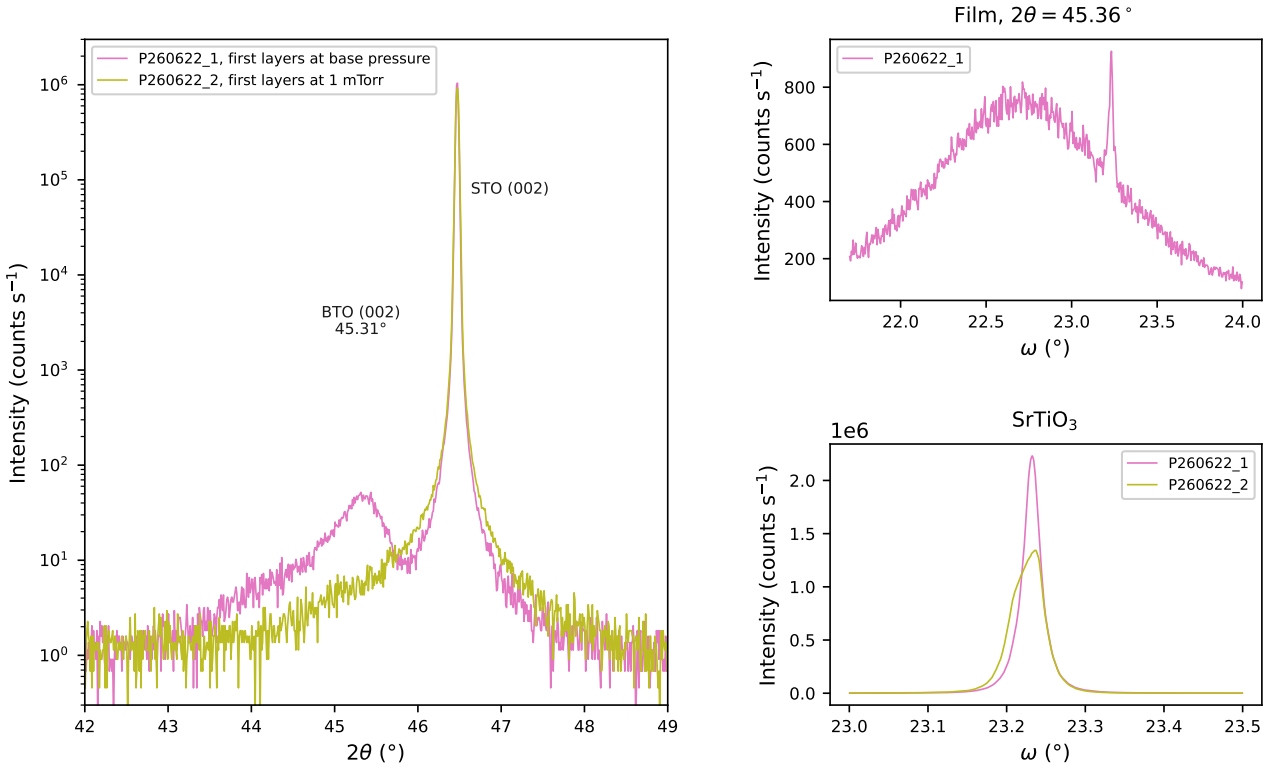


Figure 23: P260622_1 and P260622_2. Left: coupled scans. Upper right: the film rocking curve of P260622_1, taken at 45.36°. P260622_2 has no film rocking file. Lower right: the $SrTiO_3$ rocking curves.

P260701 is the first scanned growth after the window exchange with a $BaTiO_3$ maximum and a $Sr_3Al_2O_6$ maximum on separate rocking curves (Fig. 24). The temperatures are 840 then 750 °C, the fluence is 1.8 then 1.5 J cm^{-2}, and the pulse counts are 2000, 850, and 7200, with the main $BaTiO_3$ layer in 200 mTorr. Set next to P260622_1, the main-layer oxygen is 200 mTorr against 100 mTorr, and the cap count, the $Sr_3Al_2O_6$ count, and the fluence entry also change. The $BaTiO_3$ rocking curve is centered at 45.197°, a spacing of 4.009 Å, and its width is 1.10°. The $Sr_3Al_2O_6$ rocking curve is centered at 45.905°, a spacing of 3.951 Å. The broad part of that curve is 0.25° wide.

The main $BaTiO_3$ in the locked recipe is grown in two steps based on sample P260701. A thin first layer, about 850 pulses, is deposited at base pressure, and the thick layer is then deposited in 200 mTorr. A thin first layer is used in oxide pulsed-laser growth to set the nucleation, after which the main layer is grown at the condition wanted for the rest of the film [49]. In that work the first layer is grown colder, so the mismatch relaxes in a few nanometers and the main layer crystallizes on top of it. Here the split is the oxygen pressure. The first $BaTiO_3$ is grown at base pressure, where the thin films in Figure 20 still order, and the thick layer is grown in oxygen, which is the condition that brings the out-of-plane spacing down [46].

P260707 and P260708 leave that first layer out and are otherwise the closest pair after the window exchange (Fig. 25). Both use 840 then 750 °C, a fluence of 1.8 then 1.5 J cm^{-2}, 2000 then 8600 pulses, 4 Hz, and $BaTiO_3$ at 200 mTorr. The change is $Sr_3Al_2O_6$ at base pressure on P260707 and at 1 mTorr on P260708. P260707 has a $BaTiO_3$ maximum at 4.024 Å and a rocking width of 1.00°, and no clear $Sr_3Al_2O_6$ maximum. The small shoulder next to the substrate peak could be a hint of the underlying $Sr_3Al_2O_6$. The substrate peak is still present on the coupled scan. Omitting the cap therefore leaves the $BaTiO_3$ reflection in place once $Sr_3Al_2O_6$ has been grown at base pressure. The same folder contains an ω scan named as a substrate scan. The detector on that scan was at 45.02°, the $BaTiO_3$ angle, over the substrate ω window, and the curve contains a narrow spike. The $BaTiO_3$ width in the table is the separate rocking curve. P260708 has no film maximum clear of the substrate tail. The ω scan taken with the detector at 49.0° stays near the background. As seen on Figure 21 and Figure 23, 1 mTorr on the first layer is the setting that removes the film maximum.

Where a $BaTiO_3$ maximum is present, the thin base-pressure films sit at 4.082 Å and 4.067 Å. The thicker films grown in oxygen sit at 4.039 Å (P260528), 4.009 Å (P260701), and 4.024 Å (P260707). The narrowest $BaTiO_3$ rocking curve is the 840 °C base-pressure film, 0.59°. The thicker oxygenated films fall between 0.64° and 1.10°. The films in that

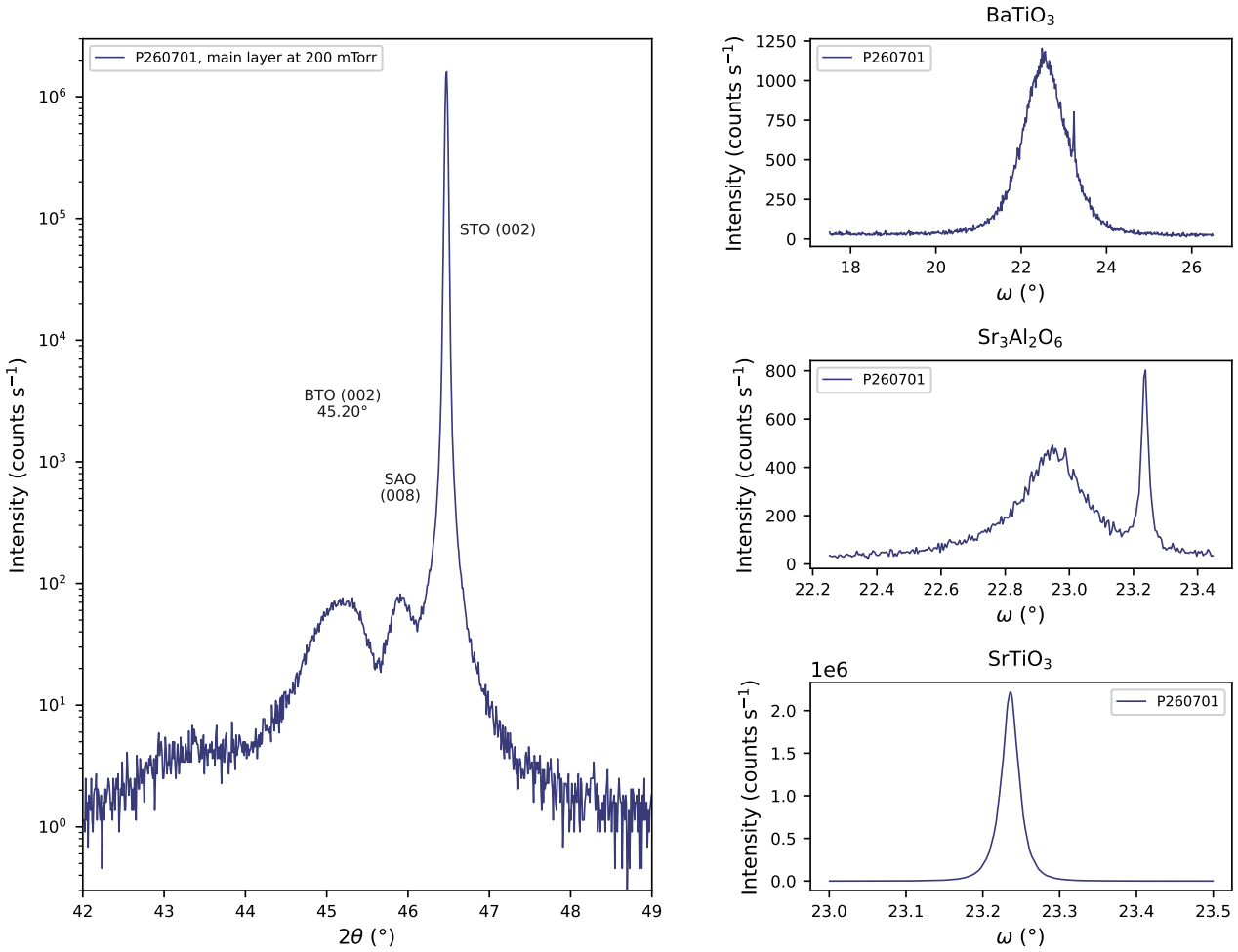


Figure 24: P260701. Left: the coupled scan. Right, from the top: the $BaTiO_3$ rocking curve, the $Sr_3Al_2O_6$ rocking curve, and the $SrTiO_3$ rocking curve.

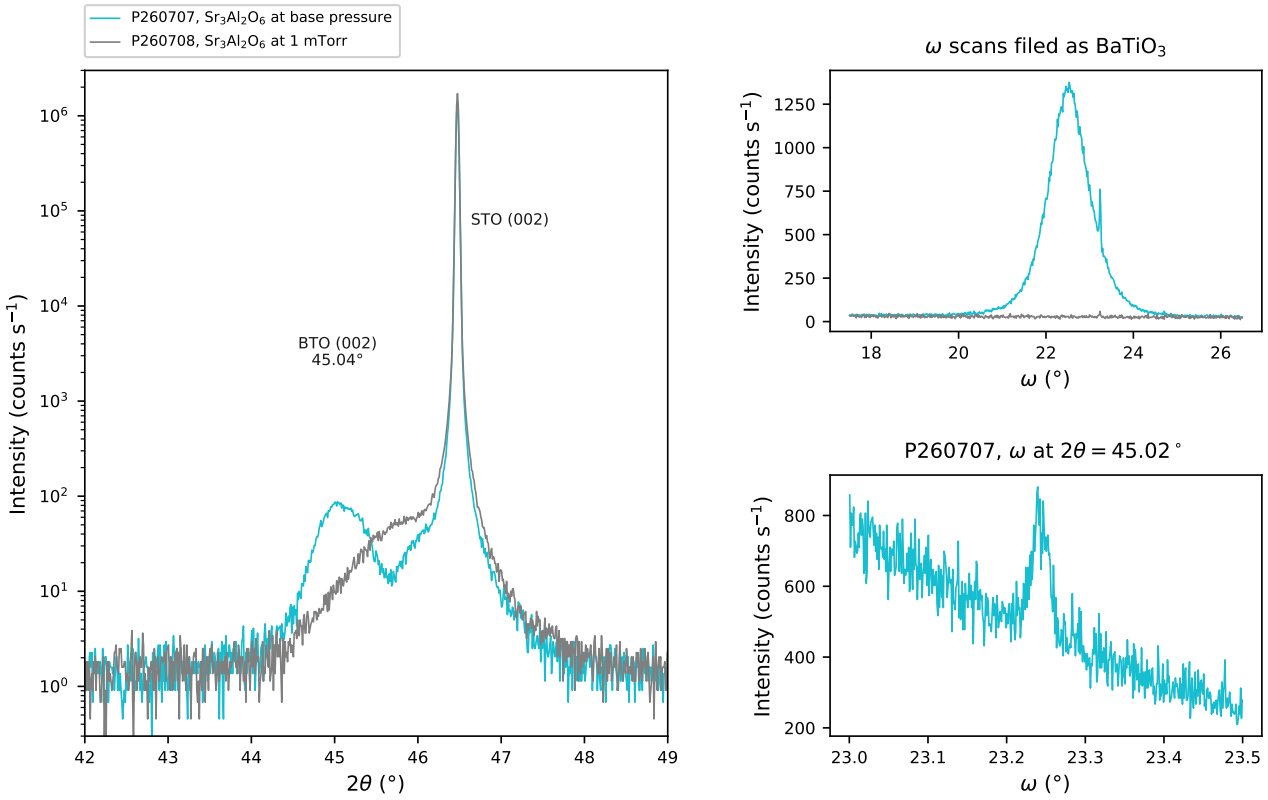


Figure 25: P260707 and P260708, the cap omitted. Left: coupled scans. Upper right: the ω scans filed as $BaTiO_3$. The P260707 scan is the rocking curve at 45.02°. The P260708 scan was taken at 49.0°. Lower right: the P260707 ω scan named as a substrate scan and taken at the $BaTiO_3$ angle.

comparison also differ in pulse count, and the growths from before 4 June 2026 were made at a different rate.

P260624 is the released film (Fig. 26). The only scan is the one labeled PDMS, so there is no on-crystal scan of the same growth to set beside it. The substrate peak is gone, and one maximum remains, at 3.997 Å, with a rocking width of 1.06°. That spacing sits with the thicker oxygenated films. Curvature broadens an ω scan [44]. A released sheet can add that curvature, so the width is read together with the fact that the out-of-plane reflection is still there.

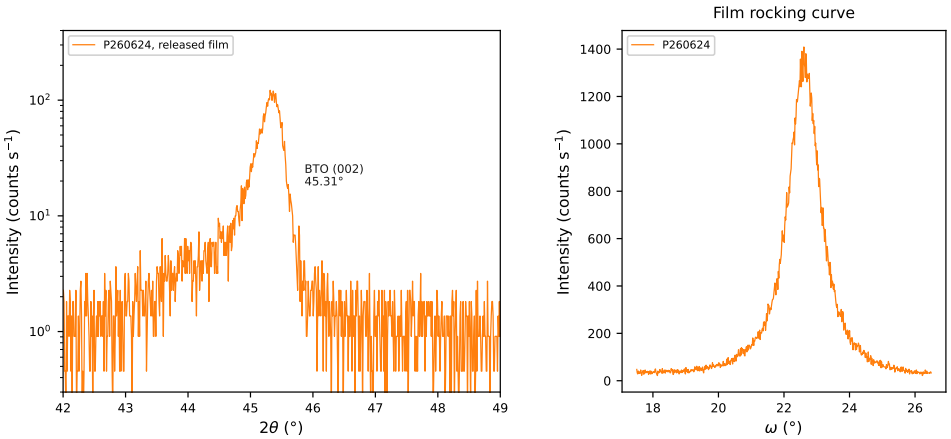


Figure 26: P260624 after release onto PDMS. Left: the coupled scan, on the scale of the film intensity. The substrate reflection is absent. Right: the rocking curve of the remaining maximum.

The reciprocal-space maps are a cut around the $SrTiO_3$ (103) reflection (Fig. 27). For $a = 3.905$ Å that is 0.256 and 0.768 Å^{-1}. A film spot at lower Q_z, with Q_x still near the substrate, is a larger out-of-plane spacing at nearly the same in-plane spacing. Every map here is 507 frames at 0.189 s per frame, so the measurement is the same one. The color scale is saturated at 40 counts. The substrate spot itself is several thousand counts. P260518 is the map with a second maximum, near $Q_z = 0.757$ Å^{-1}, which matches the $Sr_3Al_2O_6$ spacing already read from its coupled scan. On those maps, as on P260513, P260528, and P260603_1, the film intensity in this quick scan stays at a few counts, and the spacing used in the table remains the one from the coupled scan.

The same cut for one growth is in Fig. 28. These are the three pieces in Section 3.2. P260908_2_3 is still on the

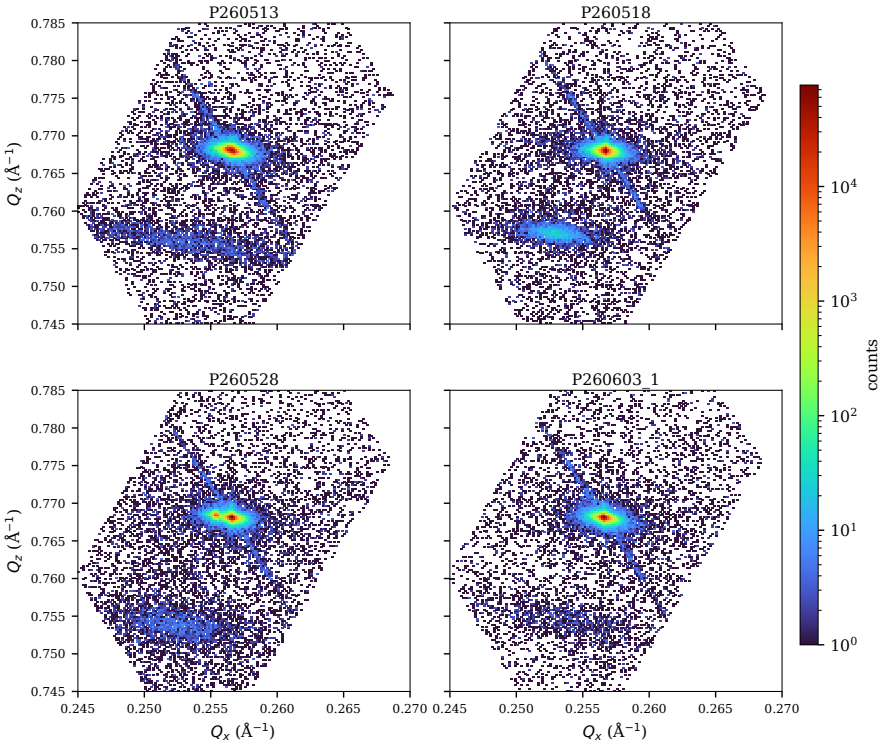


Figure 27: Reciprocal-space maps around the $SrTiO_3$ (103) reflection. Each map is 507 frames at 0.189 s per frame, including P260622_1 and P260701. The color scale stops at 40 counts so a weak film spot can be seen. The substrate spot is far above that scale. P260518 is the map with a second maximum.

substrate. P260908_2_4 was released and still carries PMMA. P260908_2_1 was released and the PMMA was removed. Each map joins three detector windows, 4269 frames at 0.189 s. The sharp spot near $Q_z = 0.77$ Å^{-1} is the $SrTiO_3$ reflection. It is present only while the stack is on the substrate. The broader maximum below it is the film. That maximum remains after release, both on the piece that still carries PMMA and on the piece from which the PMMA was removed.

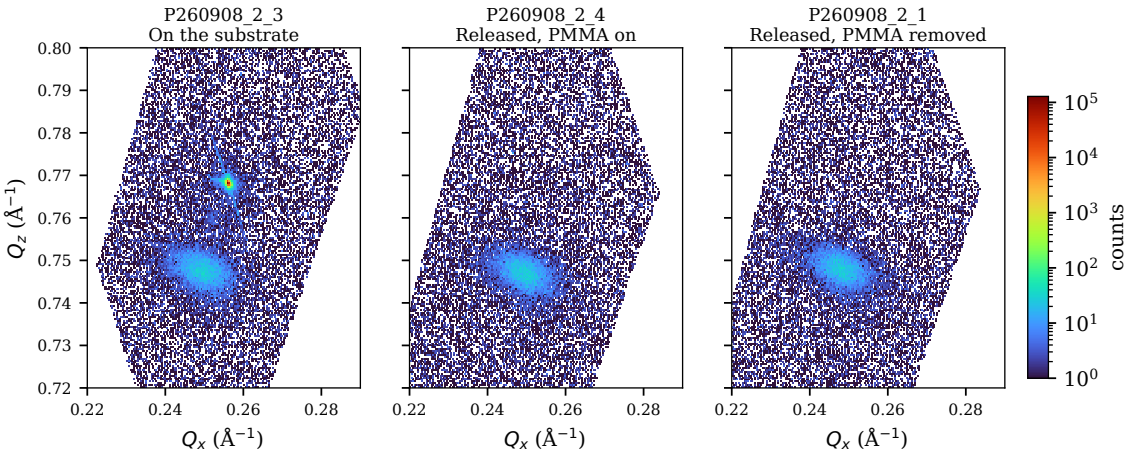


Figure 28: Reciprocal-space maps of three pieces from one growth, around the $SrTiO_3$ (103) reflection. Left: P260908_2_3, still on the substrate. The sharp spot is $SrTiO_3$. The broader maximum below it is the film. Center: P260908_2_4, released, PMMA still on. Right: P260908_2_1, released, PMMA removed. The $SrTiO_3$ spot is absent on both released pieces. The film maximum remains.

IV.2 REFLECTIVITY CURVE USED FOR THE PULSE COUNT

The thickness was taken from the spacing of the Kiessig fringes on a specular reflectivity curve. For one film, a plot of $\sin^2\theta$ against the square of the fringe order is linear. Moram and Vickers give the slope of that line as $\lambda^2/(2t)^2$, so the thickness is $\lambda/(2\sqrt{\text{slope}})$ [44]. That measurement was made on a thick layer of $Sr_3Al_2O_6$ with a very small capping layer of $BaTiO_3$. The thickness divided by the number of pulses used for that layer is the growth rate of that material. The pulse count of a later bilayer is the thickness wanted for each layer, divided by the growth rate of that layer.

The curve with a countable series is P260609_2, grown after the laser window was exchanged (Fig. 29). It is one layer of $Sr_3Al_2O_6$, 5000 pulses, with a thin $BaTiO_3$ cap, so the period is those two layers together. Twenty-six maxima, read with Cu Kα_1 radiation ($\lambda = 1.540598$ Å), give 110.4 ± 0.2 nm. About 105 nm of $Sr_3Al_2O_6$ after 5000 pulses is 0.021 nm per pulse. A target near 40 nm is then about 1900 pulses. The remaining 5 nm of $BaTiO_3$ was deposited with 700 pulses, the determined growth rate therefore is 7.14 pm per pulse. A targeted 100 nm is about 14400 pulses. The methods use that count and a nominal $Sr_3Al_2O_6$ thickness of about 40 nm. It has to be mentioned that the fluence during the deposition where the thickness was determined differ from the final recipe. Therefore the thicknesses could differ from the expected values. An additional thickness measurement via atomic force microscopy or cross sectional scanning electron microscopy would deliver precise values. Since the quality of the film is more critical for the fabrication than small deviation in the thickness, the nominal values are sufficient.

A reflectivity curve of a $BaTiO_3$ layer alone, with a period that can be counted in the same way, was not successfully measured. The $BaTiO_3$ pulse counts in the bilayer therefore remain the nominal counts in the methods. The other four reflectivity files fall into the background before a regular series of maxima can be marked (Fig. 30). They are not given a thickness.

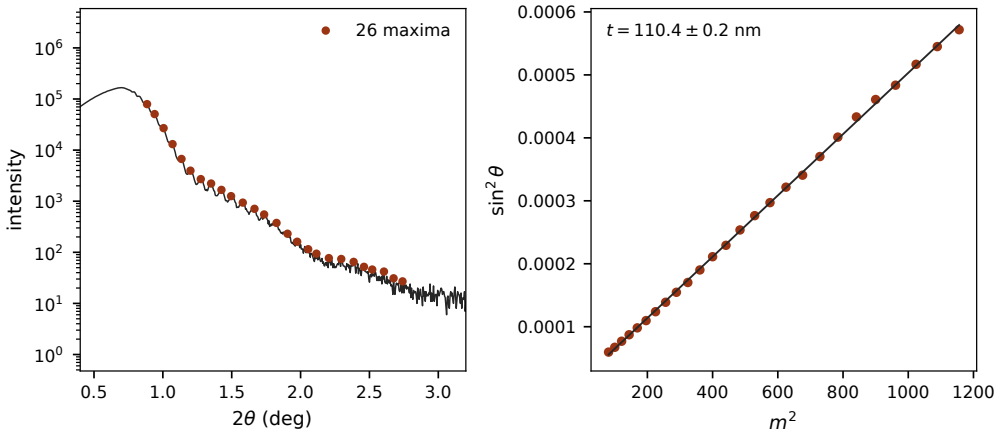


Figure 29: Specular reflectivity of P260609_2. Left: the curve and the 26 fringe maxima used for the fit. Right: $\sin^2\theta$ against m^2. The slope is the total thickness, 110.4 ± 0.2 nm.

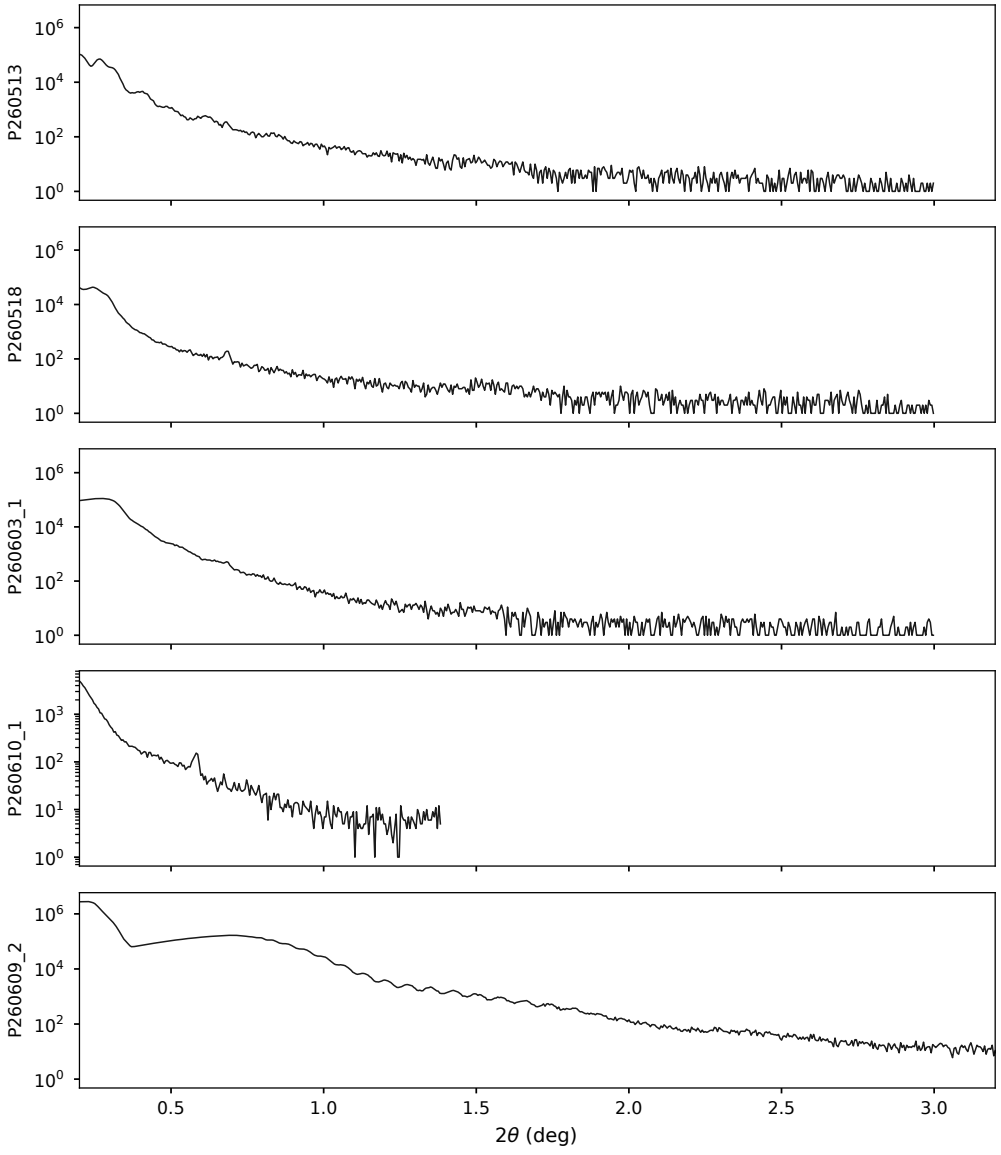


Figure 30: Every reflectivity measurement. Only P260609_2 has a regular series of maxima. The other four are not given a thickness.

V. RELEASE OF THE THIN FILM STACK

The oxide cannot be grown directly on the membrane, so the stack was released from $SrTiO_3$ by dissolving $Sr_3Al_2O_6$ in water. The first films were transferred directly onto PDMS, to see how this release would go. Those releases had no extra layers on the $BaTiO_3$, and each one was tried after the diffraction measurement of that sample. The quality of the release depends inter alia on the crystallinity of the $Sr_3Al_2O_6$. A poorer grade can include other compositions that do not dissolve in water, so parts of the film do not release. That leaves holes, or an uneven relaxation of the strain, and therefore cracks.

The first change tried on that direct release onto PDMS was a thicker $BaTiO_3$ (Fig. 31). P260518_3 has an estimated thickness of 5 nm and P260622_1_1 is logged at 50 nm, while P260617_1 is logged at 100 nm. The 100 nm sheet has fewer cracks than those two, but more bubbles. Bubbles were absent from the earlier releases.

The release was then tried on different supports: PDMS, Kapton, and temperature-release tape (Fig. 32). The three pieces are from one growth, P260617, with the main $BaTiO_3$ layer logged at 100 nm.

The difference between a good $Sr_3Al_2O_6$ layer and a poorer one is shown in Fig. 33. Both samples had PMMA spin-coated on them for support during release, and neither has gold. The film from the higher-quality $Sr_3Al_2O_6$ has only a small reduction in cracks, but noticeably fewer wrinkles. P260624 is the more complete sheet.

Figure 34 compares the added layers after the pulsed-laser deposition. P260624 has PMMA and no gold. P260908_2_2 has gold and no PMMA. P2600909_1_4 has both. The sheet that keeps the gold and the PMMA is nearly free of cracks, with a few small wrinkles. The dark spots are residual $Sr_3Al_2O_6$. P260624 and P260909_1_4 are at 40×. P260908_2_2 was saved at 50×.

Depositing the gold on the $BaTiO_3$ and then spin coating PMMA is the release that reached a continuous prototype. The films were transferred to the bottom electrode as described in Section 2.3. Six prototypes kept the PMMA. Three of them are shown in Fig. 35.

The PMMA covers the top gold, electrically insulating it. Since the PMMA removal once the thin films are transferred to the PDMS chip produced failures, the PMMA was removed from the top layer while the $BaTiO_3$ was still on the donor wafer in order to try electrical characterization. Then the same release was run in order to contact that electrode. Eight films were released that way. Together with the six that kept the PMMA, that is fourteen prototypes. Two of the eight are shown in Fig. 36.

After those transfers, the PMMA was removed in acetone and the stack was connected electrically. That step produced the failures shown below.

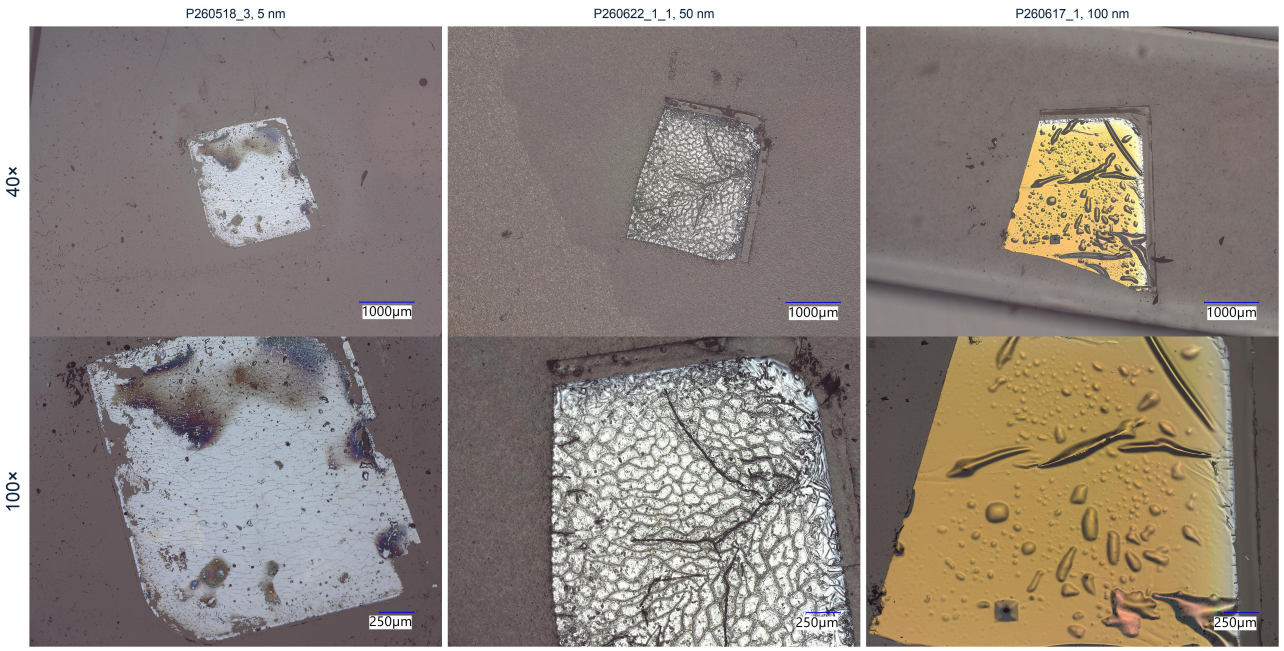


Figure 31: Direct release onto PDMS, with no extra layer on the $BaTiO_3$. Left to right: P260518_3, logged at 5 nm; P260622_1_1, logged at 50 nm; P260617_1, logged at 100 nm. In each column the 40× frame is directly above the 100× frame of the same piece. The 40× scale bar is 1000 μm and the 100× scale bar is 250 μm.

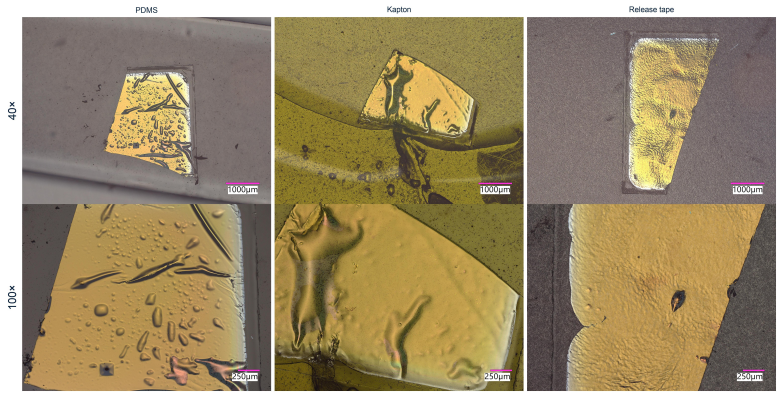


Figure 32: P260617 released onto three supports, with no extra layer on the $BaTiO_3$. Left to right: P260617_1 on PDMS, P260617_2 on Kapton, and P260617_3 on temperature-release tape. In each column the 40× frame is directly above the 100× frame. Scale bars are 1000 μm and 250 μm.

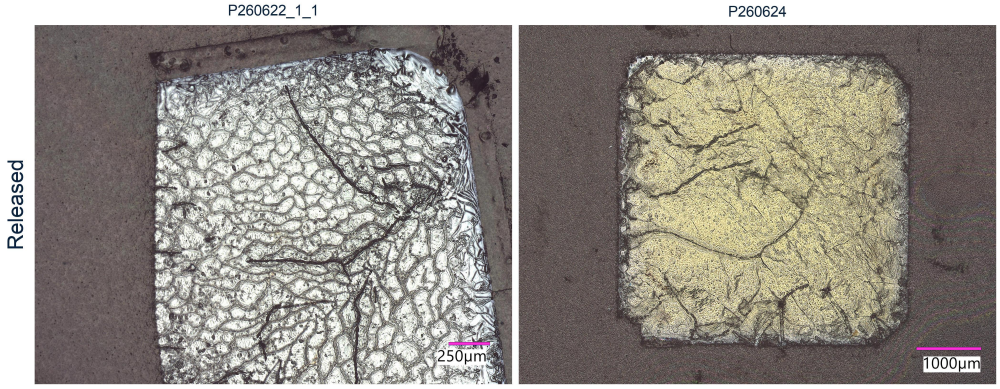


Figure 33: Release with PMMA and without gold, both at 40×. Left: P260622_1_1, the poorer $Sr_3Al_2O_6$. Right: P260624, the improved $Sr_3Al_2O_6$. The scale bar is 1000 μm.



Figure 34: Improved $Sr_3Al_2O_6$, released onto tape. Left: P260624, PMMA and no gold, 40×. Center: P260908_2_2, gold and no PMMA, 50×. Right: P260707, gold and PMMA, 40×. The 40× scale bar is 1000 μm and the 50× scale bar is 500 μm.

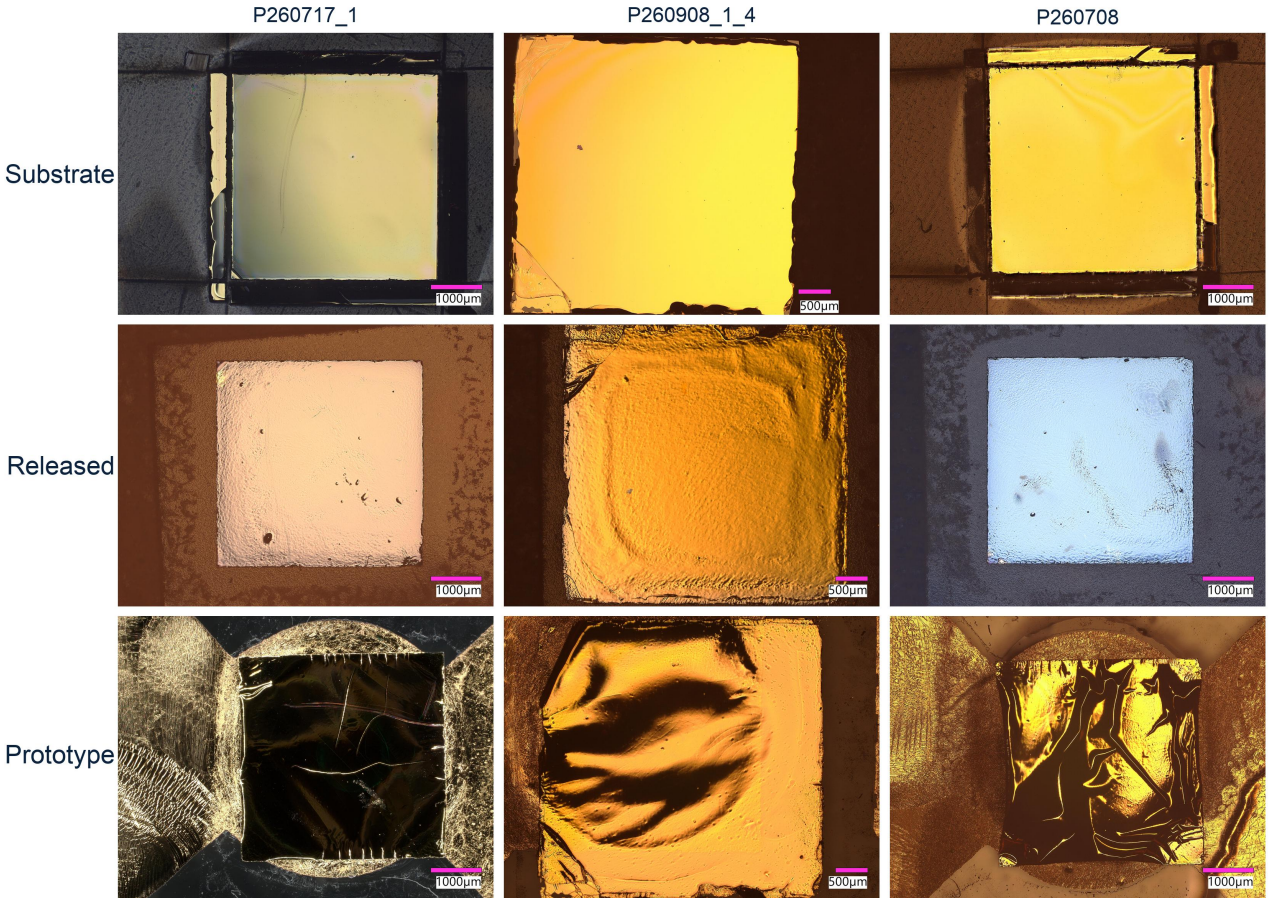


Figure 35: Films released with PMMA still on: P260717_1, P260908_1_4, and P260708. Rows are the substrate, the tape, and the prototype. P260717_1 and P260708 are 40×, so the scale bar is 1000 μm. P260908_1_4 is 50×, so its scale bar is 500 μm.

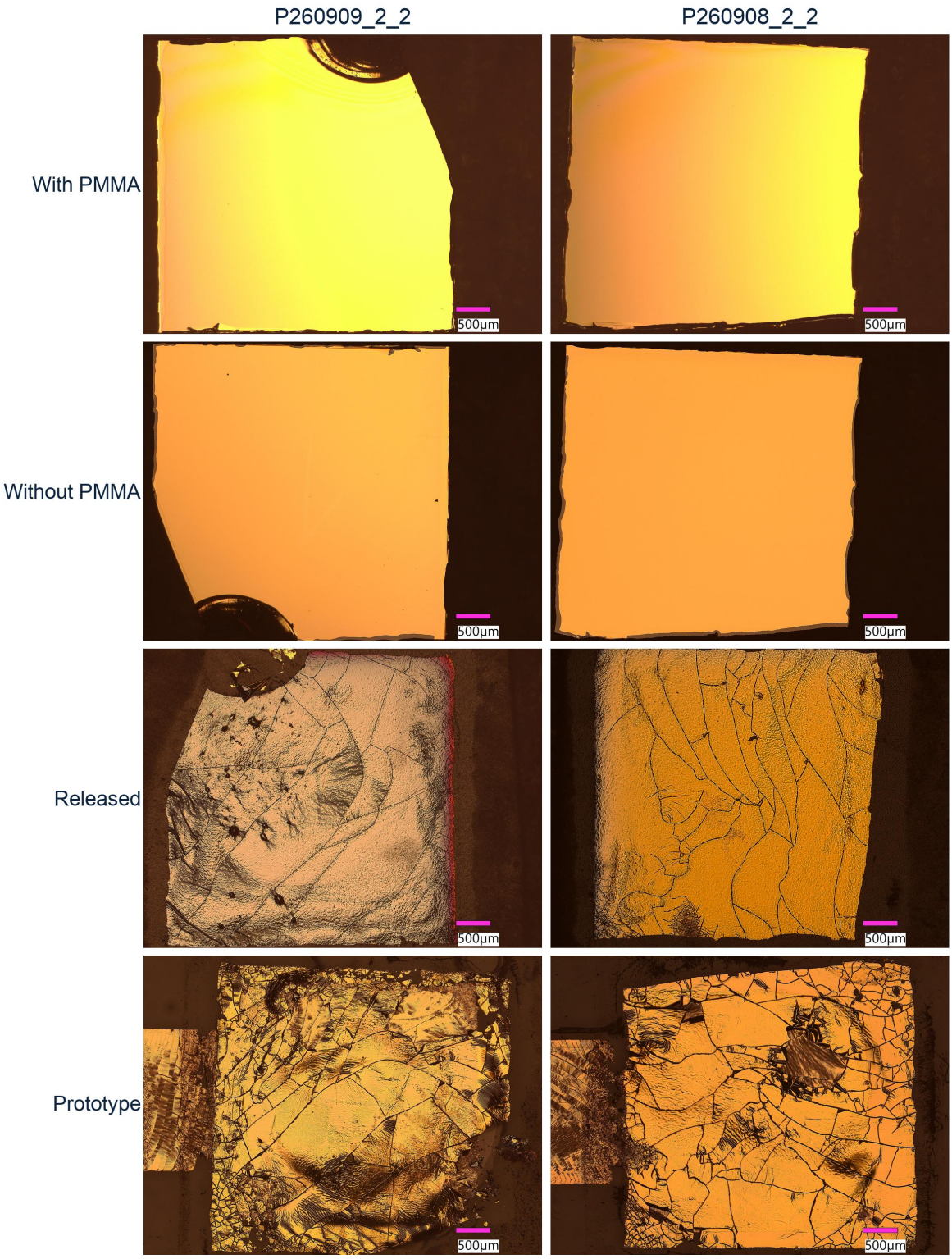


Figure 36: P260909_2_2 and P260908_2_2, the PMMA removed before release. Rows are the film on the substrate with PMMA, the same film after PMMA removal, the film on the tape, and the prototype. All frames are 50×. The scale bar is 500 μm.

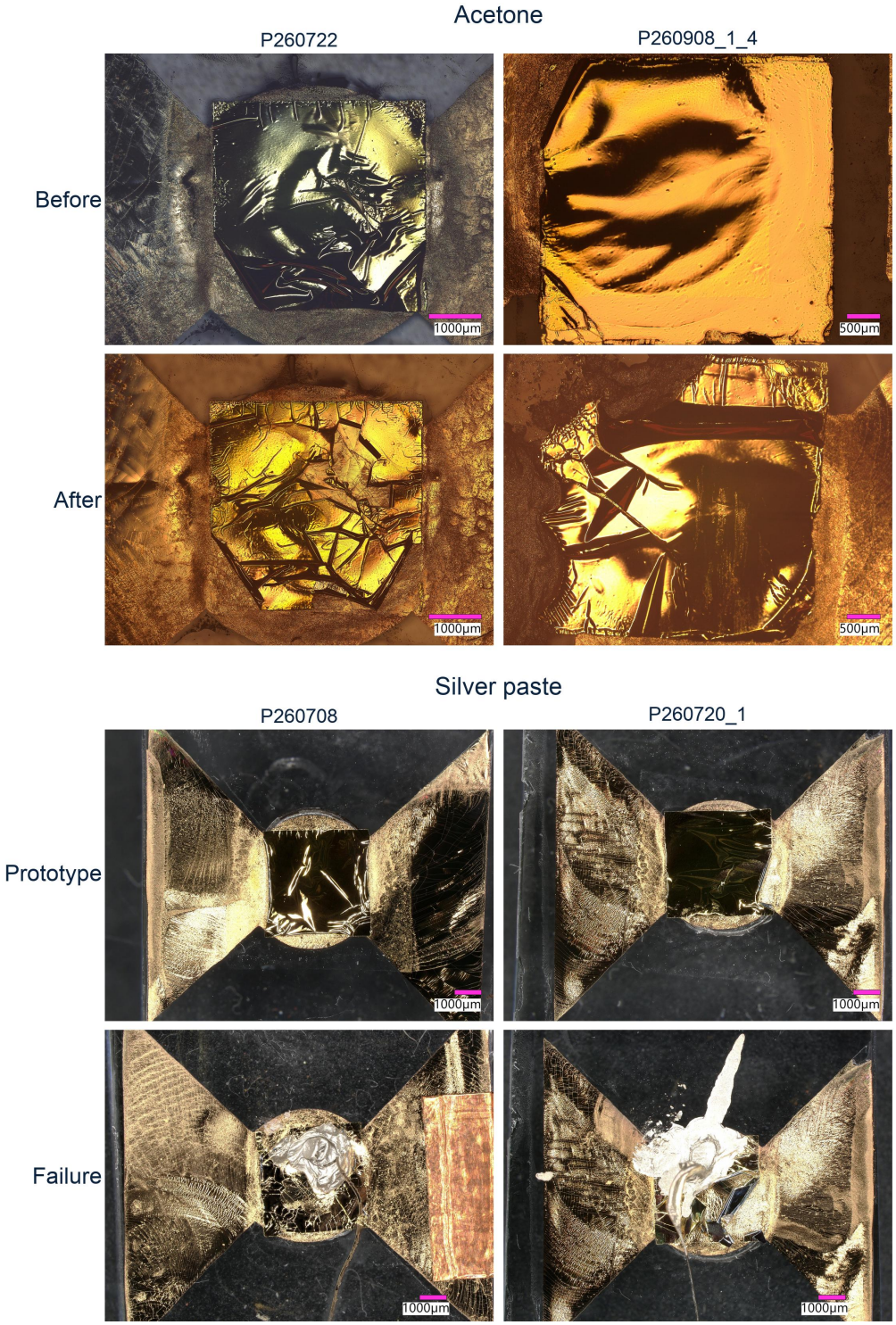


Figure 37: Failures after acetone and after silver paste. P260722 and P260908_1_4 are shown before acetone and after it. Acetone opened the film. P260708 and P260720_1 are the prototype and the same chip after silver paste shorted it. P260722 is at 40× and P260908_1_4 at 50×. The silver-paste pair is at 20×. A 40× or 20× scale bar reads 1000 μm. A 50× bar reads 500 μm.

V.1 GRADING THE TRANSFER

The prototype row in Figures 35 and 36 is the image that was graded. Figure 37 is a later frame of the same stacks. The grade of every stack is in Table 1.

A good grade is a continuous sheet across the cavity. Wrinkles, cracks at the edge of the sheet, and one corner curled where it had not bonded to the bottom electrode stay with that grade. P260717_1, P260908_1_4, and P260708 are that sheet (Figure 35). On P260908_1_4 the sheet sits slightly off the electrode. The offset was left so the contact would not short to the bottom gold. P260720_1 is the same grade. Its prototype frame is the one paired with the silver-paste frame in Figure 37.

Acceptable for testing is a sheet with film still over the cavity, so the cavity can be pressurized. A scratch, a small hole,

flakes, cracks, or a curled edge may remain, including beside the cavity. P260909_2_2 and P260908_2_2 are that case (Figure 36). On P260908_2_2 the temperature-release tape took part of the bond to the bottom electrode, and film still covers the cavity. P260722 had a small hole in the transfer image. Acetone opened it (Figure 37). P260716_1 is split by a scratch that was already on the substrate and came from handling. Acetone then left no usable film on that stack.

A bad grade is a cavity left without a usable film. P260908_1_2 has a large hole through the middle. P260721 was placed on GC260911 and shows holes, cracks, and delamination.

The grades are the transfer images. Acetone and silver paste came after them. Acetone also opened P260908_1_4. P260708 came through acetone, and silver paste then shorted it. The same setup destroyed P260720_1.

VI. ELECTRICAL MEASUREMENT

VI.1 RESISTANCE OVER CYCLING

These logs are the gold electrodes cited in Section 3.5. No oxide was on these chips. Figure 38 is the contacting: four leads on the pads outside the cavity, so the pressure cycle loads the membrane. The bottom frame is the single gold path used as the control.

Figure 40 is the results record. Figure 42 is the electrode that stays finite, and Figure 41 is the electrode that opens. At high pressure the rim deforms on GC260923_2 and stays still on GC260923_1 and GC260923_3. Figure 39**a** is the long run. Near minute 135 its resistance band shifts up by about 5 Ω. This can be due to the tape-to-pad contact changing. Panel (c) of that figure is the stepped run in Fig. 7**d**. Figure 43 is the single path.

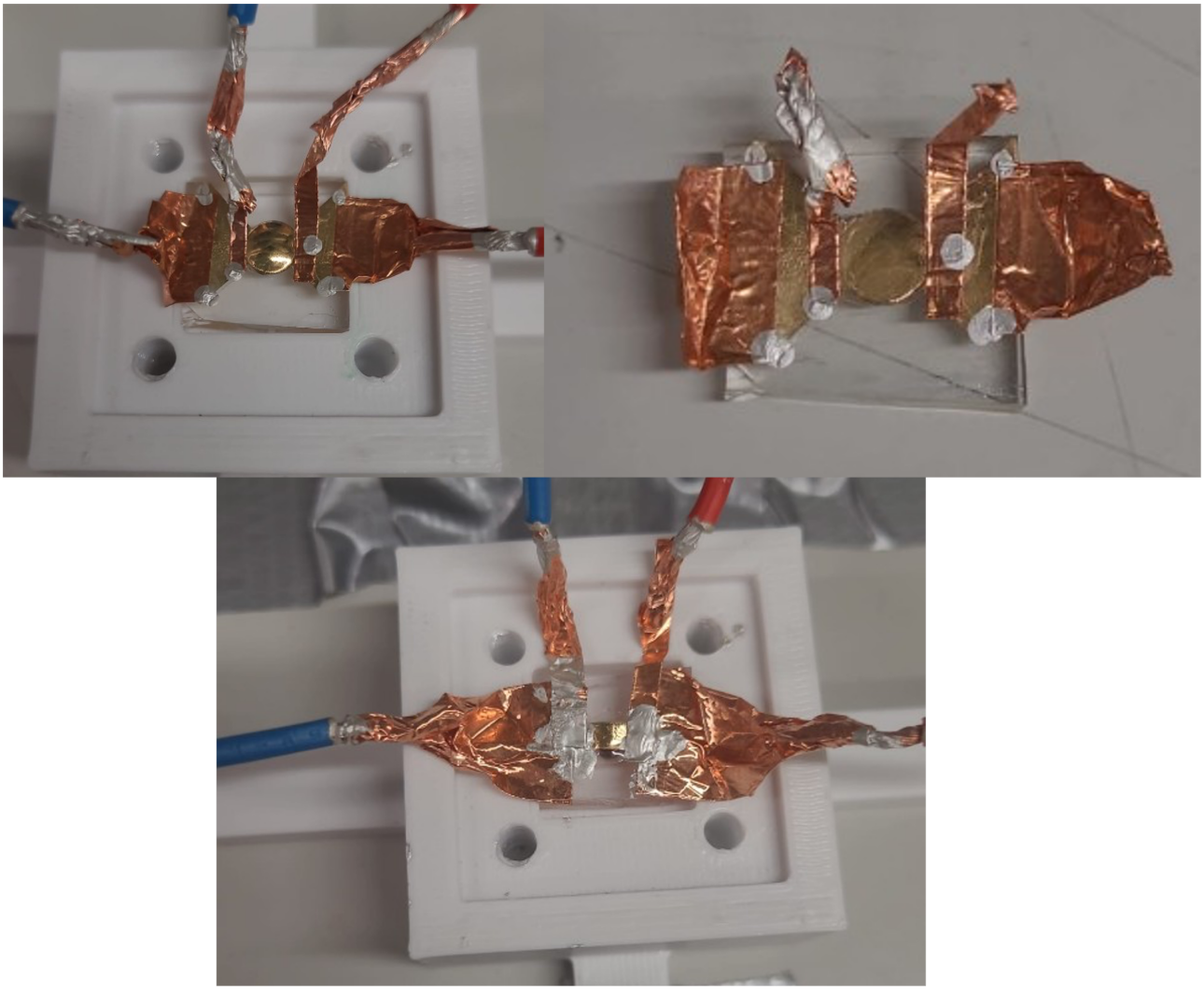


Figure 38: Contacting for the resistance logs. Top left: the chip in the holder, four leads connected with silver paste, circular gold over the entire cavity under pressure. Top right: the same chip at 0 mbar pressure. Bottom: control chip with a gold path crossing the cavity.

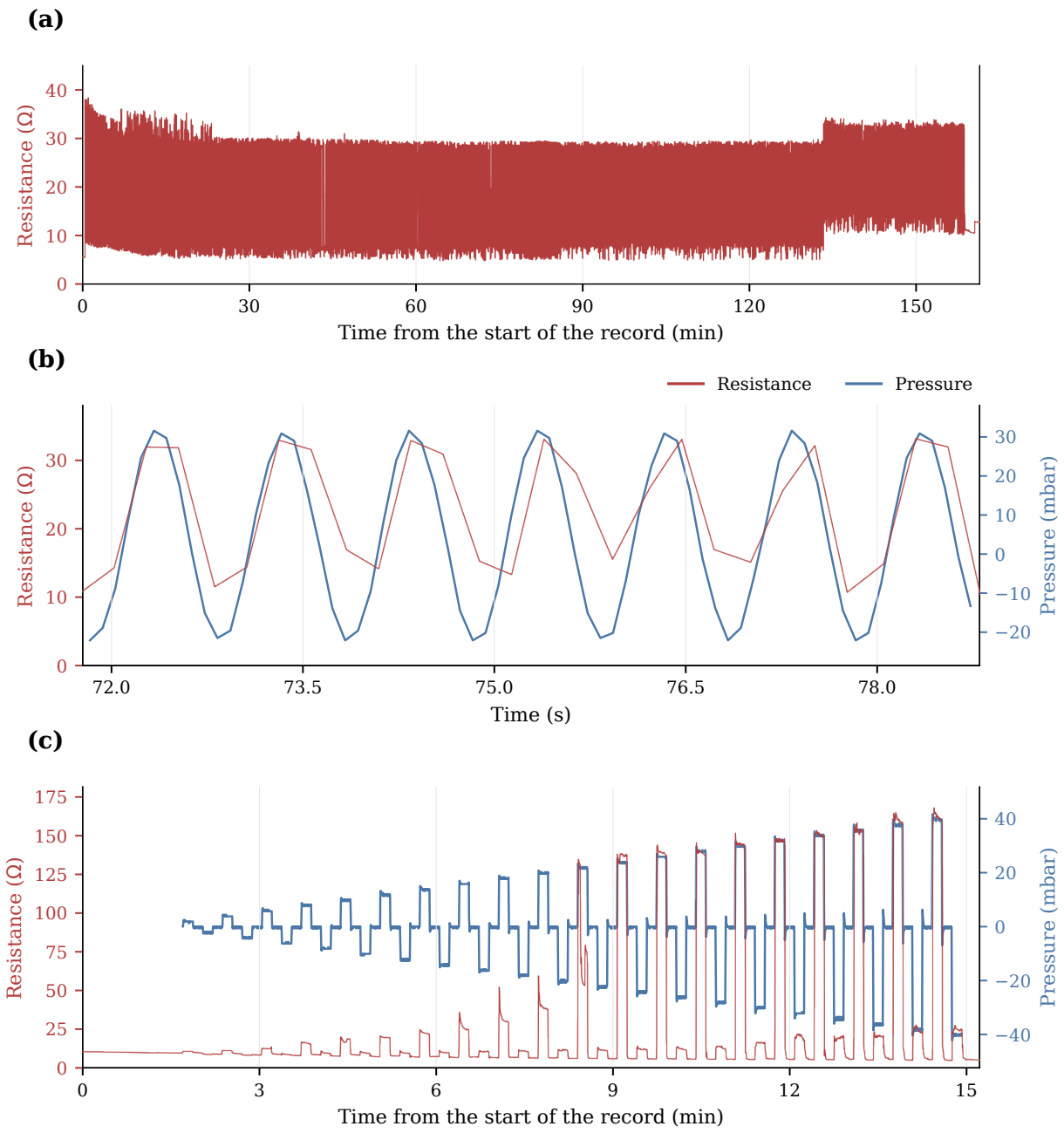


Figure 39: Four-wire resistance of GC260911_9. **(a)** 161 min measurement (ca. 9660 cycles) with pressure cycling at 1 Hz from −20 to 30 mbar. The resistance stays between about 5 and 38 Ω and ends at 12.8 Ω, from 5.7 Ω at the start. **(b)** The resistance follows the pressure. The pressure runs between about −20 and 30 mbar, and the resistance between about 11 and 34 Ω. **(c)** The resistance rises with the outward pressure steps, reaches 168 Ω, stays finite, and ends near 5 Ω. The pressure runs between about −40 and 40 mbar.

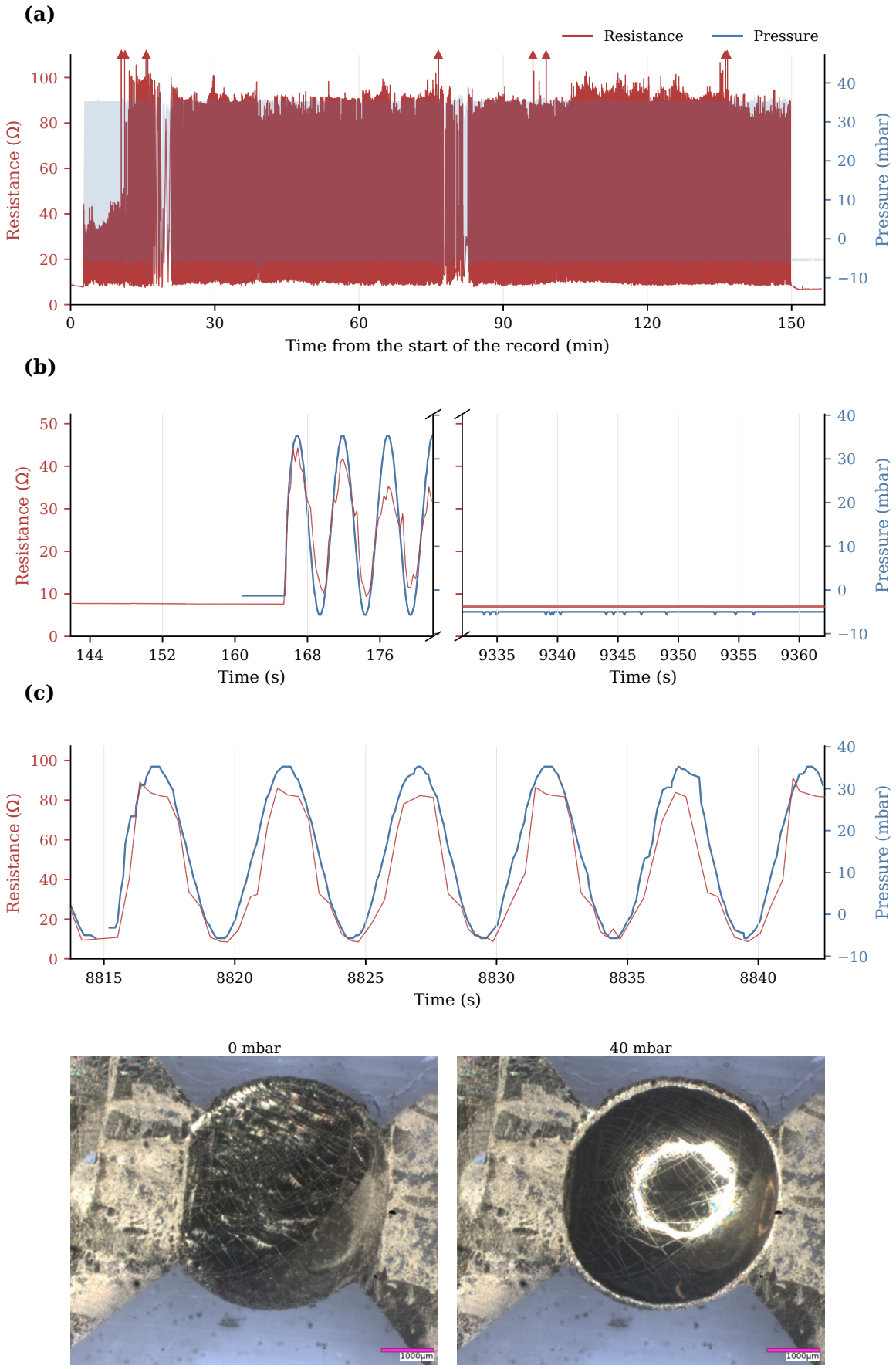


Figure 40: Four-wire resistance of GC260923_1. **(a)** The record, 156 min at 0.2 Hz (ca. 1900 cycles). Resistance and pressure are on one time axis. The pressure is the pale trace. It cycles between about −6 and 37 mbar. Triangles mark resistance readings above 110 Ω. The highest is 511 Ω. The meter does not overload. When the pressure stops, the resistance falls to about 9 Ω. **(b)** The start and the end, with the middle cut out of the time axis. On the left, the resistance is still near 9 Ω before the pressure cycle begins, and it returns to roughly that value after cycling. **(c)** A few cycles from later in the same record, in seconds. The resistance follows the pressure.

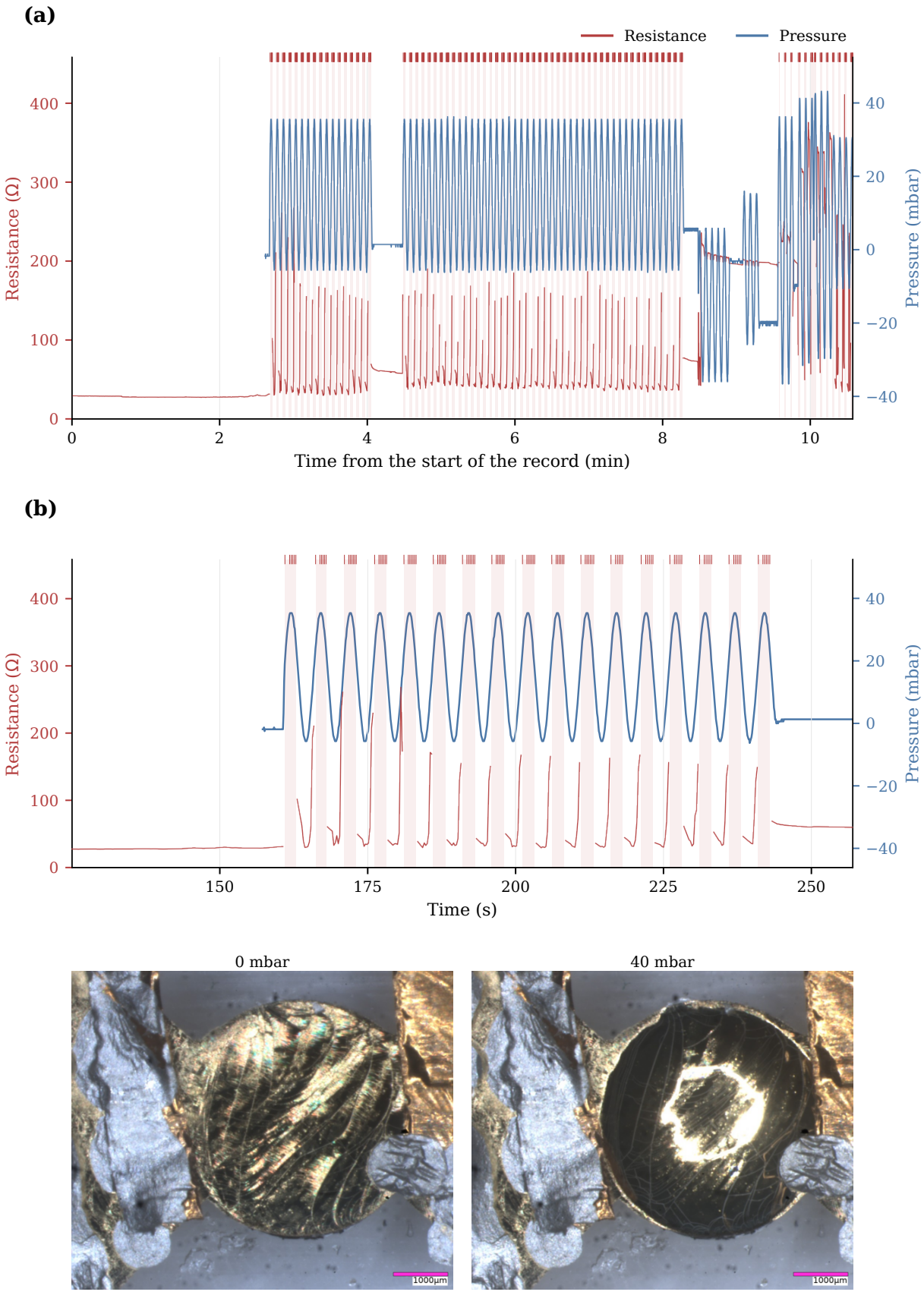


Figure 41: Four-wire resistance of GC260923_2. **(a)** About 11 min. The pressure runs from about −5 to 35 mbar. Marks at the top of the resistance axis are meter overloads. **(b)** The opening, in seconds. The meter overloads on the pressure peaks. The first overload is at about 20 mbar. The resting resistance is about 29 Ω.

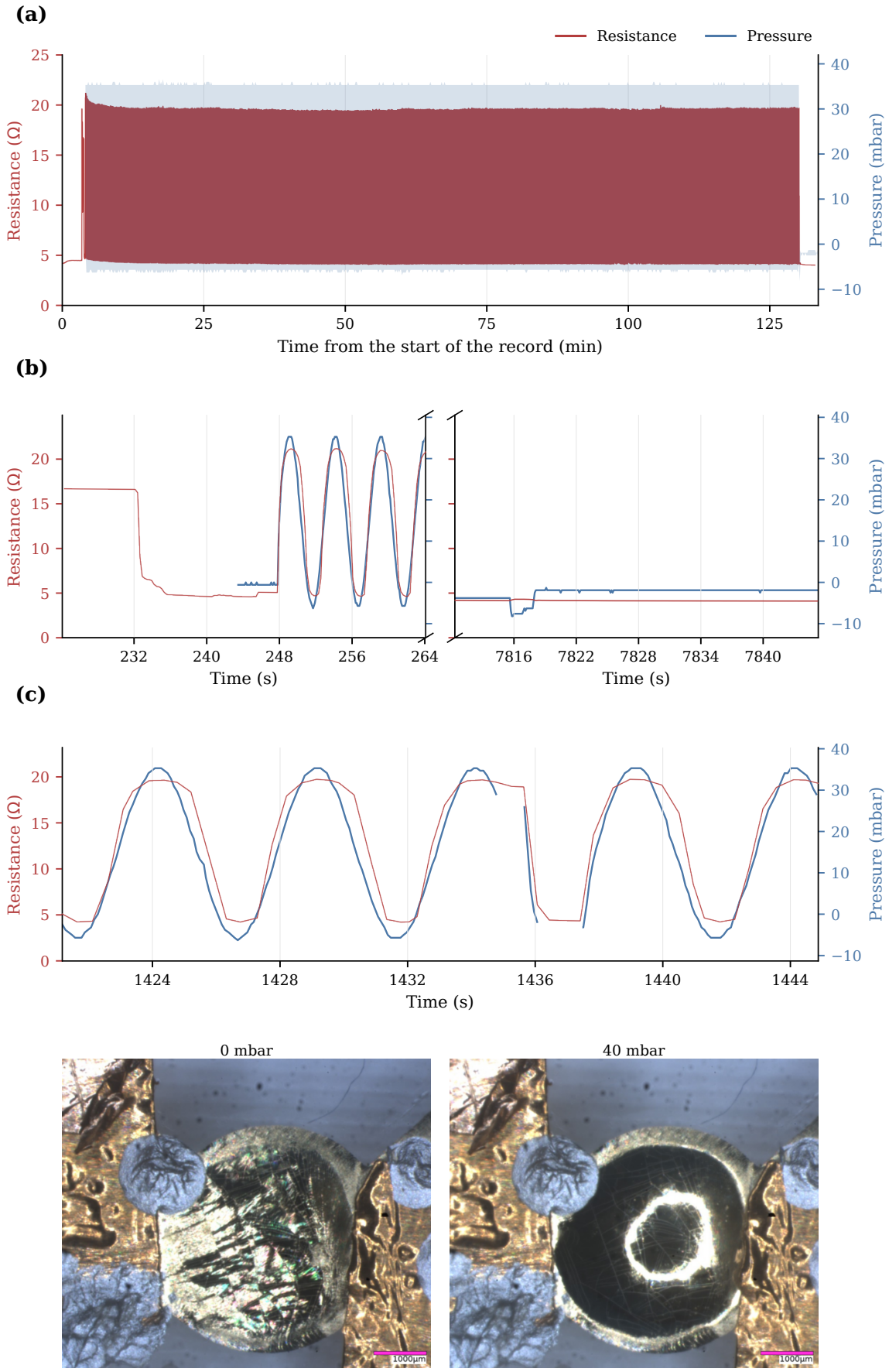


Figure 42: Four-wire resistance of GC260923_3. **(a)** The record, 133 min at 0.2 Hz (ca. 1600 cycles). The pressure is the pale trace. It cycles between about −6 and 37 mbar. The resistance stays between about 4 and 21 Ω and returns to 4.0 Ω when the pressure stops. **(b)** The start and the end, with the middle cut out of the time axis. On the left the resistance falls to about 5 Ω before the pressure cycle begins. On the right the pressure is off and the resistance sits at 4.0 Ω. **(c)** A few cycles from about 24 min into the record, in seconds. The resistance follows the pressure.

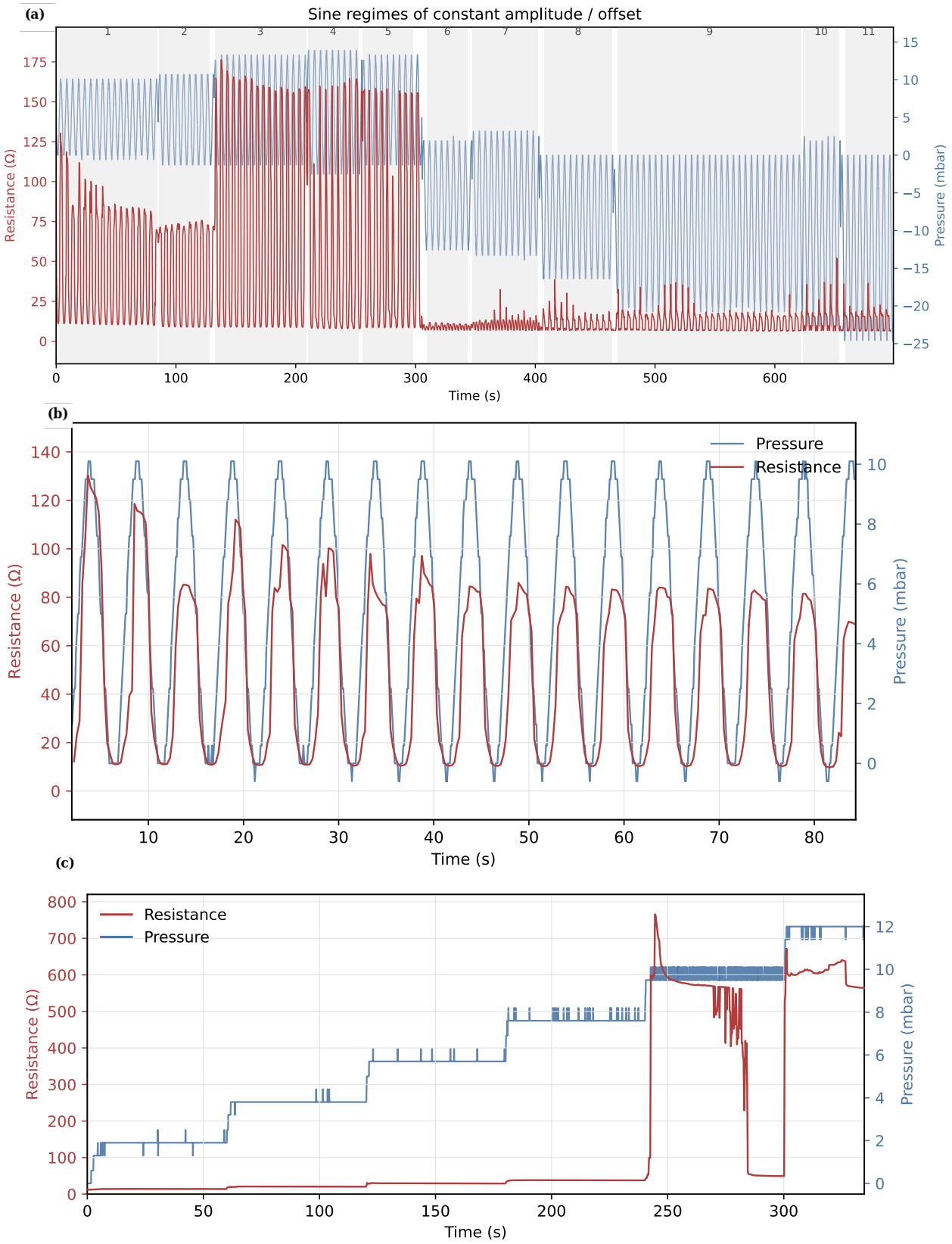


Figure 43: Four-wire resistance of the control strip. **(a)** Shows a sine varying pressure where amplitude and offset change. **(b)** The resistance follows the pressure fluctuation ranging between -2 to 10 mbar, while the resistance cycles mainly between 12 Ω to 100 Ω. **(c)** The resistance rises above 600 Ω once the threshold of 10 mbar is exceeded.

VI.2 VOLTAGE MEASUREMENTS

Open-circuit voltage was logged on the 100 mV range with a 10 MΩ input. On the runs below, the reading stays within a few millivolts while the pressure changes. It does not follow the pressure. This is not a piezoelectric output. The control trace is the noise identification on the same range and shows that nothing but noise was measured with the samples.

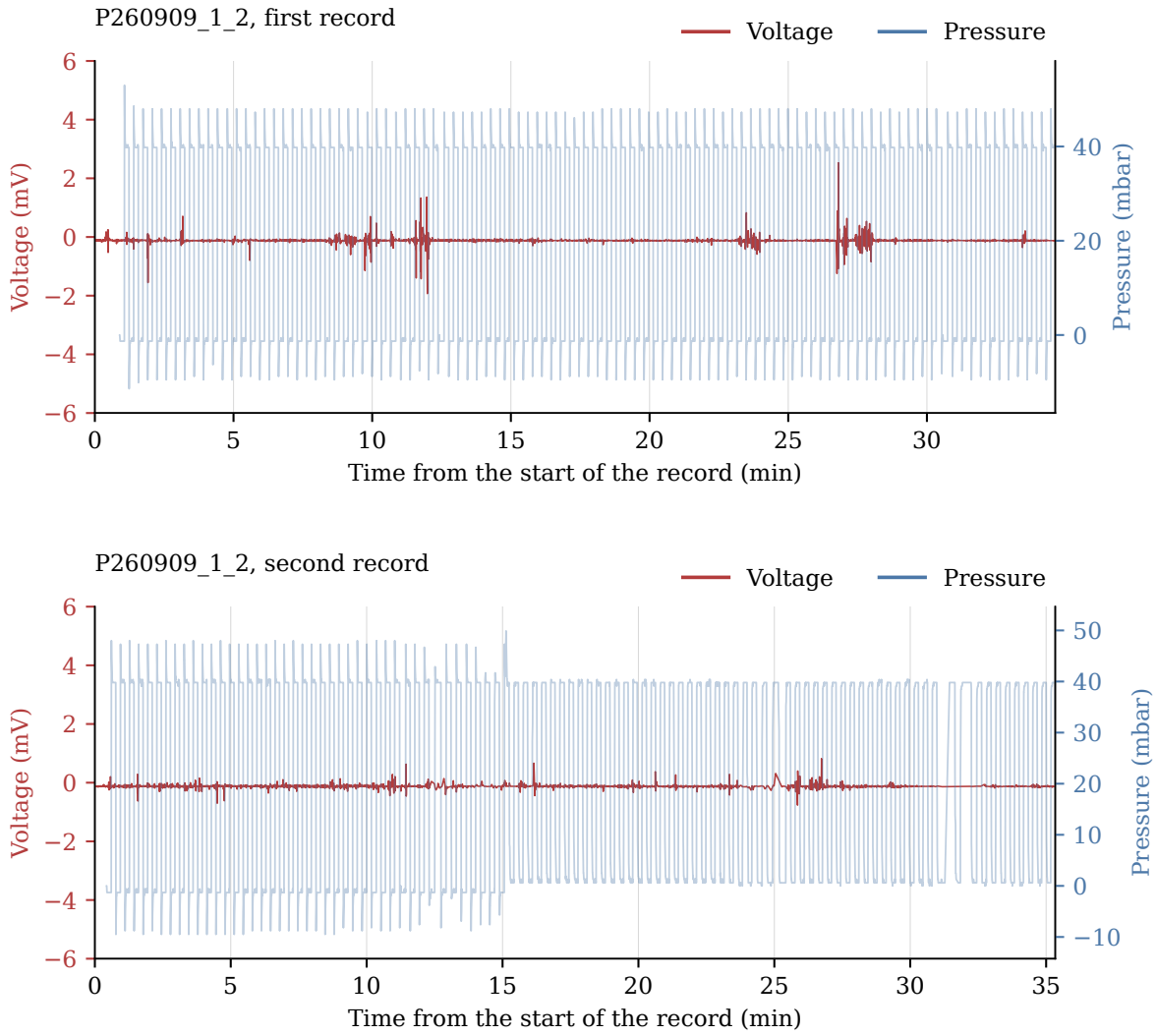


Figure 44: Open-circuit voltage of P260909_1_2, two records on 29 September 2026. The voltage stays near zero across the pressure cycles.

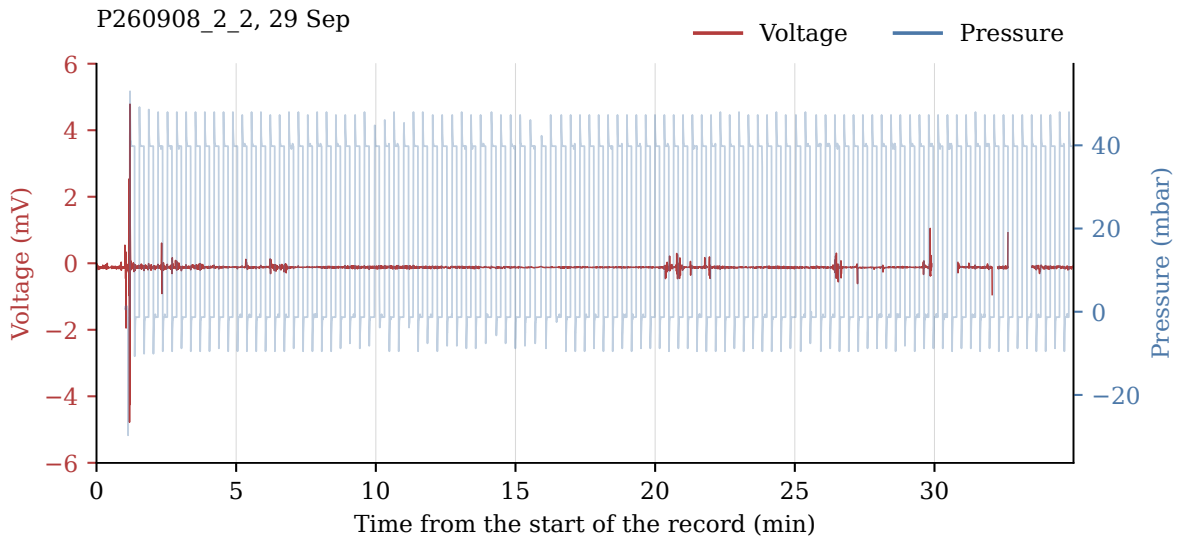


Figure 45: Open-circuit voltage of P260908_2_2 on 29 September 2026. Apart from a brief spike at the start, the voltage stays within about 1 mV while the pressure is cycled.

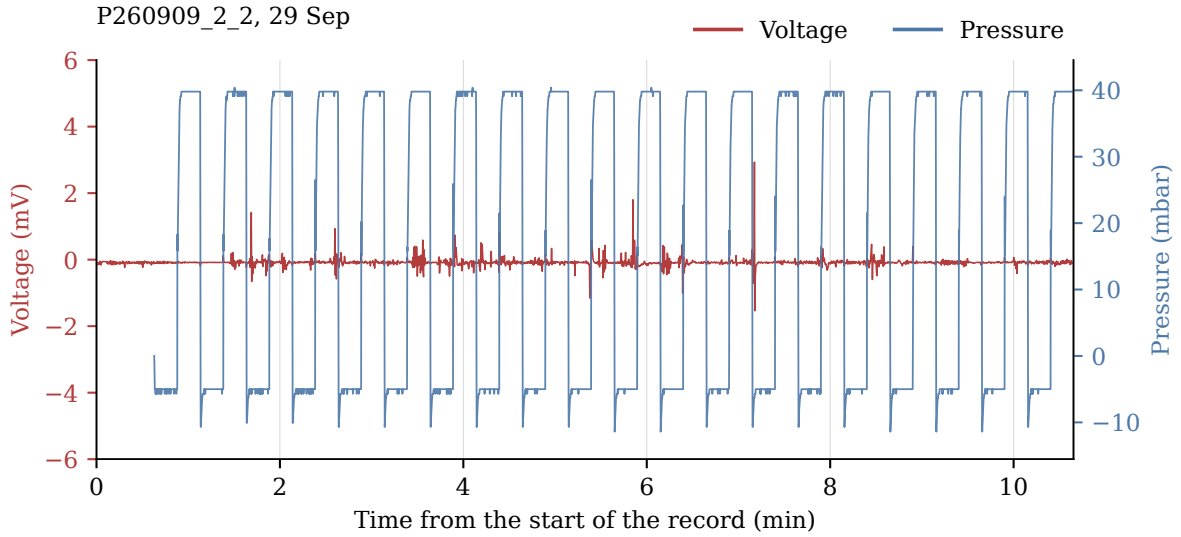


Figure 46: Open-circuit voltage of P260909_2_2 on 29 September 2026. The pressure steps between about −10 and 40 mbar. The voltage stays within a few millivolts.

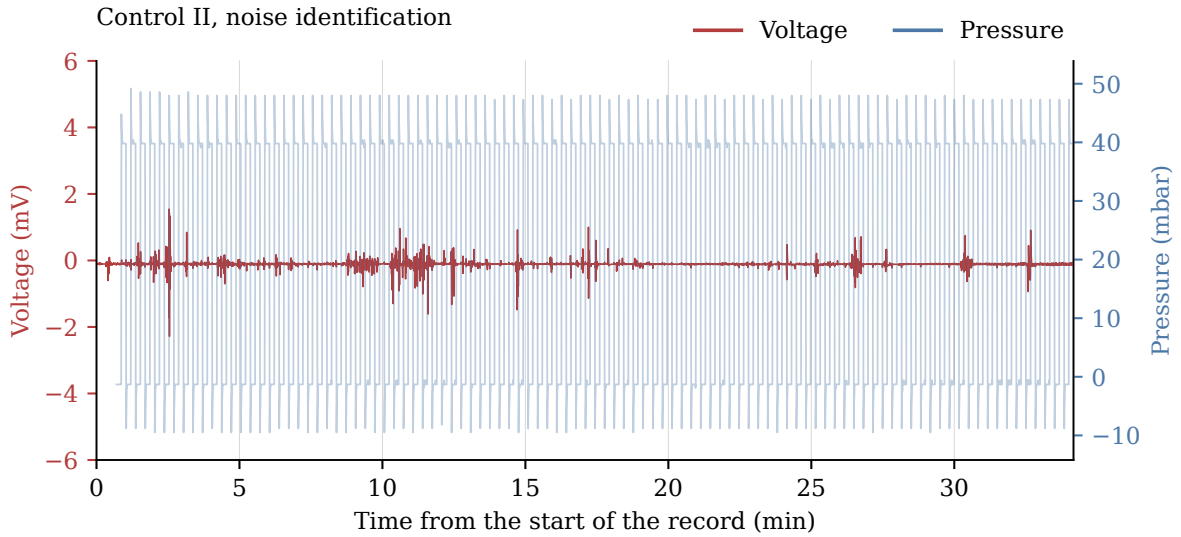


Figure 47: Open-circuit voltage during the Control II noise identification, on the same 100 mV range. The floor is a few millivolts, the same size as the chip readings above.